

**Numerical Relativity**  
**on**  
**Cosmological Past Null Cones**

A thesis submitted in fulfilment of the requirements  
for the degree of

**DOCTOR OF PHILOSOPHY (SCIENCE)**

Rhodes University

Department of Mathematics (Pure & Applied)

by

**Petrus Johannes van der Walt**

Supervised by: Prof. Nigel T. Bishop

December 2012

# Abstract

The observational approach to cosmology is the endeavour to reconstruct the geometry of the Universe using only data that is theoretically verifiable within the causal boundaries of a cosmological observer. Using this approach, it was shown in [36] that given ideal cosmological observations, the only essential assumption necessary to determine the geometry of the Universe is a theory of gravity. Assuming General Relativity, the full set of Einstein field equations (EFEs) can be used to reconstruct the geometry of the Universe using direct observations on the past null cone (PNC) as initial conditions. Observationally and theoretically this is a very ambitious task and therefore, current developments have been restricted to spherically symmetric dust models while only relaxing the usual assumption of homogeneity in the radial direction. These restricted models are important for the development of theoretical foundations and also useful as verification models since they avoid the circularity of verifying what has already been assumed.

The work presented in this thesis is the development of such a model where numerical relativity (NR) is used to simulate the observable universe. Similar to the work of Ellis and co-workers [36], a reference frame based on the PNC is used. The reference frame used here, however, is based on that of the characteristic formalism of NR, which was developed for calculating the propagation of gravitational waves. This provides a formalism that is well established in NR, making the use of existing algorithms possible. The Bondi-Sachs coordinates of the characteristic formalism is, however, not suitable for calculations beyond the observer apparent horizon (AH) since the diameter distance used as radial coordinate becomes multi-valued when the cosmological PNC reconverges in the history of a universe, smaller in the past. With this taken into consideration, the Bondi-Sachs characteristic formalism is implemented for cosmology and the problem approaching the AH is investigated.

Further developments address the limitations approaching the AH by introducing a metric based on the Bondi-Sachs metric where the radial coordinate is replaced with an affine parameter. The model is derived with a cosmological constant  $\Lambda$  incorporated into the EFEs where  $\Lambda$  is taken as a parameter of the theory of gravity rather than as a matter source term. Similar to the conventional characteristic formalism, this model consists of a system of differential equations for numerically evolving the EFEs as a characteristic initial value problem (CIVP). A numerical code implemented for the method has been found to be second order convergent. This code enables simulations of different models given identical data on the initial null cone and provides a method to investigate their physical consistency within the causally connected region of our current PNC. These developments closely follow existing 3D schemes developed for gravitational wave simulations, which should make it natural to extend the affine CIVP beyond spherical symmetric simulations.

The developments presented in this thesis is an extended version of two papers published earlier [97, 98].

# Acknowledgements

I enjoyed every minute of working on this project and consider myself very fortunate to have had the opportunity to do this work.

In particular, I had the privilege to work under the guidance of an exceptional supervisor. Besides suggesting a very fruitful topic and providing continual guidance, he also arranged funding and opportunities to present my work at international conferences. In addition, since I was an off campus student residing in Pretoria, many administrative burdens, which I couldn't personally attend to, was also handled by him. For all his help and guidance, I am sincerely grateful to Prof. Nigel Bishop.

I am also fortunate to have a supportive family. I would like to thank my wife, Brigitte, without her kind understanding, encouragement and friendship; this work would have been a distant prospect. I am also grateful to my parents who always encouraged me to learn and spared no effort to enable me to go to university, many years ago. My daughter, Bridea, was born a month after I started this project and working on this 'book' is the side of me she knows very well. She is now an inquisitive four year old and I dedicate this thesis to her.

I would also like to thank Landman Bester with whom I had some very useful discussions; I wish him all the best with the continuation of this project. Finally, I want to mention Dr Ken Craig, who introduced me to computational physics (in the form of CFD), some years ago, and spent time then to help me to understand numerical coding. It was an invaluable skill for this project.

Financial support for this project was provided by the National Research Foundation of South Africa.

# Contents

<b>1</b>	<b>Introduction</b>	<b>1</b>
1.1	Cosmology and the PNC . . . . .	2
1.1.1	The observable universe . . . . .	2
1.1.2	Parameterized versus observational models . . . . .	3
1.1.3	Observational cosmological models . . . . .	5
1.1.4	Characteristic numerical relativity . . . . .	6
1.2	Chapter outline . . . . .	6
1.3	Conventions and units . . . . .	7
<b>2</b>	<b>Cosmology and the PNC</b>	<b>9</b>
2.1	Modelling the Universe . . . . .	9
2.1.1	Relativistic cosmology . . . . .	9
2.1.2	Model dependence in cosmology . . . . .	13
2.2	Parameterized models . . . . .	15
2.2.1	Standard model - $\Lambda$ CDM . . . . .	15
2.2.2	Lemaître-Tolman-Bondi model . . . . .	19
2.2.3	The cosmological PNC . . . . .	24
2.3	Observational models . . . . .	26
2.3.1	Observable quantities . . . . .	27
2.3.2	The LTB observer approach . . . . .	33
2.3.3	The observer coordinate approach . . . . .	36
2.4	Conclusion . . . . .	42
<b>3</b>	<b>Characteristic formalism</b>	<b>44</b>
3.1	Bondi-Sachs CIVP . . . . .	44
3.1.1	Mathematical model . . . . .	44
3.1.2	Cosmological considerations . . . . .	46
3.1.3	Reconstructing the metric . . . . .	47
3.1.4	Coordinate transformations . . . . .	48
3.2	Affine CIVP . . . . .	52
3.2.1	Mathematical model . . . . .	52
3.2.2	Cosmological considerations . . . . .	54
3.2.3	Reconstructing the metric . . . . .	54
3.2.4	Coordinate transformations . . . . .	57
3.3	Conclusion . . . . .	59

<b>4</b>	<b>Numerical code</b>	<b>60</b>
4.1	Bondi-Sachs CIVP . . . . .	60
4.1.1	Mathematical algorithm . . . . .	60
4.1.2	The grid and domain of calculation . . . . .	61
4.1.3	Numerical scheme . . . . .	63
4.1.4	Boundary regions . . . . .	65
4.2	Affine CIVP code . . . . .	68
4.2.1	Mathematical algorithm . . . . .	68
4.2.2	Domain of calculation . . . . .	69
4.2.3	Numerical scheme . . . . .	69
4.2.4	Boundary regions . . . . .	71
4.3	Conclusion . . . . .	71
<b>5</b>	<b>Numerical calculations</b>	<b>73</b>
5.1	Verification framework . . . . .	73
5.1.1	Verification models . . . . .	74
5.1.2	General comments on models . . . . .	75
5.1.3	Methodology . . . . .	77
5.2	Model comparison . . . . .	78
5.2.1	Einstein-de Sitter: Bondi-Sachs CIVP . . . . .	79
5.2.2	Einstein-de Sitter: Affine CIVP . . . . .	80
5.2.3	LTB model: Bondi-Sachs CIVP . . . . .	81
5.2.4	LTB model: Affine CIVP . . . . .	81
5.2.5	$\Lambda$ CDM with $\Omega_\Lambda = 0.7$ . . . . .	82
5.3	Convergence . . . . .	83
5.3.1	Bondi-Sachs CIVP . . . . .	84
5.3.2	Affine CIVP . . . . .	85
5.4	Sensitivity to errors . . . . .	86
5.4.1	Combined input errors . . . . .	86
5.4.2	Individual input errors . . . . .	89
5.5	Code verification: Discussion . . . . .	94
5.5.1	Model comparison . . . . .	94
5.5.2	Convergence . . . . .	95
5.5.3	Sensitivity to errors . . . . .	95
5.6	Numerical experiments . . . . .	95
5.6.1	$\Lambda$ CDM versus LTB — evolution . . . . .	96
5.6.2	LTB versus $\Lambda$ CDM — matching . . . . .	96
5.7	Conclusion . . . . .	100
<b>6</b>	<b>Conclusion</b>	<b>101</b>
6.1	Summary . . . . .	101
6.2	Future developments . . . . .	103
<b>A</b>	<b>Summary of symbols</b>	<b>104</b>
A.1	Symbols in cosmology – Chapter 2 . . . . .	104

A.1.1	Coordinates . . . . .	104
A.1.2	Observable quantities . . . . .	104
A.1.3	Physical quantities . . . . .	105
A.2	Symbols in NR – Chapters 3 and 4 . . . . .	105
A.3	Relativistic symbols . . . . .	106
A.4	Abbreviations . . . . .	106
<b>B</b>	<b>Maple code</b>	<b>107</b>
B.1	Affine CIVP . . . . .	107
<b>C</b>	<b>Fortran code</b>	<b>110</b>
C.1	Code layout . . . . .	111
C.1.1	Flowchart . . . . .	111
C.1.2	Call graph . . . . .	112
C.1.3	Program routines . . . . .	113
C.2	Code . . . . .	115
<b>D</b>	<b>Scilab code</b>	<b>147</b>
D.1	Einstein-de Sitter transformation . . . . .	147
D.2	LTB transformation . . . . .	151
D.3	$\Lambda$ CDM transformation . . . . .	155

# List of Tables

5.1	Summary of verification models for evaluating accuracy and stability. . . . .	76
5.2	Affine CIVP test cases. . . . .	78
5.3	Summary of convergence results. . . . .	95
5.4	$\Lambda$ CDM models used to match the LTB density profile. . . . .	97
C.1	Affine CIVP code modules. . . . .	113
C.2	Affine CIVP code modules. . . . .	114

# List of Figures

1.1	The observable universe is defined as the PNC of an observer at the cone vertex. As a result of expansion, the earlier Universe was smaller causing the PNC to contract and refocus. The LSS is the visual boundary for observed EMR (based on Figure 2 in [33]). . . . .	2
2.1	In comparison to Figure 1.1 on page 2, in an inhomogeneous isotropic universe surfaces of constant time is irregular (based on Figure 3 in [33]). . . . .	23
2.2	The diameter distance ( $d_D$ ) against redshift ( $z$ ) of the Einstein-de Sitter model .	26
2.3	Past null cone of the Einstein-de Sitter model . . . . .	26
2.4	Cosmological number counts $N$ . . . . .	32
2.5	Observational coordinates (based on Figure 1 in [36]) . . . . .	37
3.1	Null cone coordinates of the CIVP . . . . .	45
3.2	The affine CIVP coordinates for cosmology. . . . .	55
3.3	The radial distance coordinates $d_D = r(z)$ and $\lambda$ related to $z$ , which is a common observational measure. . . . .	58
4.1	The past null cone calculated on a rectangular grid. . . . .	62
4.2	Stencil for numeric solution: points indicated with shaded squares are used to calculate the point indicated by the solid dot. . . . .	63
4.3	The past null cone calculated on a rectangular grid with an affine parameter ( $\lambda$ ) as the radial coordinate. . . . .	69
5.1	The past null cone of the bang time models compared to the Einstein-de Sitter model and the $\Lambda$ CDM model. . . . .	76
5.2	Density distribution (A) and covariant velocity (B) on PNCs at different proper times ( $u$ ) evolved from a local PNC up to $z = 0.47$ . . . . .	79
5.3	Density distribution (A) and covariant velocity (B) on PNCs at different proper times ( $u$ ) evolved from a local PNC up to $z = 4.5$ . . . . .	80
5.4	Diameter distance against $\lambda$ (A) and against of $z$ (B) on PNCs at different proper times ( $u$ ) evolved from a local PNC up to $z = 4.5$ . . . . .	80
5.5	Density distribution (A) and covariant velocity (B) on PNCs at different proper times ( $u$ ) evolved from a local PNC up to $z = 0.47$ . . . . .	81
5.6	Density distribution (A) and covariant velocity (B) on PNCs at different proper times ( $u$ ) evolved from a local PNC up to $z = 1.2$ . . . . .	81
5.7	Diameter distance against $\lambda$ (A) and against of $z$ (B) on PNCs at different proper times ( $u$ ) evolved from a local PNC up to $z = 1.2$ . . . . .	82

5.8	Density distribution (A) and covariant velocity (B) on PNCs at different proper times ( $u$ ) evolved from a local PNC up to $z = 5$ . . . . .	82
5.9	Diameter distance against $\lambda$ (A) and against of $z$ (B) on PNCs at different proper times ( $u$ ) evolved from a local PNC up to $z = 5$ . . . . .	83
5.10	Radial error distribution on the youngest null cones for the Einstein-de Sitter ( $u_{max} = 0.24$ )(A) and LTB ( $u_{max} = 0.15$ )(B) models for different grid resolutions. In (C), the error against grid size is shown; the slope of the change in error represents the order of convergence and is indicated in brackets in the legend. . . . .	84
5.11	Radial error distribution on the youngest null cones for the Einstein-de Sitter ( $u_{max} = 0.35$ )(A), $\Lambda$ CDM ( $u_{max} = 0.4$ )(B) and LTB ( $u_{max} = 0.2$ )(C) models for different grid resolutions. In (D), the error against grid size is shown; the slope of the change in error represents the order of convergence and is indicated in brackets in the legend. . . . .	85
5.12	Error propagation of relative constant input errors in $z$ , $\hat{r}$ and $\rho$ with a value of 10% shown in (A). In (B), the output error on $\rho$ , (C) the output error on $\hat{r}$ and in (D) the output error on $z$ . . . . .	86
5.13	Error propagation of relative cyclic input errors in $z$ with 1%, $\hat{r}$ with 10% and $\rho$ with 10% shown in (A). In (B), the output error on $\rho$ , (C) the output error on $\hat{r}$ and in (D) the output error on $z$ . . . . .	87
5.14	Error propagation of relative random input errors in $z$ with peaks at 2% and $\hat{r}$ and $\rho$ with peaks at 10% shown in (A). In (B), the output error on $\rho$ , (C) the output error on $\hat{r}$ and in (D) the output error on $z$ . . . . .	88
5.15	Error propagation of a 10% relative cyclic input error in $\hat{r}$ shown in (A). In (B), the output error on $\hat{r}$ , (C) the output error on $z$ and in (D) the output error on $\rho$ . . . . .	89
5.16	Error propagation of a 10% relative cyclic input error in $\rho$ shown in (A). In (B), the output error on $\rho$ , (C) the output error on $r$ and in (D) the output error on $z$ . . . . .	90
5.17	Error propagation of a 1% relative cyclic input error in $z$ shown in (A). In (B), the output error on $z$ , (C) the output error on $\hat{r}$ and in (D) the output error on $\rho$ . . . . .	91
5.18	Error propagation of a 3% relative cyclic input error in $z$ shown in (A). In (B), the output error on $z$ , (C) the output error on $\hat{r}$ and in (D) the output error on $\rho$ . . . . .	92
5.19	Error propagation of a relative random input error in $z$ that peaks around 10% shown in (A). In (B), the output error on $z$ , (C) the output error on $\hat{r}$ and in (D) the output error on $\rho$ . . . . .	93
5.20	Density distribution (A) and covariant velocity (B) on past null cones at different proper times ( $u$ ) . . . . .	97
5.21	Density distribution and covariant velocity on the past null cones: LTB with $\Omega_\Lambda = 0$ and FLRW with $\Omega_\Lambda = 0.7$ at $t_0 - 6$ Gyrs and the best fit FLRW $\Omega_\Lambda = 0$ instance. . . . .	98
5.22	Density distribution and covariant velocity on the past null cones: LTB with $\Omega_\Lambda = 0$ and FLRW with $\Omega_\Lambda = 0.7$ at $t_0 - 6$ Gyrs and the best fit FLRW $\Omega_\Lambda = 0.5$ instance. . . . .	98
5.23	Density distribution and covariant velocity on the past null cones: LTB with $\Omega_\Lambda = 0$ and FLRW with $\Omega_\Lambda = 0.7$ at $t_0 - 6$ Gyrs and the best fit FLRW $\Omega_\Lambda = 0.7$ instance. . . . .	98
5.24	Density distribution and covariant velocity on the past null cones: LTB with $\Omega_\Lambda = 0$ and FLRW with $\Omega_\Lambda = 0.7$ at $t_0 - 6$ Gyrs and the best fit FLRW $\Omega_\Lambda = 0.9$ instance. The stable region for this plot is limited to a a smaller region but also shows an unlikely match for both $\rho$ and $v_1$ simultaneously. . . . .	99

C.1	Conceptual flowchart for the affine CIVP Fortran code. . . . .	111
C.2	Call graph for the affine CIVP Fortran code. . . . .	112

# Chapter 1

## Introduction

Provided that General Relativity is valid up to the largest scales, under ideal circumstances, the spacetime structure of the Universe can be determined by solving the full set of Einstein field equations (EFEs) using observational data as the boundary conditions. Such an observational approach makes use of minimal assumption and observations as the boundary conditions dictate the outcome of the solution. Because of difficulties in obtaining and interpreting observational data, the conventional approach to cosmology is rather based on parameterized models where a model is assumed and then validated against different sets of observations and constraints. Assuming a homogeneous universe with a non-zero cosmological constant and with suitable adjustments of parameters, predictions using the  $\Lambda$ CDM model show remarkable correlation with observed cosmological parameters. The assumption of homogeneity, which is an integral part of this approach, has the convenient property that conclusions derived from local observations will also be valid for the rest of the Universe.

Developments under the assumption of homogeneity have been remarkably successful in reproducing observed cosmological parameters. However, doing investigations such as quantifying homogeneity on different scales, testing the verifiability of cosmology [36], validating the Copernican principle [96] and determining the metric of the Universe [50], a more suitable methodology is one where the EFEs are solved using a general metric and boundary conditions derived from observations. Without the assumption of homogeneity, conclusions following from the observational approach are necessarily limited to the causally connected region in the interior of our current past null cone (PNC) on which observations are located. Since the EFEs are solved in a general form, or at least more general than the  $\Lambda$ CDM model, there are more degrees of freedom and also more required boundary conditions. Sufficiently accurate and complete observations do not currently exist for full general solutions, however, in spherical symmetry with some assumptions, the concept of solutions from direct observations can be applied using currently available data and can provide a useful ground for verification of proposed cosmological models. The work presented in this thesis is the development of such a model specifically designed for numerical modelling.

# 1.1 Cosmology and the PNC

## 1.1.1 The observable universe

Assuming that relativistic physics is governed by universal laws, the causality of information is the fundamental limit of verification in cosmology. Since electromagnetic radiation (EMR), which carries all information currently accessible to us, travels at the speed of light, we only have access to observations that had time to reach us during the age of the Universe. Causality limits our observations to three regions. Firstly, the boundary of observations is defined by null geodesics connected to the observer. These geodesics trace out a PNC connected with an observer at its vertex. Objects on the surface of the PNC are directly observable through some form of radiation. Secondly, objects with mass, such as meteorites, will be within the PNC and aspects such as their composition and age can provide historical information and indirectly place constraints on cosmological parameters. Thirdly, indirect information from objects that passed the PNC surface at some time in the past can be inferred by their influence on directly observable objects. A detailed discussion relating the observable regions with observations is presented in [36].

The PNC is, however, not fully accessible and there are physical and practical limitations further restricting the directly observable part of the Universe. Since looking down the PNC implies looking back in time, theoretically, an observer should be able to look back to the beginning of time. However, events in the earlier Universe physically limit observers to probe back to the origin. The most prominent restriction is in the early hot Universe where radiation was coupled to matter. Before the Universe cooled down enough for matter and radiation to decouple the Universe was opaque. This creates a visual boundary around the early Universe, known as the last scattering surface (LSS) and is detectable as the cosmic microwave background (CMB). Probes such as the COBE, WMAP and Planck satellites captured detailed images of the LSS. Figure 1.1 illustrates the PNC in a homogeneous universe; this will be discussed in more detail in Section 2.2.3.

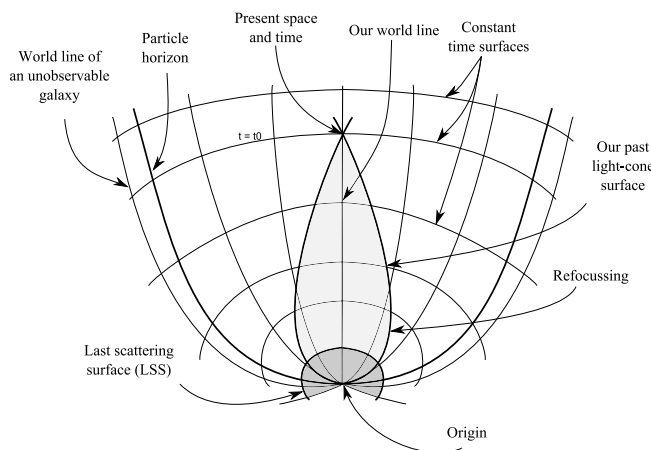


Figure 1.1: The observable universe is defined as the PNC of an observer at the cone vertex. As a result of expansion, the earlier Universe was smaller causing the PNC to contract and refocus. The LSS is the visual boundary for observed EMR (based on Figure 2 in [33]).

These restrictions limit the observable universe to a finite sub-region of the Universe. From an observational point of view there are many other practical challenges, such as the Malmquist bias, K-corrections and intergalactic absorption amongst others [72]. In addition, at the vertex of the cone, we view the Universe at one location and effectively only one point in time. In contrast to laboratory experiments, we cannot manipulate the object of investigation or repeat the experiment. Furthermore, our most consistent theory of large scale gravity, General Relativity, is governed by a theoretical complicated set of equations, the Einstein field equations (EFEs), which regardless of its physical representation, can be extremely difficult to analyse. For these reasons, it is common in cosmology to construct models where degrees of freedom are restricted by assumptions and then attempt to fit remaining free parameters to the observations they represent. Currently this is limited to models where the Universe is assumed to be homogeneous and the limits of causality do not restrict the region of investigation since the observations at one location represent all other locations at the same epoch.

### 1.1.2 Parameterized versus observational models

The conventional approach to cosmology is based on *parameterized models*, which are used to search for the simplest model that reproduces observable phenomena. Priority is given to simplicity and it is thereby assumed that local physics is universal and the Universe is homogeneous. The Friedman-Lemaître-Roberson-Walker (FLRW) class of models is the mathematical representation under these assumptions. Surprisingly, with very little knowledge of the restriction and complications already discussed, these models, which were derived in the 1920s and 1930s, are consistent with data from the most recent advances in observational technology. It seems remarkable that assumptions, initially made to simplify theory, hold enough physical significance to capture the most important properties of the Universe. Conveniently, these models can easily be written in terms of a few free parameters and the objective is to find the best fitting parameter values from observations. Currently, the  $\Lambda$ CDM model, the FLRW model with a non-zero cosmological constant, is the simplest model for which the required parameters can be substantiated by observations. Only three parameters are required to describe this model: the Hubble constant, the deceleration parameter and the cosmological constant.

In the future, if it turns out that the  $\Lambda$ CDM model is not adequate to represent some new observations, it will be necessary to adapt to a more suitable model; this might require that a more complicated class of models has to be investigated. For instance, instead of assuming a FLRW geometry, the spherically symmetric radial inhomogeneous Lemaître-Tolman-Bondi (LTB) geometry can be assumed. However, when assuming a specific model, there can always be a more general model that can provide an interpretation of observations which seems plausible, especially if the interpretation of observations is related to the assumption of the specific model. Instead of trying to match observations using parameterized models an alternative approach is to derive the properties of the Universe directly from observations. This approach uses *observational models* and follows a strategy of fixing boundary conditions to values obtained from observations and let these determine the degrees of freedom of a more general model, restricted by fewer assumptions. This approach is referred to as the *direct observational approach* since it attempts to use only data causally connected to the observer without narrow assumptions of specific cosmologies. As an example, the LTB model contains homogenous models as subclasses and with certain boundary conditions degenerate to the FLRW models. Therefore, if boundary

conditions restrict an assumed LTB geometry to the simpler case of a FLRW geometry, it can be said with more certainty that the the assumption of a FLRW geometry is correct. However, if this is not the case, it might be that certain effects are the result of radial inhomogeneity; a result that would have been difficult to predict from the assumption of a FLRW geometry.

The process of restricting a general model with boundary conditions is common in Newtonian astrophysics and other classical field theories, especially in numerical modelling. It might therefore appear curious that cosmology rather follows an approach of model assumption with parameter verification. In particular, there is no guarantee that the assumed model is the only model that reproduces observations within acceptable limits. In fact, the  $\Lambda$ CDM model is only the simplest model of a larger class which reproduce current observations. In addition, its simplicity is contained in the assumed geometry while it introduces unknown phenomena to justify the properties of resulting parameter values. While this is a disadvantage it is also a benefit, since we do not understand observations well enough to derive unambiguous boundary conditions, which might contain completely unknown phenomena. The parameterized approach has the freedom to introduce aspects such as dark energy to explain unexpected observations. Using fluid approximation for the Universe and assuming isotropy, for instance, we require initial data of velocity and density profiles for the LTB model. These are not what we observe. Our source of information is EMR and from radiative flux, spectral shifts, number counts and the properties of objects inaccessible by other means we have to derive the fluid properties. That is assuming the observable objects are representative of all contributions to the cosmic fluid.

Using the model approach, the current interpretation of observations strongly suggest that the energy-density content of the Universe is significantly dictated by dark matter and dark energy which are only detectable by their gravitational interaction with observable objects. Since these are not directly observable, a pure observational approach seems to be a distant prospect. To incorporate mostly unobservable part of the Universe into the observational approach, some assumption have to be made (see [35]):

- i. The ratio of dark matter to baryonic matter can be derived from observational data such as the CMB.
- ii. The 4-velocity of dark matter is aligned with that of baryonic matter.
- iii. Knowledge of dark energy has to be assumed.

Without these, if we should try to implement the observational approach using only direct observations, alternative models where the effects of dark energy and dark matter are explained with observable matter will have to be considered. This might require an alternative theory to General Relativity.

Both the approaches of parameterized and observational models have their limitations and advantages. Parameterized models are not unique but have the freedom to introduce unexpected phenomena while observational models are dependent on only the observable content of the Universe but provide unique results. Parameterized models are predominantly used in cosmology with only a few groups advocating observational models. We make the point here that, although not in its purest form, the observational approach can provide an important tool for cosmology. In particular, it is a very useful ground for the verification of proposed models since it can avoid some of the circularity of proving what has already been assumed. This can

be done by calculating a reversed initial value problem using observations, with some interpretation, on the PNC as initial conditions. This type of model verification is demonstrated in Chapter 5 where the histories of the  $\Lambda$ CDM model is compared with that of an LTB model without a cosmological constant.

### 1.1.3 Observational cosmological models

Much of the developments on observational models were inspired by the seminal paper of Kristian & Sachs [56] published in the 1966. Their work was based on earlier investigations by McCrea and collaborators [64, 65, 43] which were developments to derive the properties of direct observations under the assumption of a FLRW geometry. The approach of Kristian & Sachs was, however, unique in that they systematically restricted a general metric to a specific geometry using observations. Moreover, an important aspect is their treatment of observations, using the properties of geometric optics without assuming a specific theory of gravity. In their derivations they made use of series expansions, so their study was necessarily restricted to a region close to the observer. The ideas introduced by Kristian & Sachs were the starting point of further developments by Ellis, Stoeger, Maartens and others in their *Observational Cosmology* programme with its initial publication in 1985 [36]. In these developments, observational coordinates, based on the concept introduced by Temple in 1938 [94], were implemented to extend the region investigated by Kristian & Sachs to higher redshifts. Observational coordinates are based on null geodesics on the PNC and are therefore the natural framework on which EMR reaches an observer. Solving the EFEs for cosmology in this framework consists of two problems: firstly, astronomical observations are used to determine the metric on the local PNC and secondly these form the final values of a reversed characteristic initial value problem (CIVP), which determines the historical evolution of the region causally connected to the PNC (i.e. the interior of the PNC). The causally connected region is of fundamental importance since it defines the limits on which cosmological models can be validated from direct observations.

In developments towards exact solutions in observational cosmology, spherically symmetric solutions are taken as a first step to refine the methods (see for instance [91, 89, 92, 93, 3, 4, 5, 6, 7]). Spherical symmetry by itself is not necessarily unrealistic since the Universe does appear to be highly isotropic. The spherically symmetric inhomogeneous LTB model in observational coordinates is therefore an important tool for verifying these developments. The LTB model in its standard form also provides a useful framework to investigate solutions from direct observations. In this approach, observations on the PNC are transformed to cosmological coordinates and then related to the coefficients of the LTB metric (e.g. see [71]). These transformations require numerical solutions to handle observational data and recent work by Lu & Hellaby [51] and McClure & Hellaby [63] developed and refined methods for setting up the local PNC from data based on realistic observations with the intention to be implemented on data obtainable in the next generation of astronomical surveys. It should be noted that the emphasis in observational models lies in the fact that the initial (final) conditions are provided by direct observations on the PNC and that the EFEs are implemented in a general form with minimal assumptions.

### 1.1.4 Characteristic numerical relativity

In numerical relativity (NR), methods to implement general solutions of the EFEs have been well established for strong gravitational scenarios where gravitational waves (GWs) are expected to be formed. Similar to EMR, gravitational radiation also propagates along null geodesics and null cones also provide a natural frame of reference. In this case, however, it is the future null cone that is of interest in the form of a future directed CIVP. The characteristic formalism in NR is based on the theoretical developments of Bondi, van der Burg & Metzner [18] and Sachs [85] which were part of the *Gravitational Waves in General Relativity* programme initiated by Bondi in the late 1950s. These developments were of fundamental importance to the understanding of gravitational waves and with the advancement of computational technology, it was recognised that the characteristic formalism holds several computational benefits. Among these are: the fact that the EFEs simplify to ordinary differential equations along characteristics, which are less expensive to compute, and the conformal method, developed by Penrose [76], which can be used to represent infinity on a finite grid, making modelling asymptotical behaviour possible in full non-linearity. The one major drawback of null cone coordinate systems is the vulnerability to non-uniqueness and singularities in the presence of caustics. In astrophysical problems, this is usually treated by combining the characteristic formalism with the Cauchy formalism where the latter is used to solve regions where caustics are expected while the former is used to extract the solution to the far field [9]. Treating caustics directly on the null cone has been investigated [46] but this approach has not been implemented numerically. A comprehensive overview of characteristic numerical relativity can be found in [101].

Although the propagation of radiations of cosmological observations and gravitational waves both occur on null cones, the characteristic formalism has rarely been employed for investigating cosmological problems. The most probable reasons for this are that noncomoving coordinates are not popular in cosmology and the cosmological PNC converge at the apparent horizon (AH), which causes the radial coordinate (diameter distance) to become multi-valued. Nevertheless, some research has been done. In 1976 and 1981, Chellone used the Bondi-Sachs metric to investigate the FLRW model and found it advantageous for investigating inhomogeneities in the early universe using perturbation methods [26, 27]. In 1985, Ellis et al [36] proposed the Bondi-Sachs CIVP as a method for evolving from an initial PNC setup using the Newman Penrose formalism. This was never implemented and subsequent work was done using the fluid-ray tetrad formalism, which was specifically designed for their research. More recently in 2004, Ishak [53] used the Bondi-Sachs metric to investigate the observational cosmology problem with emphasis on advantages of noncomoving coordinates. In 1996, Bishop & Haines [12] published a axi-symmetrical implementation for the Einstein-de Sitter model. The work presented in this thesis is a continuation of their work and has been published in [97] and [98]. Here, we develop a model for spherical symmetric, inhomogeneous, dust universes with a cosmological constant and, using an affine parameter as radial coordinate, we do calculations beyond the AH.

## 1.2 Chapter outline

A general overview of cosmological models, observations and their relation to the PNC is given in Chapter 2. Of particular importance is the distinction between the parameterized and observational models which forms the basic argument towards the developments in this thesis. As an

illustration of a parameterized model, an overview of the  $\Lambda$ CDM model, which is relevant to the current understanding of the Universe, is given and the observational evidence for the model is discussed. The LTB model is then described as a parameterized model with inhomogeneities. This is followed by an introduction to observable models by the description of observable quantities on the PNC followed by a review of two existing observational models. The requirements of the model presented in the later chapters concludes this chapter.

Chapter 3 presents the theoretical developments towards a null cone model of the observable universe intended for calculations using NR. Based on the Bondi-Sachs CIVP, geometric (hypersurface) and energy-momentum (evolution) equations are derived for spherically symmetric dust cosmologies, which is the requirement for the cosmological models that will be investigated in this work. The diameter distance, which is the radial coordinate of the Bondi-Sachs model, is however only suitable for calculations prior to the PNC converging and approaching this region the method becomes inaccurate. To address this problem, a new model is derived where the radial coordinate is replaced by an affine parameter on the PNC. This model is suitable for calculations up to redshifts well beyond the AH with the inclusion of a cosmological constant.

A code was developed for calculations and simulations on these CIVP models and this is the topic of Chapter 4. For this, an explicit second order algorithm, previously developed in [10, 11] for modelling gravitational waves, was adapted for the cosmological problem. The original codes did not consider the region at and in the vicinity of the cone vertex, which is not of importance in gravitational wave modelling. In the observable universe, this is the position of the observer and special considerations are required since the GW model contains coordinate singularities here. These are treated by using series expansions around the observer position.

Chapter 5 presents the results obtained for various runs of the code where both homogeneous and inhomogeneous models are modelled. Exact and numerical calculations derived in the previous chapters for known solutions are used to measure the codes accuracy and stability and these are presented here. After showing that the code is sufficiently accurate and stable, two numerical experiments are presented, which demonstrate an interesting application of the model where it can be used to verify the physical consistency of different models given similar initial values.

Finally the synthesis of the work is presented in Chapter 6. In summary the code developed was able to simulate the required models adequately. Furthermore, some possibilities for future research with the developments done here as basis are mentioned.

### 1.3 Conventions and units

This thesis combines developments in cosmology with developments in NR where different notations are preferred and some clashes in symbols occur. Instead of inventing new notation or converting the notation of one field to the other's, the notation of recent developments in the particular fields are used. Moreover, Chapter 2, which is exclusively a review of existing work in cosmology, uses notation used in texts in cosmology such as [100, 35] while Chapter 3, which presents developments based on NR, preference is given to the notation of NR used in [10, 11].

Changes in symbols that might cause confusion are clearly pointed out in the text and Appendix A is included as a summary of the symbols in their specific contexts. Clashes in the use of symbols are mostly limited to the use of  $r$  as the radial coordinate. In Chapter 2,  $r$  will

be used as the comoving radial distance which clashes with the use in the remaining text where  $r$  will be used as the diameter distance in null coordinates. In places where both symbols are required,  $r$  will be the diameter distance and  $\tilde{r}$  the comoving distance. It is clearly pointed out in the text where the use of  $r$  changes. The use of different notation is mostly limited to the presentation of differentiation symbols. For differentiation, partial derivative are denoted by  $\partial$  or a comma “,” and covariant derivatives by  $\nabla$  or a semi-colon “;”. Spatial derivative are indicated as  $A' = A_{,r}$  and temporal derivatives  $\dot{A} = A_{,t}$ . The choice of convention used is based on the prominence in literature e.g. the comma notation is more prominent in NR while the  $\dot{A}$  and  $A'$  notations are more common in cosmological references.

Geometrised units:  $G = c = 1$ , where  $G$  is the gravitational constant and  $c$  is the speed of light are mostly used. The few cases where the values of these constants have significance are pointed out at the places where they are used. The signature  $(-, +, +, +)$  for the metric  $g_{ab}$  is exclusively used. Following the convention of *abstract index notation* used in [100, 35], apart from the standard rules for tensor indices, Latin indices  $(a, b, c \dots)$  are used in expressions where no choice of coordinate are made while expressions in terms of coordinates are made make use of the Greek alphabet  $(\alpha, \beta, \delta \dots)$ . The summation rule for tensors is followed where the  $\Sigma$  symbol is implied when superscript and subscript indices are repeated.

## Chapter 2

# Cosmology and the PNC

The distinction between parameterized and observational models was made in Chapter 1 and this chapter explores the theoretical aspects of these two approaches in more detail. After introducing some general concepts, the  $\Lambda$ CDM model is described as a parameterized model with a summary of the observational requirements and evidence for substantiating this model. The inhomogeneous Lemaître-Tolman-Bondi model is then introduced as a more complicated class using the parameterized approach. The topic which forms the basis of the developments in this thesis, the observational approach to cosmology, follows by introducing the observable quantities from observations on the PNC. A brief summary of two existing observational models is then given as a conceptual illustration of the observational approach. The descriptions that follow give mathematical summaries of the theoretical aspects by repeating the most relevant formulae to substantiate concepts; none of these are newly derived. Further, it should be borne in mind that most the topics in this chapter are riddled with subtleties that are beyond the scope of this thesis and can be found in the references given.

## 2.1 Modelling the Universe

### 2.1.1 Relativistic cosmology

In relativistic cosmology, the theoretical basis for modelling the large scale Universe is General Relativity and its mathematical foundation, Riemannian geometry. Together with these, assumptions and choices of reference frames have to be made to relate observations in a manageable way to our theoretical expectations. Accordingly, these topics are treated in detail in standard texts such as [35], [72], [100], [48], [44] and many others. In this section, a few highlights are given on the most relevant of these for the current work. Besides providing the foundations for development later in this thesis, this will also be used to fix terminology and notation.

#### Assumptions

In Section 1.1, limitations of our ability to observe the Universe were discussed. The most fundamental of these is the fact that, light travels at a finite speed and therefore, the observable

universe is restricted to the region where light could have reached us within the age of the Universe. In addition, we view the Universe from inside, at one location and effectively only one point in time. In contrast to laboratory experiments, we cannot manipulate the object of investigation or repeat the experiment. Regardless of theoretical and technical complications, making simplifying assumptions is an inevitable part of the way that we interpret theory and observations in cosmology.

The *cosmological principle* is the cornerstone assumption of cosmology. This is a simplifying postulate proposing that on a sufficiently large scale, there is uniformity in the properties of the Universe i.e. the Universe looks the same to all observers. Firstly, the uniformity refers to the physical laws of nature as we perceive them locally. This has the implication that, similar to an experiment repeated in different Earth based laboratories, there is repeatability in observations of the Universe irrespective of the location of the observer (see [17] for a more elaborate argument pp. 11–15). While this is a very bold extrapolation of our understanding of nature, which cannot be verified from only one spacetime location, without it we can say very little about the Universe.

The second aspect of the cosmological principle is the assumption of uniformity in kinematic and dynamic properties i.e.: the expansion rate and the distribution of matter. This can be substantiated through the *Copernican principle* that states that we are not in a privileged location in the Universe: a local observer is a *fundamental observer* representing any other observer in the Universe. Together with the observational evidence indicating a high level of isotropy, it is then concluded that the distribution of matter and spatial expansion is homogeneous. This part of the assumption is not essential for understanding the Universe and with more precise observations than currently available it is a testable hypothesis.

A further assumption that simplifies the description of the Universe is the *smooth-fluid approximation* whereby the matter content of the Universe is represented by a continuous fluid. Accordingly, the largest structures in the Universe, galaxy super clusters, are regarded to be small enough compared to the overall size to be considered particles of the *cosmological fluid*. It is further assumed that the fluid is well behaved: the fluid particles move along well defined laminar stream lines (world lines) and is only affected by gravity. For a fluid to behave in this well-ordered way, it has to consist of Newtonian dust, i.e. a pressureless fluid.

## Riemannian geometry

In General Relativity, spacetime is described by a four dimensional pseudo-Riemannian manifold  $(M; g)$  with  $M$  a differential manifold and  $g$  a non-degenerate, smooth, symmetric metric tensor which is not positive definite. On the manifold a vector space  $\mathcal{T}_p(M)$  can be formed at each point  $p$ , which consists of the set of all tangent vectors,  $\mathcal{T} \in \mathcal{T}_p$ , at the arbitrary point  $p$ .  $\mathcal{T}_p$  is an important structure for evaluating curves on the manifold and also intrinsically related to the way that coordinates are defined on  $M$ .

In tensor index notation on a coordinate system (e.g.  $x^\mu$ ), the metric can be represented as a line element related to infinitesimal coordinate displacement as

$$ds^2 := g_{\mu\nu} dx^\mu dx^\nu. \quad (2.1)$$

In order to relate the connection between vectors in tangent spaces on  $M$ , an affine

connection, the *Christoffel symbols*, is formed from  $g_{ab}$

$$\Gamma^d{}_{bc} := \frac{1}{2}g^{da}(g_{ab,c} + g_{ac,b} - g_{bc,a}). \quad (2.2)$$

Without  $\Gamma$  it is not possible to determine if two vectors are distinct or the same at two points,  $p$  and  $q$  in vector spaces  $\mathcal{T}_p$  and  $\mathcal{T}_q$ , on  $M$  [100].  $\Gamma$  provides a utility to define covariant differentiation on  $M$ , for instance for a vector in curved spacetime

$$v^a{}_{;b} := v^a{}_{,b} + \Gamma^a{}_{cb}v^c. \quad (2.3)$$

The concept of curvature in Riemannian geometry is related to the non-commutativity of the second order covariant derivatives of a vector. This can be written in terms of  $\Gamma$  and its derivatives as the *Riemann curvature tensor*

$$R^d{}_{abc} := \Gamma^d{}_{ac,b} - \Gamma^d{}_{ab,c} + \Gamma^d{}_{ec}\Gamma^e{}_{ab} - \Gamma^d{}_{eb}\Gamma^e{}_{ac}. \quad (2.4)$$

For flat space-time  $R^d{}_{abc} = 0$ . By the contraction of  $R^d{}_{abc}$ , the *Ricci tensor* is formed

$$R_{ab} := R^c{}_{abc}, \quad (2.5)$$

which is also  $R_{ab} = 0$  for flat spacetime and further contraction defines the *Ricci scalar*

$$R := g^{ab}R_{ab}. \quad (2.6)$$

$g_{ab}$ ,  $\Gamma^d{}_{bc}$ ,  $R^d{}_{abc}$ ,  $R_{ab}$  and  $R$  are the geometric components required by the Einstein field equations.

A geodesic is defined as the curve whose tangent is parallel propagated along itself, giving the intuitive notion of the shortest path in a curved geometry [100]. For a curve with a tangent  $\mathcal{T}^a$  to be a geodesic it has to satisfy

$$\mathcal{T}^a\nabla_a\mathcal{T}^b = \alpha\mathcal{T}^b \quad (2.7)$$

with  $\alpha$  an arbitrary function on the curve. It can further be shown that there exists a class of parameters such that the tangent vector has constant magnitude for which the reparameterization of (2.7) follows as

$$\mathcal{T}^a\nabla_a\mathcal{T}^b = 0. \quad (2.8)$$

These parameters are called *affine parameters* ( $v$ ) and have the property that all affine parameters of a curve are linearly related. By choosing a specific coordinate system, e.g.  $x^\mu$ , (2.8) can be written as

$$\frac{d^2x^\mu}{dv^2} + \Gamma^\mu{}_{\nu\sigma}\frac{dx^\nu}{dv}\frac{dx^\sigma}{dv} = 0. \quad (2.9)$$

A crucial point follows from the theory of ordinary differential equations. This is formalised as the local existence and uniqueness theorem for geodesics [73] (p. 216).

**Theorem 1 (Existence and uniqueness of geodesics)** *Let  $(M; g)$  be a Riemannian manifold. If  $p \in M$  and  $v \in \mathcal{T}_p(M)$  then there exists an open interval  $I = (-\epsilon; \epsilon)$  and a unique geodesic  $\alpha : I \rightarrow M$  such that  $\alpha(0) = p$  and  $\dot{\alpha}(0) = v$ .*

The local existence and uniqueness properties of geodesics together with affine parametrization make them particularly useful as coordinates. This is a key facet in the developments followed in this thesis.

## General Relativity

General Relativity describes the interaction of geometry and matter through the Einstein field equations (EFEs),

$$R_{ab} - \frac{1}{2}R g_{ab} + \Lambda g_{ab} = \kappa T_{ab} \quad (2.10)$$

where  $R_{ab}$  is the Ricci tensor,  $R$  the Ricci scalar,  $T_{ab}$  the stress tensor,  $\Lambda$  the cosmological constant and  $\kappa = 8\pi G/c^2$ . The left hand side of the equations are the geometric terms while the righthand side the energy-matter term.

For the models considered in this work, matter is taken to be Newtonian dust for which the stress tensor is  $T_{ab} = \rho u_a u_b$ . Since the stress tensor is particularly simple, the form of the EFEs mostly used in this work is

$$R_{ab} = \kappa \left( T_{ab} - \frac{1}{2}T g_{ab} \right) + \Lambda g_{ab} \quad (2.11)$$

where  $T = -\rho$ , the contraction of  $T_{ab}$ . In addition to its role in the EFEs, the stress tensor also determines the relativistic conservation equations through  $\nabla^a T_{ab} = 0$ .

In General Relativity, the sign of  $g_{\mu\nu}x^\mu x^\nu$  is related to the causal connection to a spacetime event according to

$$g_{\mu\nu}x^\mu x^\nu \begin{cases} < 0 & \text{time-like} \\ = 0 & \text{null} \\ > 0 & \text{space-like} \end{cases} . \quad (2.12)$$

where  $x^\sigma \in \mathcal{T}_p$ . Time-like curves define the paths of objects with mass while null curves define the paths of particles without mass (e.g. photons). Space-like curves define paths between points which are not causally connected [44].

## Kinematics

As a problem in relativistic fluid dynamics, there is a well defined 4-velocity following the path of world lines, defined as

$$u^\mu := \frac{dx^\mu}{d\tau} \quad (2.13)$$

with  $\tau$  the proper time.  $u^a$  defines the paths of objects with mass moving under the influence of gravity alone. A direct implication of (2.13) is the normalisation of  $u^a$ :

$$u^a u_a = -1, \tag{2.14}$$

which in turn implies

$$\dot{u}^a u_a = 0. \tag{2.15}$$

In summary, the *fundamental 4-velocity* ( $u^a$ ) is defined as the tangent vector to a time-like geodesic world line, affinely parameterized by the proper time ( $\tau$ ).

## Coordinates

In terms of the cosmological fluid, the most convenient frame of reference is *comoving synchronous* (CS) coordinates. Accordingly, the time coordinate,  $t$ , is an affine parameter defined on the cosmic fluid's particle world lines, which are time-like geodesics. Under certain conditions (see [35] p.84), the time parameter on the world lines can be synchronised such that simultaneous events on different world lines can be represented by a unique *cosmic time*, connecting hypersurfaces where  $t = \text{constant}$  [35, 68]. Under the cosmological principle, space-like homogeneous hypersurfaces connect the corresponding time intervals on neighbouring world lines i.e. *homogeneity is defined on  $t = \text{constant}$  surfaces* and a radial coordinate (usually  $r$ ) measures instantaneous distance on these surfaces. Furthermore, the coordinates are to expand with the Universe and all galaxies remain stationary relative to each other in CS coordinates. CS coordinates are, however, not aligned with observations since  $r$  is defined on space-like hypersurfaces. To incorporate direct observations, transformations are required to obtain events on the PNC corresponding to  $t = \text{constant}$  surfaces. Alternatively, the coordinate system can be adapted to correspond to null hypersurfaces, which are intrinsically not synchronous. Such a null coordinate system will be developed in this thesis.

### 2.1.2 Model dependence in cosmology

The purpose of cosmology is to search for the cosmological model that has the best agreement with observed phenomena. It has already been pointed out that we have to rely on assumptions to make cosmology a manageable endeavour. However, from a scientific point of view, there should be as few assumptions as possible. In cosmology, this will require that the interpretation of the observations should be independent of the model it substantiates. For reasons already mentioned in Section 1.1.2, this is not the standard procedure in cosmological developments. Nevertheless, models following the concept of idealised observational cosmology have been developed (see [36]) and a comparison between assumptions and model independence provides useful insight into the study of cosmology. Much of the structure of this chapter is based on this argument and a brief outline of how it will be presented is given here.

## Standard model

Assuming the the cosmological principle, the Universe is modelled as a FLRW model and current observations favour a hot Big Bang universe. Besides direct observations, indirect evidence also plays an important role in substantiating this model. For instance, in the early hot universe processes such as baryogenesis and nucleosynthesis substantiate the observed ratios of matter and elements while in the very early universe, cosmic inflation accounts for almost exact flatness beyond causal horizons, which is observed in the CMB and its anisotropies. More recently, direct observations of Type Ia supernovae (SNIa) added justification for the presence of a cosmological constant in these models and the  $\Lambda$ CDM model, which will be described in Section 2.2.1, is currently the standard model in cosmology. Effectively, the assumed universe with some adjustments provides remarkable correspondence to observations and since the Universe is assumed to be homogeneous, local effects can be extrapolated to the rest of the Universe. However, much of the interpretation of observations is dependent on the assumed geometry of the model.

## Inhomogeneous cosmologies

Instead of assuming homogeneity, we can assume a more general model such as the LTB model, which makes provision for radial inhomogeneities. This model has more freedom in parameters and can be made to fit a larger set of observations than the FLRW models. Through the adjustment of parameters, this model can also account for observed phenomena but requires the observer to be very close to the centre of a region where the conditions are suitable to fit isotropic observations. There are possibly many models that can fit observations and deciding which of them are real and which are contrived is not a trivial matter, if it can be determined at all. More general models also encounter these problems. The LTB model, which represents these type of models will be the topic of Section 2.2.2.

## Observational models with symmetries

Since cosmologies such as the LTB model assume specific surroundings around the observer, the observer's point of view can, strictly, not be extrapolated beyond the observable universe. An observational representation, where observations determine the metric, of the LTB model is required to make the model more specific. This mostly makes use of model independent observations. It will, however, be difficult to ignore the predictions of dark matter and dark energy following from the standard model and these will have to be assumed or alternative explanations for their apparent presence should be introduced. Observational models do not attempt to explain the Universe prior to the CMB. The models described in Sections 2.3.2 and 2.3.3 and the model developed in Chapters 3 and 4 are examples of such models.

## Ideal observational cosmology

Model selection using the observational approach can be generalised to the point where only a theory of gravity is assumed and no unobservable matter or symmetries are assumed. This will, however, require a very precise map of the Universe, which is unlikely to be obtained in the near future, and assumes that observable objects are representative of unobservable

objects. This type of approach, assuming ideal observational data, is of importance to explore the fundamental theoretical limits of determining the geometry of the observable universe and was used in [36] to prove Theorems 4 and 5 (Section 2.3.3 on page 41).

## Cosmography

Cosmography attempts to only use observations to determine the geometry of spacetime (e.g. see [99]). Here, it is assumed that our understanding of geometric optics is valid in the rest of the Universe but no theory of gravity is assumed. It was shown in [36] that this approach is fundamentally restricted (see Theorem 4, Section 2.3.3 on page 41) and cannot be used to determine the spacetime structure of the observable universe. On the other hand, if the EFEs with evolution equations are combined with the cosmographical data, the past Cauchy development of the PNC can be determined uniquely. Therefore, cosmography measured over a long enough period to determine  $d/dt$  of any observable quantity, can be used to test the dynamics of the EFEs and evolution equations.

## 2.2 Parameterized models

### 2.2.1 Standard model - $\Lambda$ CDM

The  $\Lambda$ CDM is used as an example of a parameterized model. This model is currently accepted as the standard model in cosmology and is, therefore, the most relevant homogeneous cosmology to consider. Mathematically, the geometry of a homogeneous universe in CS coordinates is fully described by the Robertson-Walker (RW) line element

$$ds^2 = -dt^2 + a^2(t) \left( \frac{dr^2}{1 - kr^2} + r^2(d\theta^2 + \sin^2\theta d\varphi^2) \right). \quad (2.16)$$

The coordinates are synchronous in time with  $t$  the proper time on an observer's world line. All observers were synchronised at  $a(0) = 0$  and spatial co-moving hypersurfaces are defined by corresponding  $t = \text{constant}$  instances on all world lines. On these hypersurfaces,  $r$  is the radial coordinate with  $\theta$  and  $\varphi$  the spherical latitude and longitude angles.  $a(t)$  is a scale factor of spatial expansion.  $k$ , is a curvature index representing closed, open or flat spatial section by taking on the values 1,  $-1$  or 0 respectively. By adjusting  $a(t)$  and  $k$ , all possible homogeneous geometries can be described by this metric.

The EFEs (2.10) relate the geometry to the energy-matter content where  $T_{ab}$ , because of the imposed isotropy, takes the form of a perfect fluid

$$T_{ab} = (\rho + p)u_a u_b + pg_{ab} \quad (2.17)$$

where  $\rho$  is the energy-density,  $p$  the pressure and  $u_a$ , the covariant velocity.

Substituting the metric, (2.16), and the energy-density tensor, (2.17), into the EFEs (2.10), two important equations follow. The Friedman equation,

$$\left( \frac{\dot{a}}{a} \right)^2 = \frac{\kappa\rho}{3} + \frac{\Lambda}{3} - \frac{k}{a^2}, \quad (2.18)$$

and the Raychaudhuri equation

$$\frac{\ddot{a}}{a} = -\frac{1}{6}\kappa(\rho + 3p) + \frac{\Lambda}{3}. \quad (2.19)$$

These describe the expansion and acceleration in expansion of the Universe for a specific energy-density distribution, curvature and cosmological constant.

By differentiating (2.18) and eliminating  $\ddot{a}$ , using (2.19), the energy-density conservation equation is obtained as

$$\dot{\rho} = -3\frac{\dot{a}}{a}(\rho + p). \quad (2.20)$$

This can also be derived by substituting (2.17) into the relativistic conservation equation  $\nabla^a T_{ab} = 0$ .

To solve the system (2.18), (2.19) and (2.20), one additional equation is required. The equation of state defined as  $p(\rho) = w\rho$ , provides the necessary closure. Relevant values for  $w$  are:  $w = 0$  for matter (as Newtonian dust) and  $w = 1/3$  for radiation and  $w = -1$ .<sup>1</sup>

### Cosmological parameters

The FLRW model can be solved analytically for the three cases of curvature,  $k = -1, 0$  or  $1$ , and since the spatial curvature is constant, it is only necessary to determine  $k$  at one instant in time. By definition,  $\Lambda$  is also constant and therefore also a single value parameter, which has to be determined at a single epoch. The required solution,  $a(t)$  and  $\rho(t)$  can be obtained from (2.18) and (2.20) while (2.19) can be used to constrain the values of  $k$  and  $\Lambda$ .

The procedure towards a solution introduces cosmological parameters, which can be determined from their values at  $t_0$ , the current time. The Hubble rate is defined as

$$H(t) = \frac{\dot{a}(t)}{a(t)} \quad (2.21)$$

and the Hubble constant,  $H_0$ , the value at  $t_0$ , which can be determined from redshift-distance relations.

The density parameter is introduced as the ratio of the density against the critical density ( $\rho_c = 3H_0/\kappa$ ) required for the Universe to be spatially flat (i.e.  $k = 0$ ). This provides a value for each density component. With

$$\Omega_{m0} = \frac{\kappa\rho_{m0}}{3H_0^2}, \quad \Omega_{\Lambda0} = \Omega_{\Lambda} = \frac{\Lambda}{3H_0^2}, \quad \Omega_{k0} = \Omega_k = -\frac{k}{a_0^2H_0^2}. \quad (2.22)$$

Since  $\Omega_k$  and  $\Omega_{\Lambda}$  are constants, it is only necessary to determine their value at  $t_0$  while  $\Omega_{m0}$  will provide the initial value for (2.20). Rewriting (2.18) in terms of the density parameters gives

$$H^2 = H_0^2 \left( \frac{\Omega_{m0}}{a^3} + \Omega_{\Lambda} + \Omega_k \right), \quad (2.23)$$

---

<sup>1</sup>As an alternative to an explicit cosmological constant, a fluid with  $w = -1$  can be introduced, which provides a form of equations (2.18) and (2.19) in terms of a vacuum energy  $\rho_{\Lambda}$ , with  $\Lambda = \kappa\rho_{\Lambda}$ .

and for the current time  $t_0$

$$\Omega_k = \frac{\Omega_{m0}}{(a_0)^3} + \Omega_\Lambda - 1. \quad (2.24)$$

From this equation, knowing two of the density parameters and  $a_0$  will determine the other one.

Another parameter in terms of  $t_0$  that can be obtained from (2.18) and (2.19) is the deceleration parameter

$$q_0 = \left( -\frac{a\ddot{a}}{\dot{a}^2} \right)_0 = \frac{1}{2}\Omega_{m0} - \Omega_\Lambda. \quad (2.25)$$

An important aspect of this equation is that the expansion of the Universe cannot accelerate without the presence of a form of vacuum energy.

## Observations and concordance

Since the discovery of the recession of galaxies in the 1920s, measuring  $H_0$  has been the most important endeavour in cosmological observations. It is evident from the previous section that  $H_0$ , is required for determining all the other cosmological parameters. Its importance is of such significance that it was one of the design objectives of the Hubble Space Telescope (HST).<sup>2</sup> As a Hubble Key Project, the objective was to determine  $H_0$  within an error margin of 10%. Since the recession of galaxies can directly be determined from  $z$ , measuring  $H_0$  comes down to accurately measuring distance in space. Towards this goal, Cepheid variable stars were used as measure for low redshifts and primary measure to calibrate secondary measures such as the Tully-Fischer relation and Type Ia supernovae (SNIa) for high redshifts. The end result was  $H_0 = 72 \pm 8 \text{ km s}^{-1} \text{ Mpc}^{-1}$  (see [45] for more details).

In the 1960s, together with the evidence of expansion, three other observations provided support for the idea that the Universe evolved from an initial hot dense state. Radio galaxies were observed to be more prevalent at higher redshifts, which supports the idea that the Universe is evolving. The CMB was detected and its existence and the temperature it represents corresponded to the predictions of the Big Bang theory. It was also found that observed abundances of light elements (hydrogen, helium-4, deuterium and lithium), closely followed the predictions of the Big Bang theory at the observed temperature of the CMB. The history of these developments is described in [58] (pp. 319–335).

As detailed observations became available in the 1990s, the structure of the CMB provided further refinement to support a FLRW model. The isotropy of the CMB is a strong argument for homogeneity in the Universe and assuming then that the fluctuations in the CMB are the result of structural fluctuations in the very early Universe, the acoustic peaks in the spectrum can be used a standard ruler of distance on the last scattering surface. Comparing CMB fluctuations with the expected values for closed, flat and open spatial geometries, evaluation of the first acoustic peaks of both the COBE and WMAP data strongly favours the flat geometry i.e.  $\Omega_0 \approx 1 \Rightarrow \Omega_k \approx 0$ . In addition, combining the CMB data with data of galaxy surveys give further evidence for this. This provides a very useful simplification of equation (2.24).

---

<sup>2</sup>The size of the HST mirror was determined by the requirement of observing faint Cepheids in the Virgo cluster.

Observations of the gravitational effect of matter gives an estimation of  $\Omega_{m0}$ . The rotation of galaxies in clusters, rotation of stars in galaxies, the temperature of galaxies through X-ray observations and the effect of gravitational lensing all point to a value of  $\Omega_{m0} \approx 0.3$ . However, the quantity of baryonic matter inferred from deuterium abundance and differences in the fluctuation peaks in the CMB corresponds to only  $\Omega_B \approx 0.05$ . The deficit to obtain  $\Omega_{m0} \approx 0.3$  is made up of cold dark matter ( $\Omega_{CDM}$ ), of which only the gravitational evidence is detected. Simulations of structure formation is taken as further evidence for this.

Having  $\Omega_{m0} \approx 0.3$ , from equation (2.24) the vacuum energy or cosmological constant component is expected to be  $\Omega_\Lambda \approx 0.7$ . Otherwise, our understanding of the Universe through a number of assumption is seriously flawed, which is not an entirely remote possibility since accounting for missing energy by introducing a cosmological constant is not sufficient evidence for claiming that 70% of the energy-density content of the Universe is of an unknown type. This should also be viewed from the fact that theoretical predictions from quantum mechanics favours a value  $10^{120}$  time larger. Equation (2.25) comes into play here since a positive  $\Omega_\Lambda$  component will be observable from a negative value of  $q_0$ . SNIa observations from the *High-Z Supernova Search Team* and *Supernova Cosmology Project* provided substantiating evidence for an accelerating Universe and the value  $\Omega_\Lambda \approx 0.7$  fits the observations very well [77, 83].

The parameter values  $\{H_0, \Omega_k, \Omega_{m0}, \Omega_\Lambda\} = \{72, 0, 0.3, 0.7\}$  describes the simplest cosmological model that is in agreement with all observational evidence. This is known as the Concordance, Standard or  $\Lambda$ CDM model. Observational evidence, for this model, follows from measurements designed to determine the parameters separately and also measurements where combined values of the parameters are determined. Considerable evidence for the model comes from CMB, SNIa and HST data. Theoretical hypotheses of the Universe earlier than the LSS, such as cosmic inflation and baryogenesis, are also in agreement with the processes expected in the hot dense early stages of the  $\Lambda$ CDM model. Therefore, the majority of modern cosmological research centres around refining and further substantiating this model.

### $\Lambda$ CDM solution

Having  $\Omega_k = 0$ , then  $\Omega_\Lambda = 1 - \Omega_{m0}$  and equation (2.23) can be written in terms of the cosmological parameters as:

$$H^2 = H_0^2 \left( \frac{\Omega_{m0}}{a^3} + 1 - \Omega_{m0} \right) \quad (2.26)$$

With a variable substitution  $h = ((1 - \Omega_{m0})/(\Omega_{m0}))^{1/2} a^{3/2}$ , equation (2.26) becomes a standard integral with the solution:

$$a(t) = \left( \frac{\Omega_{m0}}{1 - \Omega_{m0}} \right)^{1/3} \left( \sinh \left[ \frac{3}{2} H_0 (1 - \Omega_{m0})^{1/2} t \right] \right)^{2/3}. \quad (2.27)$$

With some rearrangement and scaling to  $a(t_0) = 1$ , the age of the Universe is obtained as: <sup>3</sup>

$$t_0 = \frac{2}{3}H_0^{-1}(1 - \Omega_{m0})^{-1/2} \sinh^{-1} \left[ (1/\Omega_{m0} - 1)^{1/2} \right]. \quad (2.28)$$

The density distribution in terms of  $H_0$  and  $\Omega_{m0}$  is:

$$\rho_m = \frac{3H_0^2}{\kappa} \frac{\Omega_{m0}}{a^3}. \quad (2.29)$$

## 2.2.2 Lemaître-Tolman-Bondi model

### Inhomogeneous universes

The largest galaxy surveys show that inhomogeneities are prevalent as gravity causes matter to clump together resulting in a web of walls separated by large voids. However, it is assumed that on some even larger scale, inhomogeneities average out and their effects are negligible. Mathematically, relaxing the assumption of homogeneity provides a larger class of models of which the FLRW universes are three specific cases to which more complicated models can degenerate. Inhomogeneous models can therefore be used to model the Universe on the scales where inhomogeneities are not negligible and models can be constructed that degenerate to the FLRW cases on the scales where homogeneity is expected. On the other hand, inhomogeneous models can also be constructed that are significantly different to the standard model and provide alternatives where questions can be asked such as: What if the effects of inhomogeneities are not negligible? Can the apparent cosmic acceleration be explained using only inhomogeneities? Research on these questions has provided interesting alternatives for dark energy as the cause of the appearance redshift dimming of SNIa. The essence of these investigations was put forward in [71] where it was shown that any set of isotropic observations for a spherical symmetric geometry can be matched by some selection of source evolution functions (this is discussed in more detail in Section 2.3.2).

The most commonly used inhomogeneous models for investigating SNIa dimming are: lumpy universe, backreaction and local void or hump models. *Lumpy universe* models are models where inhomogeneities between the observer and observed object affects observations. The Swiss-Cheese model, where spherical regions are repeatedly cut from an otherwise FLRW universe and then filled with another spherical model is an example which has been shown in [54] to have a significant effect on the distance-redshift relation of SNIa. Another lumpy universe model, the Roeder & Dyer model, has been demonstrated in [62] to account for apparent dark energy. *Backreaction* models work on the principle that averaging the EFEs over nonlinear perturbations will induce an effective energy-momentum tensor with a nearly constant magnitude which will have the appearance of a cosmological constant [34]. *Local void* models make use of the observation that there exist nearly empty regions in the Observable Universe where the expansion is faster than that of the greater Universe and then suppose that we are located near the centre of such a bubble. This model has been used in [40], [47], [69], [55], [42] and many others as alternatives to cosmic acceleration. These models are, however, mostly illustrations of the fact that scenarios containing inhomogeneities can account for the dimming of SNIAs with

---

<sup>3</sup>This scaling affects the value of  $k$ , since the model was already normalised to have  $k = -1$ ,  $k = 0$  or  $k = 1$  from the general case  $k < 0$ ,  $k = 0$  or  $k > 0$ . However, since  $k = 0$  for the  $\Lambda$ CDM mode, it does not affect the particular solution.

redshift.

The simplest inhomogeneous model is the the Lemaître-Tolman-Bondi (LTB) model, which represents an isotropic, dust filled, inhomogeneous universe. This is on appearance a minor variation of the FLRW model with a relaxation of the homogeneity assumption on the radial coordinate. Mathematically, the LTB metric can be presented as a generalisation of the RW metric by replacing products with  $(r)$  of the scale factor  $(a(t))$  and the curvature index  $k$  by more general functions:  $\{a(t)r, kr\} \rightarrow \{R(r, t), k(r)\}$  [40]. Alternatively, the FLRW model is a specific case of the LTB model. The LTB model has exact analytical solutions which makes it a useful tool to investigate the mathematical significance inhomogeneities in the Universe. This model is also useful to investigate homogeneous universe models on the scales where inhomogeneities are not averaged out as well as more complex inhomogeneous models which are made up of superimposed symmetrical inhomogeneous regions.

On a physical and philosophical level the addition of inhomogeneities has more fundamental consequences and the LTB model, in its basic form, is not popular as a physically realistic model. Opposition mostly comes from the fact that it is in conflict with the Cosmological and Copernican principles where isotropy implies homogeneity. Conversely, an isotropic inhomogeneous universe implies that the observer is in a special location, in particular, very close to the centre of the Universe. Although homogeneity cannot, in principle, be verified because it requires observational access to the entire Universe, the coincidence of the Earth being in the centre of the Universe is not a philosophically appealing idea. Observationally, however, bearing in mind that our view of the Universe is restricted to our PNC, an observer placed at the centre of the observable region can correspond to an observed LTB region. The LTB model can also be used in Swiss-Cheese models where it is used to fill the regions cut out in an otherwise FLRW universe.

## LTB model

In the LTB model, the assumption of universal homogeneity is relaxed on the radial coordinate and the general form of the metric in CS coordinates for an irrotational cosmic fluid is defined as (see for instance [15], [38] and [78])

$$ds^2 = -dt^2 + U^2(t, r)dr^2 + R^2(t, r)\{d\theta^2 + \sin^2 \theta d\varphi^2\}. \quad (2.30)$$

Where  $U$  and  $R$  are scaling functions related to the expansion of the Universe. When substituting (2.30) into the EFEs for dust ( $p = 0$ ),  $U$  can be written in terms of  $R$  and the metric becomes

$$ds^2 = -dt^2 + \frac{[R'(t, r)]^2}{1 + 2E(r)}dr^2 + R^2(t, r)\{d\theta^2 + \sin^2 \theta d\varphi^2\}. \quad (2.31)$$

Here,  $R(t, r)$  is the called the areal radius and  $4\pi R^2$  defines the proper surface area of a sphere with coordinate radius  $r$  at a constant time slice [38].  $E(r)$  is an arbitrary function of integration related to the local geometry of space-time. According to the sign of  $E$ , the geometry is classified into three categories with  $E > 0$  being hyperbolic,  $E = 0$  parabolic and  $E < 0$  elliptic.

With further manipulation of the EFEs, a Friedman equation can be derived as (see [78])

pp. 296–300)

$$\dot{R}^2 = \frac{2M(r)}{R} + 2E(r) - \frac{1}{3}\Lambda R^2, \quad (2.32)$$

the Raychaudhuri equation is

$$\frac{2}{3}\frac{\ddot{R}}{R} + \frac{1}{3}\frac{\dot{R}'}{R'} = -\frac{1}{6}\kappa(\rho + 3p) + \frac{\Lambda}{3}, \quad (2.33)$$

and the density equation

$$\frac{4\pi G}{c^4}\rho(t, r) = \frac{M'}{R^2 R'}. \quad (2.34)$$

$M(r)$  is also an arbitrary integration function and corresponds to the *active gravitational mass*, i.e. the mass contributing to the gravitational field; defined by rewriting (2.34) as

$$\frac{c^2 M(r)}{G} = 4\pi \int_0^r \frac{\rho(t, r)}{c^2} R^2(t, r) R'(t, r) dr \quad (2.35)$$

Using geometrised units,  $G = c = 1$ ,  $M(r)$  is written as

$$M(r) = 4\pi \int_0^r \rho(t, r) R^2(t, r) R'(t, r) dr. \quad (2.36)$$

Solving (2.32) for  $\Lambda = 0$  it follows that for  $E < 0$ :

$$R(t, r) = -\frac{M}{2E}(1 - \cos \eta) \quad \text{with:} \quad \eta - \sin \eta = \frac{(-2E)^{3/2}}{M}(t - t_B(r)) \quad (2.37)$$

for  $E > 0$ :

$$R(t, r) = \frac{M}{2E}(\cosh \eta - 1) \quad \text{with:} \quad \sin \eta - \eta = \frac{(2E)^{3/2}}{M}(t - t_B(r)) \quad (2.38)$$

and for  $E = 0$ :

$$R(t, r) = \left[ \frac{9}{2} M(r) (t - t_B(r))^2 \right]^{1/3} \quad (2.39)$$

with  $\eta(t, r)$  a parameter function. The function  $t_B(r)$  is called the *bang-time* function; the local time when  $R(t, r) = 0$ , which forms a non-simultaneous singular surface [71]. Considering equation (2.34),  $\rho$  becomes singular and defines the big bang singularity, which might be a singular surface, not necessarily a singular point.

The functions  $E(r)$ ,  $M(r)$  and  $t_B(r)$  determine  $R(t, r)$  and correspondingly the metric which then fully determines the model. These functions describe all radial inhomogeneous dust models and for specific choices, the FLRW models. For instance the values

$$M(r) = M_0 r^3, \quad E(r) = 0 \quad \text{and} \quad t_B(r) = \text{constant}, \quad (2.40)$$

correspond to the  $k = 0$  (Einstein-de Sitter) model. Obtaining solutions with a non-zero

cosmological constant is not as general and might require the initial data on more than one instance in time. For instance, density profiles at two instances or an initial velocity and later density profile for models with  $\Lambda > 0$  (see [13] p. 33).

A different notation used in [40] by Enqvist provides a form of the metric where the analogy with the RW geometry is directly recognisable

$$ds^2 = -dt^2 + \frac{[A'(t, r)]^2}{1 - k(r)} dr^2 + A^2(t, r) \{d\theta^2 + \sin^2 \theta d\varphi^2\}. \quad (2.41)$$

Using this notation, analogous parameters  $H_0(r)$ ,  $\Omega_k(r)$ ,  $\Omega_m(r)$  and  $\Omega_\Lambda$  were derived. This view of the model makes it more convenient to compare the LTB model to the FLRW models in Section 2.2.1 and some interesting physical implications will be pointed out in Section 2.2.2.

### LTB physical considerations

Although the FLRW models are a subclass of the LTB models, in general, radial inhomogeneity can lead to significant differences in the physical properties which cause observational ambiguities in cosmological models. Some considerations to take note of are:

- i. The function  $E(r)$  can change between hyperbolic, parabolic and elliptic solutions in the same universe and equations (2.37–2.39) are not necessarily different universes as is the case in the FLRW geometries where  $k$  measured at one spacetime event determines the curvature of the model completely.
- ii. In (2.34),  $\rho(t, r)$  can become singular at  $R(t, r) = 0$  which corresponds to the Big Bang but also when  $R' = 0$  which is called a shell crossing, a coordinate singularity probably without physical significance.
- iii. The implication of  $t_B(r)$ , the time of  $R(t, r) = 0$ , being a function of  $r$ , is that the age of the Universe is not necessarily a singular event but can be a singular surface if  $t_B(r) \neq \text{constant}$ . Nevertheless, it should be remembered that in the early Universe, a radiation model is more appropriate than the LTB model and there is no real physical significance to this surface [21].
- iv. The point where  $r = 0$  is the centre on symmetry and requires specific conditions to insure that the model is mathematically well-posed (see [78]). The models that will be used for simulations in this study have  $E(r) = 0$  and are all well-posed, which is a requirement for convergence in numerical modelling [57]. In homogeneous models the concept of a centre does not exist.
- v. In the FLRW models, surfaces of constant expansion rate and density correspond with surfaces of constant time. This is not the case with the LTB model where expansion rate and density are functions of both space and time and although symmetrical around the observer's world line, it can be irregular (see figure 2.1). The cosmological parameters are therefore functions of both  $t$  and  $r$ :  $H(t, r)$ ,  $q(t, r)$  and  $\Omega(t, r)$ .
- vi. The initial conditions are functions of  $r$  i.e.:  $R_0(r) = R(t_0, r)$  which can be derived from measurements of  $H_0(r)$  and  $\Omega_0(r)$ . Since  $r$  is defined on space-like surfaces, these

quantities will have to be determined from observations on the PNC through coordinate transformations (see Section 2.3.2).

- vii. From the presentation of Enqvist [40], an ambiguity in the concept of acceleration becomes apparent by comparing the Raychaudhuri equations (2.19) and (2.33). It is evident that in a homogeneous universe,  $\ddot{a}(t)$  is only related to the matter density and the cosmological constant. In the LTB model,  $\ddot{R}(t, r)$ , is also dependent on spatial derivatives of  $R$ . This illustrates the fact that spatial inhomogeneities can account for cosmic acceleration.
- viii. The redshift in the LTB model is also dependent on both  $t$  and  $r$ , however it is measured on the PNC where  $t$  can be written as  $t(r)$ . It can then be determined with an integral towards  $r$  as

$$\ln(1+z) = \int_0^r \frac{\dot{R}(r^*)'}{\sqrt{1+2E(r^*)}} dr^*,$$

with all functions of  $t$  rewritten as functions of  $t(r)$ .  $z$  is therefore not necessarily a clear indication of the age or distance. Without knowledge on how inhomogeneity is distributed, a statement such as: ‘a gamma ray burst at  $z=8$  was detected’ will not necessarily indicate an early Universe event.

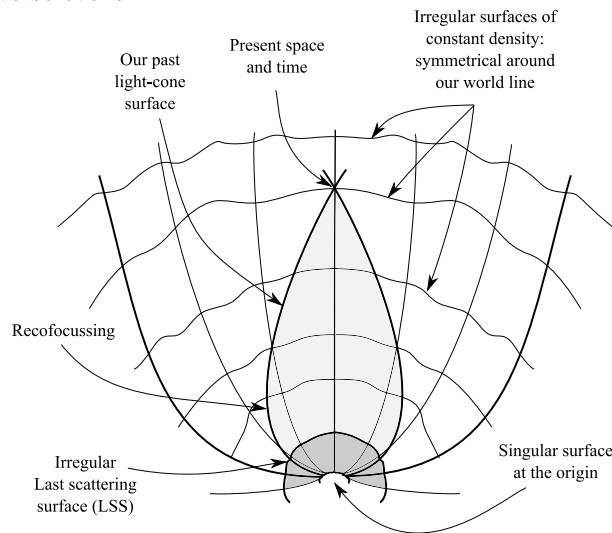


Figure 2.1: In comparison to Figure 1.1 on page 2, in an inhomogeneous isotropic universe surfaces of constant time is irregular (based on Figure 3 in [33]).

### ***Bang-time models***

Numerous LTB models exist which include the FLRW models as a subclass, other physical realistic models and also many models with uncertain physical relevance. Investigations with the code, that will be described in Chapter 4, will be limited to a simple class of LTB models referred to as *bang-time models*, which makes use of the bang time function,  $t_B$ , as a mechanism to induce inhomogeneities into a universe. By selecting simple functions for  $t_B$ , it has been demonstrated that inhomogeneities can mimic the effect of inflation (solving the horizon problem) [25, 22],

describe the CMB dipole anisotropy [87], and demonstrate how inhomogeneities can reproduce the effect of SNIa redshift dimming without the requirement of dark energy [21].

The bang-time models are based on the class of parabolic LTB models, where the metric becomes

$$ds^2 = -dt^2 + [R'(t, r)]^2 dr^2 + R^2(t, r)\{d\theta^2 + \sin^2 \theta d\varphi^2\}. \quad (2.42)$$

The solution is then simplified by setting,  $M(r) = M_0 r^3$  as a coordinate condition where  $M_0$  is a constant which for illustrative purposes is set to  $2/9$ . Equation (2.39) then reduce to

$$R(t, r) = r(t - t_B(r))^{2/3} \quad (2.43)$$

with

$$R'(t, r) = \frac{t - t_B(r) - 2/3 r t'_B(r)}{(t - t_B(r))^{1/3}} \quad (2.44)$$

and (2.36) can be simplified to

$$\rho(t, r) = \frac{1}{2\pi(t - t_B(r))(3t - 3t_B(r) - 2rt'_B(r))}. \quad (2.45)$$

By selecting  $t_B(r) = 0$ , equation (2.45) becomes the Einstein-de Sitter model (see Section 2.2.3). If  $t_B(r) \neq 0$  and  $t_{B,r}(r) = 0$ , the time of the initial singularity is adjusted and the age of the Universe changes. For non-constant functions, the initial singularity becomes a non-simultaneous singular surface, which depends on  $r$ . Thus, a variety of models can be generated for testing the code on parabolic spatial sections.

### 2.2.3 The cosmological PNC

Before proceeding to a discussion on observational models, a brief overview of some of the properties of the PNC of an expanding universe, using CS coordinates, is presented in this section. The PNC is the past directed region causally connected to a cosmological observer and its shape determines the paths that radiation follows to reach the observer. What follows can be considered as a more formal explanation of the PNC illustrated in Figures 1.1 and 2.1. A more detailed description can be found in [37].

For this purpose, the Einstein-de Sitter (EdS) model provides a useful mechanism to conceptualise an expanding universe. This is the simplest solution of the FLRW models, the case where  $k = 0$  and  $\Lambda = 0$  and for the purposes of the discussion, geometrised units with time scaled such that  $t_0 = 1$  is used. Solving equations (2.18) and (2.20) gives

$$a(t) = t^{2/3} \quad \text{and} \quad \rho = \frac{1}{6\pi t^2} \quad (2.46)$$

and when substituting  $a(t)$  into the metric it follows that

$$ds^2 = -dt^2 + t^{4/3} dr^2 + t^{4/3} r^2 \{d\theta^2 + \sin^2 \theta d\varphi^2\}. \quad (2.47)$$

To determine the surface of the the PNC, a null trace can be calculated from the observer position by setting  $ds = d\theta = d\varphi = 0$ . The null ray, in a spherically symmetric universe, traces out the PNC when rotated. Applied to (2.47) it follows that

$$ds^2 = 0 \Rightarrow \int_{r_e}^{r_0} dr = \int_{t_1}^{t_0} \frac{dt}{t^{2/3}}. \quad (2.48)$$

This relation determines the shape of a PNC in a homogeneous expanding universe with a flat spatial section. If we consider a signal emitted from a source at a time,  $t_e$ , in the past, this will be observed at a redshift

$$1 + z = \frac{a(t_0)}{a(t_e)} = t_e^{-2/3}. \quad (2.49)$$

The proper distance  $r_D$  of a locus on the PNC follows by a redshift scaling of the coordinate distance from (2.48) for a signal emitted at time  $t_e$  with  $r_0 = 0$  i.e.

$$r_D = \frac{1}{(1+z)} \int_{r_e}^{r_0} dr \Rightarrow r_D = 3(t_e^{2/3}t_0^{1/3} - t_e). \quad (2.50)$$

This distance corresponds to the proper angular diameter distance ( $r_D = d_D$ ), discussed in Section 2.3.1. This result becomes a point of interest in observational models since (2.50) is not monotonically increasing and setting  $d/dt(r_D) = 0$  shows that  $d_D$  reaches a maximum at some time in the past, which is referred to as the *apparent horizon* (AH)

$$d_{D(AH)} = \frac{4}{9}t_0 \text{ at } t_{e(AH)} = \frac{8}{27}t_0. \quad (2.51)$$

In terms of redshift, this is also the case (see Figure 2.2) and the maximum is reached at  $z = 1.25$  when (2.51) is substituted into (2.49). Since the proper distance starts to decrease from this point onwards, angular sizes will be perceived to increase with redshift. The observable universe is, therefore, by itself, a gravitational lens and angular sizes of remote galaxies are not necessarily an indication of their radial distance without taking the redshift into account.

Conceptually, signals received by an observer will travel on the surface of the PNC but since the Universe was smaller in the past, the PNC reconverges into the initial singularity. Therefore, while an expanding homogeneous Universe evenly enlarges in all direction, the observable universe forms an expanding teardrop. Figure 2.3 shows this result and also includes the path of the oldest signal connected to the PNC; the particle horizon, following from

$$h(t_0) = a(t_0) \int_0^{t_0} \frac{cdt}{a(t)} \quad (2.52)$$

when incorporating  $c$ . It is interesting to note that the oldest signal is currently a distance of  $3ct_0$  from the observer for the EdS model.

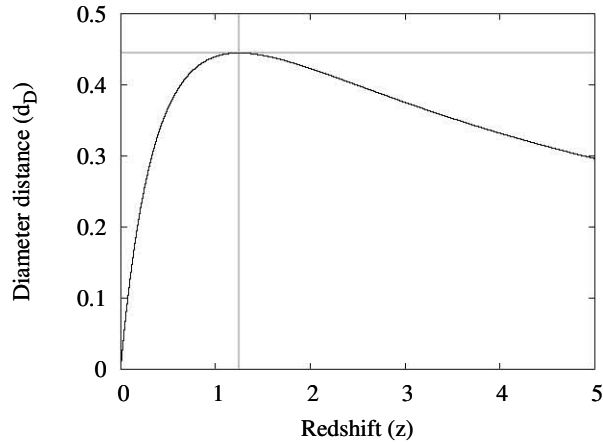


Figure 2.2: The diameter distance ( $d_D$ ) against redshift ( $z$ ) of the Einstein-de Sitter model

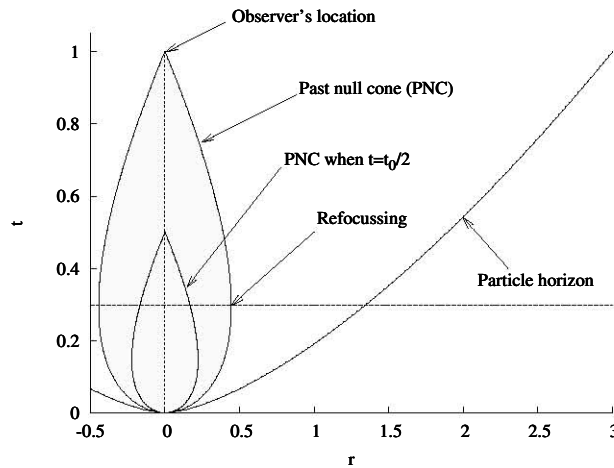


Figure 2.3: Past null cone of the Einstein-de Sitter model

## 2.3 Observational models

The work by Kristian & Sachs [56] is generally considered as the seminal work in direct observational cosmology. Besides the results they obtained, which placed some fundamental limits on observable quantities, their methodology is of general interest (the significance of their work is described in [32]). In summary, they assumed the Universe is describable using Riemannian geometry and then derived observable quantities from the properties of geometric optics and radiation without assuming a theory of gravity. These results were then used in cosmological models to evaluate how observations restrict relativistic cosmology. This paradigm was followed by the developments of Ellis and collaborators [36] as well as Dautcourt [31, 30] in the 1980s. This section will follow the pattern of Kristian & Sachs as a guideline by introducing observable quantities and pointing out what their dependence on a theory of gravity and also on specific cosmological models are. Then a summary of two observational models where these quantities

serve as the initial conditions will follow. In addition, since the resolution of current observations is not sufficient to practically implement the method, some comments will be made on the status and challenges of obtaining the required observational quantities. The observational quantities considered here are those required as the input to spherical symmetric models i.e.: redshift, redshift-drift, distance measures and number counts. In [36], more general models are considered, which can be referred to for further details.

### 2.3.1 Observable quantities

Following [36], *observational quantities*, or direct observations, are observations on the PNC which do not require the assumption of a specific cosmological model for interpretation as cosmological data. Interpretation of observations on cosmological scales is practically a very ambitious task and therefore, quantities considered to be direct observations follow this definition under idealised circumstances. For instance, using number counts from discrete sources are considered to be a direct observation even though current developments make use of assumed models to develop the understanding of number density through luminosity functions. It is the eventual goal that the understanding of number densities will be sufficient to interpret number counts without assumptions dictating a specific cosmology (see [52]). From a mathematical point of view, direct observations can be used as initial conditions on the current PNC to calculate a reversed initial value problem to determine the historical evolution of the Universe.

Observational models, attempt to reconstruct the geometry of the Universe using only direct observations. Parameterized models, on the other hand, makes use of observations in the context of an assumed model. For instance, assuming a RW geometry, the redshift-magnitude dimming represents a cosmological constant. Observations that require such heuristic interpretation, usually within the framework of an assumed model, are referred to as *indirect observations* because under different assumptions, their interpretation could have been different. Although it might be considered unlikely that certain observations can be the result of anything other than their assumed interpretations, a level of circularity is unavoidable because assumptions are not independent of conclusions. From a theoretical point of view indirect observations can be used as constraints to validate the physical consistency of a particular cosmological model.

### Geometric optics

The geometry of null geodesics in curved spacetime is an essential aspect when interpreting observations. This follows from the geometric optics approximation which states that observations received by electromagnetic radiation can be represented by a solution of Maxwell's equations in a charge and current free region [39, 28, 35]. Accordingly, the paths of photons are represented as null geodesics in curved spacetime. This is a well accepted principle in relativity, however, the point made here is that the fact that photons travel on null geodesics, can be derived from the properties of radiation (Maxwell's equations) without assuming a specific theory of gravity. As a consequence, the properties of observations derived from the geometric optics approximation are independent of a theory of gravity.

Following the geometric optics approximation, the ray 4-vector ( $k^\mu = dx^\mu/dv$ ), tangent to photon paths, satisfies equation (2.8) and is therefore an affinely parameterized null geodesic. The affine parameter on a null geodesic is not a directly observable quantity but plays an

important role in interpreting both distance and time in curved spacetime. Since any two affine parameters are linearly related, the affine parameter can be scaled to investigate different physical properties. Moreover, the fundamental 4-velocity ( $u^a$ ) can be combined with the ray 4-vector to represent the wave frequency ( $-u_a k^a = \nu$ ). This combined with the affine parameter can also be used to represent small intervals in space and time

$$|\delta t| = |\delta l| = -(u^a k_a) dv, \quad (2.53)$$

which can be used to evaluate differential radial distances, times, volumes etc. In the developments in Chapter 3, the affine parameter will be used as a radial coordinate to extend the Bondi-Sachs model beyond the AH.

### Redshift

The redshift or blueshift of a wave is the tendency of wavelengths to appear longer or shorter, as a result of the movement or environment of a radiating source relative to an observer. In astronomical observations, the shift of wavelengths is observed as a shift of absorption lines compared to those detected in laboratory experiments<sup>4</sup>. The redshift ( $z$ ) in terms of wavelength ( $\lambda$ ) is defined as (e.g. see [72])

$$z := \frac{\lambda_o - \lambda_e}{\lambda_e} \Rightarrow z + 1 = \frac{\lambda_o}{\lambda_e} \quad (2.54)$$

where  $\lambda_e$  is the wavelength measured at the emitter and  $\lambda_o$  the wavelength at the observer. Therefore, essentially a comparison of the emitted wavelength to the wavelength measured by an observer. In terms of the inverse of the wavelength ( $\lambda = c/\nu$ ), the redshift can also be expressed as the fractional shift in the frequencies

$$z + 1 = \frac{\nu_e}{\nu_o} = \frac{\delta t_o}{\delta t_e}, \quad (2.55)$$

which also reveals the redshift as a time dilation effect when incorporating (2.53). These definitions do not impose any cosmological ideas on the detection of shifting effects, they are derived on the basis that physical consistency is expected between well established laboratory results and astrophysical observations.

Incorporating our understanding of cosmology, the observed redshift is the combined effect of three known mechanisms for the shifting wavelengths: the local Doppler effect ( $z_D$ ) of the specific movement of an object, the shifting of wavelengths due to gravitational effects ( $z_G$ ) and the shifting due to the expansion of the Universe. The later is known as the *cosmological redshift* ( $z_C$ ) due the fact that the expansion of the Universe causes a lengthening of wavelengths, which is towards the red spectrum for visible radiation. The combined effect is a multiplication of the respective redshift terms (see [35] p. 158)

$$(1 + z_{tot}) = (1 + z_C)(1 + z_D)(1 + z_G)(1 + z_oD)(1 + z_oG). \quad (2.56)$$

---

<sup>4</sup>Redshifts are also measured using photometric techniques but these rely on understanding of the characteristics of specific objects. Although these techniques are more practical for large-scale surveys, measuring the shift in emission lines are more reliable [14].

It is expected that local effects at the emitter will be cancelled out by averaging and the observer Doppler effect can be compensated for by taking the CMB anisotropy into consideration. Effectively, the observed redshift then becomes a measure of the expansion of the Universe.

Using the geometric optics approximation and observational coordinates (see Section 2.3.3), the product of the fundamental 4-velocity ( $u^a$ ) and ray 4-vector ( $k_a$ ),  $u^a k_a$  can be adjusted to correspond to the wave frequency by rescaling the affine parameter ( $-u_a k^a = \nu$ , see [35]), which applied to (2.55) gives

$$1 + z = \frac{(u_a k^a)_e}{(u_b k^b)_o} \quad (2.57)$$

as the cosmological redshift. When using coordinates aligned with the PNC, such as observer coordinates,  $(u_b k^b)_o = 1$ , which the redshift is a direct measurement of the zeroth component of the emitter 4-velocity, i.e. [36]

$$1 + z = (u^0)_e. \quad (2.58)$$

This relation provides an initial value of the velocity on the observer PNC, which will be used in the current developments to solve a reversed CIVP.

### Redshift drift

The *redshift drift* ( $\dot{z}$ ) or in the context of (2.55), the *time drift*, is the rate of change of  $z$  over time. Measuring the redshift drift is one of the design objectives of the CODEX spectrograph planned for the European Extremely Large Telescope (E-ELT) [75]. For this, redshift-distance relations will be measured over a number of years to detect variations in redshift with time. Another approach is to make use of cosmic chronometers where similar sources (e.g. massive elliptical red galaxies) at different redshifts are compared to indicate how the expansion of the Universe has progressed through different epochs. A recent study on cosmic chronometers is presented in [70] under the assumption of a homogeneous universe.

In [79, 102, 67, 24], the redshift-drift was investigated as a mechanism for validation of inhomogeneous models. It was pointed out that for certain classes of models, the sign of the redshift drift will be positive up to certain redshifts while for the  $\Lambda$ CDM model, it is expected to be negative. Since initial measurements of  $\dot{z}$  will probably not be a detailed map but might indicate the sign of the value, it will be a clear indication that some models can be ruled out as representing the Universe.

In [86, 66] the concept of redshift-drift was introduced and it was shown that for FLRW models as

$$\frac{dz}{dt} = (1 + z)H_0 + H(z). \quad (2.59)$$

In [96] the redshift-drift was proposed as a method to test the Copernican principle. This was done using spherically symmetric observer coordinates  $\{w, y, \theta, \varphi\}$  where  $w$  is the proper time,  $y$ , the radial distance along the PNC and  $\theta, \varphi$  the same as in spherical polar coordinates. In

this framework the following expression was derived

$$\frac{dz}{dw} = (1+z)H_0 - H(w_0, y) + \frac{1}{\sqrt{3}}\sigma(w_0, y) \quad (2.60)$$

where  $w_0$  is the time at the observer and  $\sigma(w_0, y)$  the shear of image distortion. These coordinates will be discussed in Section 2.3.3.

From the above relations, it is apparent that  $\dot{z}$  is related to the Hubble rate ( $H$ ).  $H$  and  $z$  is also closely related to the affine parameter  $v$ , it is therefore also evident that  $\dot{z}$  should be related to  $v$ . In [35], this relation is pointed out at the observer positions as

$$\left. \frac{dz}{dv} \right|_{v=0} = H^{obs}, \quad (2.61)$$

using null cone based coordinates, and in [82], it was derived for the EdS model that

$$\frac{dv}{dz} = \frac{1}{H_0(1+z)^{7/2}}. \quad (2.62)$$

Determining  $dz/dv$  or  $dv/dz$  is however fundamentally restricted without the assumption of a theory of gravity as will be discussed in Section 2.3.3, Theorem 5.

A more general relation between  $v$  and  $\dot{z}$  will be a significant advantage for the affine CIVP model presented in Chapter 3 but will be investigated in future research. In Chapter 3, the redshift-drift will be used as a direct observation of the cosmological constant.

## Distance

The distance between a source and observer on cosmological scales is a particularly difficult measure since it requires knowledge of the type of source as it was in the past and also the path that light has travelled from the source to the observer in curved spacetime. In order to relate distant objects in the younger Universe to similar nearby objects in the older Universe, the standardisation of intrinsic properties of astrophysical objects through their brightness and size provides standard candles and rulers.

Measuring radiative flux of a discrete object and considering the geometric optics approximation, two measures of distance can independently be obtained from direct observations. Both these measurements, however, required knowledge of the intrinsic properties of the object being observed.

The *luminosity distance* ( $d_L$ ) is defined as

$$d_L := \sqrt{\frac{L}{4\pi F}} \quad (2.63)$$

where  $L$  is the absolute luminosity and  $F$  the measured radiative flux. In terms of the distance modulus ( $\mu$ ) it can be written as

$$\mu := m - M = 5(\log_{10}(d_L) - 1), \quad d_L = 10^{(\mu/5+1)} \text{ [parsec]} \quad (2.64)$$

with  $m$  and  $M$  the apparent and absolute magnitudes. A more general formula is given in

[56]. The benefit of working with magnitudes is that the  $d_L$  can be obtained from single source observations such as type Ia supernovae.

The definition of the *area distance* or *angular diameter distance* ( $d_D$ ) is

$$(d_D)^2 := \frac{dS}{d\Omega} \quad (2.65)$$

with  $dS$  the intrinsic (actual) surface area of the object and  $d\Omega$  the solid angle it subtends at the observer (see Figure 2.4). Observations of  $d_D$  are based on complex sources such as galaxies. This is in general more difficult to interpret than single sources, however, the acoustic peaks on the CMB can be taken as very accurate  $d_D$  measures on the last scattering surface. It is common for  $d_D$  to appear directly in cosmological models as a metric coefficient or coordinate.  $d_D$  is however not a monotonic increasing distance when the PNC refocusses (see Section 2.2.3), which is the motivation in Chapter 3 for adapting the Bondi-Sachs CIVP to have an affine parameter as the radial coordinate instead of the diameter distance.

A useful property of these two measures is that they can be measured independently but also through geometric optics relations,  $d_L$  can be expressed as a redshift product of  $d_D$ . This property is known as the reciprocity theorem (see [41, 39])

$$d_L = (1 + z)^2 d_D. \quad (2.66)$$

$d_D$  can thereby be determined from magnitudes using (2.64) and (2.66). Independent measures of  $d_L$  and  $d_D$  are important since (2.66) is model independent and can be used to verify the validity of proposed models. For instance, by comparing SNIa redshift observations of  $d_L$  and  $d_D$  with calculations using (2.66), the axion-photon mixing effect was discarded as an alternative explanation to cosmic acceleration [8].

## Density distribution

The classical test to determine the mass distribution in the Universe is to count the number of discrete sources emitting radiation at their redshifts. Such observations have been in operation since the 1930s. However, they are still the most difficult to interpret as model independent measures in cosmology. Nevertheless, the principle behind number counts is relatively simple and comes down to counting the number of galaxies in a given volume and then through the understanding of how these sources contribute to the density, the density distribution of a region can be determined.

A model independent formula for cosmological number counts was derived in [39]. With reference to Figure 2.4, the number of galaxies in a proper volume  $dV$ , formed by a differential displacement  $\delta l$  of a surface  $dS$  is counted.  $dS$  is connected to the observer ( $O$ ) by null geodesics intersecting at  $O$  and subtended by the solid angle  $d\Omega_0$ . The *proper number density*  $n$  is then defined as

$$n := \frac{dN}{dV} \Rightarrow dN = n \delta l dS. \quad (2.67)$$

With  $\delta l = (u^a k_a) dv$  from (2.53), where the sign is changed to represent the PNC, (2.67) becomes

$$dN = (d_D)^2 d\Omega_0 [n(-k^a u_a)]_A dv. \quad (2.68)$$

with  $u^a$  the 4-velocity,  $k^a$  the tangent vector along the null geodesics and  $v$  the affine parameter distance along null geodesics. This is in terms of the number counts and the proper volume at the emitter (marked as A in Figure 2.4). In terms of the observer rest frame at the vertex  $O$ ,  $k^a u_a = 1$ . Substituting this into (2.57), (2.68) can be written as

$$dN = (d_D)^2 d\Omega_0 n(1+z) dv. \quad (2.69)$$

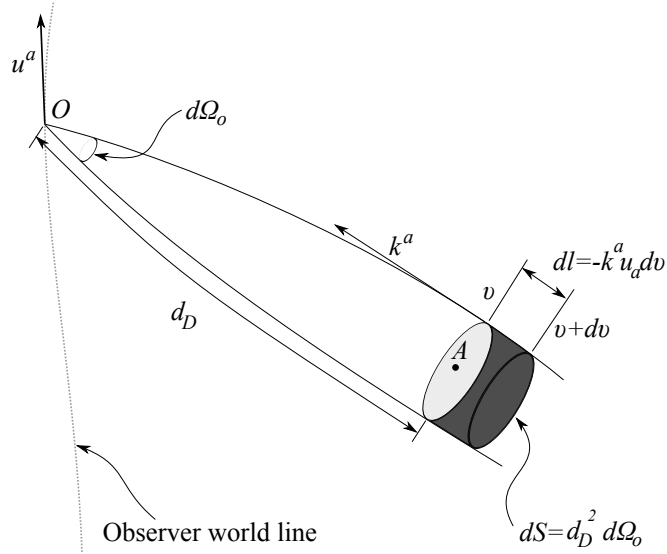


Figure 2.4: Cosmological number counts  $N$ .

Equation (2.69) is set in idealised circumstances where all galaxies are being counted. This is not practically possible and there has to be some probabilistic provision for galaxies not counted. To incorporate counting uncertainties, a completeness parameter  $J$  is included in equation (2.69), which has to make provision for selection problems without the a priori assumption of a specific cosmology

$$dN = Jn(d_D)^2 d\Omega_0(1+z)dv. \quad (2.70)$$

Having number counts on different scales, it then has to be derived how this represents the mass-energy density of the Universe. To this effect, a mass per galaxy function is introduced ( $\mathcal{M}_g$ ). However, this is not a direct conversion since galaxies are complex objects and their age, environment, interaction and morphology affects how different galaxies in different epochs can be compared and contribute to density. In addition, the presence of observable objects also has to be used to extrapolate the presence of dark matter. A simple conversion follows as

$$\rho(v) = n(v)\mathcal{M}_g \quad (2.71)$$

although it is recognised that the process of obtaining  $\mathcal{M}_g$  is practically very challenging especially without making cosmological assumptions.

In practice,  $N$  will be measured in terms of  $z$  since  $v$  is not directly observable. This requires knowledge of a relation between  $v$  and  $z$ , which cannot be determined from geometric optics only; a theory of gravity has to be assumed. This is in fact a crucial point which formally limits the applicability of cosmography from ideal observations [36]. With a one-to-one (up to some point) relation between  $v$  and  $z$ , (2.70) can then be written as

$$\rho(z) = \frac{\mathcal{M}_g}{(1+z)J(d_D)^2 d\Omega_0} \left( \frac{dN}{dz} \frac{dz}{dv} \right). \quad (2.72)$$

Studies towards the understanding of these aspects are currently in process but still under the assumption of specific cosmological models (see [82, 1, 52]). Recent developments in [52] using the FORS survey on high redshifts ( $0.5 \leq z \leq 5.0$  for blue bands and  $0.75 \leq z \leq 3.0$  for the red bands) are the latest advances towards the cosmological interpretation of galaxy number counts as a measure of density. Although these are still based on the assumption of a FLRW model, it is envisaged that further work will be done where radial homogeneity will be relaxed in the near future.

### 2.3.2 The LTB observer approach

#### The model

This approach is based on the LTB model transformed to align with the PNC and written in terms of observable quantities. The formalism described in this section is based on a series of papers where this method was developed up to the point where numerical algorithms were used for calculations using input data that represents realistic observations. In [71], the model was initially presented and by proving two theorems (see Theorems 2 and 3), it was shown that source evolution and radial inhomogeneities are intrinsically ambiguous. This is a fundamental observational limitation, which is employed by others to mimic dark energy using LTB models (e.g. [23]). In [51, 63] a numerical code was developed to solve general cases, with  $\Lambda = 0$  and the behaviour of these calculations were tested using realistic observational data. An important relation between the active gravitational mass  $M$ , diameter distance  $R$  and the cosmological constant  $\Lambda$  was derived in [49]. The highlight of these developments will now follow in this section.

For direct reference, the LTB metric, Friedman and density equations are rewritten here, using geometric units

$$ds^2 = -dt^2 + \frac{[R'(t,r)]^2}{1+2E(r)} dr^2 + R^2(t,r) \{d\theta^2 + \sin^2 \theta d\varphi^2\}, \quad (2.73)$$

$$\dot{R}(t,r) = \pm \sqrt{\frac{2M(r)}{R(t,r)} + 2E(r) + \frac{\Lambda R^2(t,r)}{3}} \quad (2.74)$$

$$4\pi\rho(t,r) = \frac{M'(r)}{R^2(t,r)R'(t,r)}. \quad (2.75)$$

As pointed out in Section 2.2.2, the LTB model is fully determined by the three arbitrary functions:  $M(r)$ ,  $E(r)$  and  $t_B(r)$ . However, only two of them have to be solved while the other can be fixed by a gauge choice.

Following an observational approach, these will have to be determined from observations on the local PNC. However, CS coordinates are not causally aligned with observations and a transformation is required to project the metric onto the PNC. This alignment is done by considering a radial null geodesic in spherical symmetry ( $ds^2 = 0 = d\theta^2 = d\varphi^2$ ), which when introduced into (2.73) gives

$$d\hat{t} = -\frac{\widehat{R}'}{\sqrt{1+2E}}dr. \quad (2.76)$$

In this equation, the ‘ $\hat{\cdot}$ ’ refers to expressions where  $t$  is written in terms of  $r$  i.e.  $\hat{t} = t(r)$ . The righthand side of the equation is completely in terms of  $r$  and can be integrated, if  $t(r)$  is known. This is facilitated by rescaling  $r$  such that  $d\hat{r}/d\hat{t} = 1$  and taking the current time at position  $r = 0$  as  $t_0$ . Then

$$\frac{\widehat{R}'}{\sqrt{1+2E}} = 1 \quad \text{and} \quad \hat{t}(r) = t_0 - r \quad (2.77)$$

for an incoming null geodesic. The important aspect, here, is that on the null cone, all quantities required for the LTB model can be written in terms of  $r$  alone. The Friedman equation and density equations on the PNC are then written as <sup>5</sup>:

$$\widehat{R} = \sqrt{\frac{2M}{\widehat{R}} + 2E + \frac{\Lambda\widehat{R}^2}{3}} \quad (2.78)$$

$$4\pi\hat{\rho}\widehat{R}^2 = \frac{M'}{\sqrt{1+2E}} \quad (2.79)$$

### Observable quantities

Redshift distance observations can directly be related to the model since the areal radius ( $\widehat{R}$ ) on the null cone, is the angular diameter distance ( $d_D$ ) and using equations (2.63) and (2.66), related to the luminosity distance ( $d_L$ ), magnitudes and luminosities e.g.:

$$\widehat{R}(z) = \frac{d_L}{(1+z)^2}. \quad (2.80)$$

For the density distribution from number counts, a volume element is considered for a small radial increment

$$d\widehat{V}^3 = 4\pi\widehat{R}^2 \frac{\widehat{R}'}{\sqrt{1+2E}}dr. \quad (2.81)$$

The differential mass in terms of the mean mass per source ( $\hat{\mu}$ ), the number density of sources

---

<sup>5</sup>The plus sign is taken for the square root since it represents the PNC.

$(n(z))$  and a small increment in redshift ( $\delta z$ ) is

$$4\pi\hat{\mu}n\delta z = \hat{\rho}\widehat{dV^3}. \quad (2.82)$$

Combining these with equation (2.77) then gives an equation for the mass in a volume element in terms of  $z$  as

$$\hat{R}^2\hat{\rho} = \hat{\mu}n\frac{dz}{dr}. \quad (2.83)$$

A relation derived in [49] provides an expression for the cosmological constant  $\Lambda$ , with some restrictions, in terms of the values of the diameter distance and the active gravitational mass at the AH as

$$\Lambda\hat{R}_m^3 - 3\hat{R}_m + 6M_m = 0, \quad (2.84)$$

where the  $m$  subscript refers to the values corresponding to the maximum value of  $\hat{R}$ . This is particularly interesting since having values for  $\hat{R}$  and  $M$ ,  $\Lambda$  can be determined without additional observations. It also provides a method for testing current estimations of  $\Lambda$ , provided that precise enough observations are available to determine  $R$  and  $M$  at the AH.

### Observational model

Since  $r$  is not a measurable quantity, in order to relate (2.79) to observations, the redshift ( $z$ ) is introduced as a radial coordinate. Writing the Friedman equation (2.78) (with  $\Lambda = 0$ ) in terms of  $z$  and some rearrangement an equation relating  $r$  and  $z$  is obtained as

$$\frac{d\hat{R}}{dz}\frac{d^2z}{dr^2}(1+z) + \left[\frac{d^2\hat{R}}{dz^2}(1+z) + \frac{d\hat{R}}{dz}\right]\left(\frac{dz}{dr}\right)^2 = -4\pi\hat{\rho}\hat{R}(1+z). \quad (2.85)$$

This equation is the Raychaudhuri equation on the null cone in terms of  $z$ . It is important to note that this equations is only in terms of radial derivatives compared to (2.33), which is in terms of time derivatives. This is an example of the duality of space and time on the PNC. By further manipulation and incorporating the observable quantities, the following set of ODEs, which can be solved numerically is obtained:

$$\frac{d^2r}{dz^2} = \left\{ \frac{1}{1+z} + \frac{d^2\hat{R}/dz^2 + 4\pi\hat{\mu}n(dr/dz)/\hat{R}}{d\hat{R}/dz} \right\} \frac{dr}{dz} \quad (2.86)$$

$$\sqrt{1+2E} = \frac{d\hat{R}/dz}{2(dr/dz)} + \frac{(1-2M/\hat{R})(dr/dz)}{2d\hat{R}/dz} \quad (2.87)$$

$$\frac{dM}{dz} = 4\pi\hat{\mu}n\sqrt{1+2E}. \quad (2.88)$$

From these equations,  $r(z)$ ,  $M(z)$  and  $E(z)$  can be calculated and then using the exact solutions of the LTB model,  $t_B(z)$ . It should be noted that in order to determine  $\Lambda$  from (2.84),  $M(z)$  has to be known, but,  $M$  is implicitly related to  $\Lambda$  in the other relations. Therefore, (2.84), will have to make use of an iterative scheme when solving the observational model. Having the values for  $r(z)$ ,  $M(z)$ ,  $E(z)$  and  $\Lambda$ , the state of the Universe at any time can be determined,

regardless if it is within the observer PNC, i.e. causally connected to the observer.

In their numerical calculations, [51] and [63] made use of binning techniques for discrete data, representing realistic observations, as input values. Also, provision had to be made for  $\hat{R}$  being zero at the origin and  $d\hat{R}/dz$  being zero at the AH, which cause singularities in the observable model's equations. These were treated using series solutions around these regions. The model presented in Chapter 3 has similar limitations around these regions and series solutions also provides a method for integrating through the singularities.

### Fundamental limitations

In [71] a formal investigation into the ability to distinguish inhomogeneities from source evolution in isotropic observations was done. The formulation that will be used here is taken from [38] with the notation adapted to the current context. This relates number counts ( $n(z)$ ) and the apparent luminosity ( $l(z)$ ) with their evolution functions, the mass per source ( $M(z)$ ) and the absolute bolometric luminosity ( $L(z)$ ). In [71], it was formally proved that <sup>6</sup>:

**Theorem 2 (Isotropic Observations Theorem 1)** *Any given isotropic set of source observations  $l(z)$  and  $n(z)$ , together with any given source luminosity and mass evolution functions  $L(z)$  and  $M(z)$ , can be fitted by a spherically symmetric dust cosmology – a LTB model – in which observations are spherically symmetric about us because we are located near the central world line.*

The converse followed as:

**Theorem 3 (Isotropic Observations Theorem 2)** *Given any spherically symmetric geometry and any spherically symmetric set of observations, we can find evolution functions that will make the model compatible with the observations. This applies in particular if we want to fit observations to a FLRW model.*

These theorems place fundamental limits on the ability to interpret isotropic observations. Effectively, any observational scenario can be interpreted as either inhomogeneous or homogeneous with some source evolution function. Since source evolution requires the prior assumption of a cosmological model, using isotropic observations to distinguish between homogeneous and inhomogeneous models is fundamentally obscured.

Even though these results were derived without using a cosmological constant, they provide the formal foundation for investigations where the interpretation of redshift-dimming is taken to be inhomogeneities instead of dark energy.

### 2.3.3 The observer coordinate approach

#### The model

Instead of transforming spherical coordinates to align with observations, a coordinate system can be chosen to be aligned with the causal structure connected to the observer. Effectively,

---

<sup>6</sup>This theorem is related to an earlier result in [61], which in turn cited [59] as the primary reference. The emphasis in the formulation, here, is on source evolution functions, while in [61], it was shown that the assumption of isotropic observations imposes isotropy on the geometry of the EFEs.

these coordinates trace out the observer's PNC and are naturally aligned with the propagation of EMR. This is an idea proposed by Temple in 1938 [94] but, as a cosmological formalism, developments only started in the 1980s with the *Observational Cosmology* (OC) programme of Ellis and others and separate work of Dautcourt [31, 30]. The OC programme published a series of papers and is still active through the work of Stoeger and others [36, 91, 89, 92, 93, 90, 60, 88, 3, 4, 5, 6, 7]. In these, the fluid-ray tetrad approach was developed, which is particularly favourable for exact solutions of the model <sup>7</sup>. Separate developments towards a numerical solution, using a coordinate approach, were done in [50] where many of the results of the tetrad approach were reproduced <sup>8</sup>. Parallel to the theoretical work, research is also in progress where galaxy survey data is prepared for observable quantities closely related to the requirements of these model [82, 1, 52]. The discussion in this section is mostly based on [7], which is a detailed summary of the latest developments of this approach. Some of the notation was adapted to be in line with other sections in this text.

A general null cone metric in spherical symmetry, with reference to Figure 2.5, is written as

$$ds^2 = -A^2(w, y)dw^2 + 2A(w, y)B(w, y)dw dy + C^2(w, y)\{d\theta^2 + \sin^2\theta d\varphi^2\}. \quad (2.89)$$

The coordinates  $x^\mu = \{w, y, \theta, \varphi\}$  are defined as (see [7]):  $w$ , the proper time coordinate on an observer's world line ( $\mathcal{C}$ ), which is a time-like geodesic. Hypersurfaces with  $w = \text{constant}$  are PNCs and the PNC of an observer at the current time is indicated as  $w_0$ .  $y$  represents a general radial parameter increasing along a PNC with  $y = 0$  the position at the cone vertex.  $\theta$  and  $\varphi$  are the latitude and longitude angles, respectively, and remain constant on light rays.

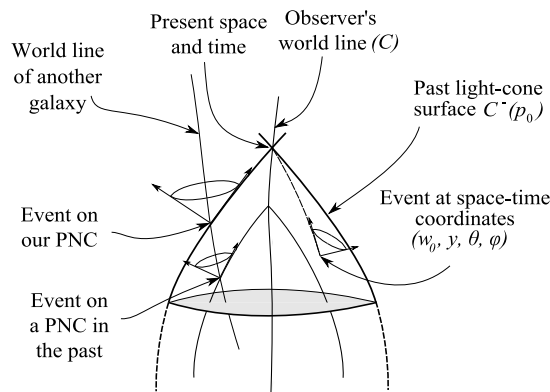


Figure 2.5: Observational coordinates (based on Figure 1 in [36])

Some constraints are required to make the model more specific and also to simplify the solution. The metric as defined in equation (2.89) is that of a general PNC and in order to restrict the model to the PNC of a local observer,  $w$  can be scaled such that  $\mathcal{C}$  represents the observer's world line, which is done by specifying  $A(w_0, 0) = 1$ . The properties of the 4-velocity

<sup>7</sup>The fluid-ray tetrad approach is discussed in more detail on page 40.

<sup>8</sup>A very useful comparison of differences in notation of the OC programme and related research is given in [50].

in this setting are

$$u^\mu = \frac{1}{A}\delta_w^\mu, \quad u_\mu = (-A, B, 0, 0), \quad u^a u_a = -1 \quad (2.90)$$

and that of the null ray 4-vector [50]

$$k_\mu = \delta_\mu^w, \quad k^\mu = \frac{dx^\mu}{dv} = \left(0, \frac{1}{AB}, 0, 0\right), \quad k^a k_a = 0. \quad (2.91)$$

For later reference, it is worth noting that if the affine parameter is used as radial coordinate ( $y = v$ ), then,  $AB = 1$ . There are some freedom in the selection of  $y$ , as required, it can be implemented as a specific measure of distance e.g. the redshift ( $z$ ), an affine parameter ( $v$ ), the diameter distance ( $d_D$ ) or alternatively as a coordinate comoving with the fluid flow ( $u^\mu \partial_\mu y = 0$ ) [36]. It is usually chosen as an observable distance, such as  $z$  or  $d_D$ , to determine the initial PNC and then a comoving coordinate to determine spacetime off the PNC. The relationship between the covariant and contravariant forms of  $u^a$  and the normalisation condition (2.14) require as an integration condition that [7]

$$A' = -\dot{B}, \quad (2.92)$$

which also follows from the geodesic equations for  $u^a$  [50]. Additional freedom in the coordinates and the choice of  $y$  being comoving allow for setting <sup>9</sup>

$$A_0(y) = B_0(y). \quad (2.93)$$

Furthermore, to ensure that the behaviour of the model is regular around the cone vertex, the following central conditions are specified for the model:

$$\text{as } y \rightarrow 0 : A(w, y) \rightarrow A(w, 0) \neq 0, \quad (2.94)$$

$$B(w, y) \rightarrow B(w, 0) \neq 0, \quad (2.95)$$

$$C(w, y) \rightarrow B(w, 0) y = 0, \quad (2.96)$$

$$C'(w, y) \rightarrow B(w, 0). \quad (2.97)$$

As with other cosmological models the energy-matter content used in the model is taken as dust. The objective is then to determine the metric coefficients, which is done by deriving the values on the current PNC of  $A_0$ ,  $B_0$ , and  $C_0$  from observations. These are then used as initial values to be evolved off the PNC to obtain  $A(w, y)$ ,  $B(w, y)$  and  $C(w, y)$  in the region causally connected to the observer. The model is therefore only concerned with the region fundamentally observable to the observer, i.e. the observable universe.

---

<sup>9</sup>The quantities in this discussion on the current PNC will be indicated with a subscript 0, i.e.:  $A(w_0, y) := A_0(y)$ .

## Observable quantities

In comoving coordinates, the  $g_{00}$  component of the metric (2.89) is directly related to the redshift ( $z$ ) using (2.58) and (2.90) as

$$1 + z = \frac{dw}{d\tau} = u^0 = \frac{1}{A_0(y)} \quad \text{with } u^0|_{y=0} = 1 \quad (2.98)$$

when  $w$  is scaled such that  $w_0$  is the age of the Universe as observed at the current epoch.

Through redshift magnitude relations, using (2.63), the luminosity distance ( $d_L$ ) can be expressed as a function of  $z$  and then using the reciprocity theorem (see [39]), the diameter distance is

$$C_0(z) = d_D = d_L(1 + z)^2. \quad (2.99)$$

All radial derivatives of  $C_0(z)$  on the initial null cone are also known through this relation.

Galaxy number counts can be used as a measure of mass-energy distribution along the radial coordinate. The form of equation (2.72) in these coordinates for the number of galaxies counted up to a distance  $z$  the mass-energy density (notated here as  $\mu$ ) is

$$\mu_0(y) = \frac{\mathcal{M}_g}{(1 + z)J(C_0)^2 d\Omega_0 A_0 B_0} \left( \frac{dN}{dz} \frac{dz}{dy} \right) = \frac{\mathcal{M}_g}{J(C_0)^2 d\Omega_0 B_0} \left( \frac{dN}{dz} \frac{dz}{dy} \right) \quad (2.100)$$

Analogous to  $M(r)$  in the LTB model, the quantity  $M(y)$ , which is related to the total mass measured by a central observer up to a distance  $y$ , is introduced as

$$M(y) = \frac{1}{8\pi} \int_0^y m N'(y^*) F(y^*) dy^* \quad \text{with } F(y) = \left( \frac{\dot{C}}{A} + \frac{C'}{B} \right). \quad (2.101)$$

When  $C$  is known, an expression of  $M(y)$  from where  $C$  reaches a maximum can be used in

$$6M_{max} + \mu_\Lambda C_{max}^3 - 3C_{max} = 0 \quad (2.102)$$

to determine  $\mu_\Lambda$ , the energy due to  $\Lambda$ . This is the observer coordinate version of equation (2.84) in the LTB model and was independently derived in [4] and [50].

Since observations are measured against  $z$ , the relation between  $y$  and  $z$  is a key property in the model. This can be determined from the Raychaudhuri equation (which will follow later in this section (2.109)) as

$$\frac{dy}{dz} = \frac{1}{A_0} (1 + z)^2 \frac{dr_0}{dz} \left\{ 1 - \frac{1}{2} \int_0^z (1 + z^*) r_0(z^*) M_0(z^*) dz^* \right\}^{-1} \quad (2.103)$$

or alternatively from the redshift drift ( $\dot{z}(z)$ ) using

$$\dot{z}(w_0, y) = (1 + z) \left\{ \frac{\dot{A}_0(0)}{A_0(0)} - \frac{\dot{A}_0(y)}{A_0(y)} \right\}. \quad (2.104)$$

The redshift drift also provides an alternative method to determine  $\mu$ , which is an advantageous

property of this model since some of the uncertainties of number counts can be avoided (see [6, 7]).

### Formalism and model

Initially in [36], the Newman-Penrose (NP) formalism was used to setup the model on the current PNC. Since the values on the initial PNC originate from null geodesics, the null tetrad of the NP formalism was useful for determining the metric coefficients originating from EMR data. The NP formalism is not well adapted to handle matter flow, required to integrate off the PNC, and it was proposed to use the Bondi-Sachs CIVP for matter evolution. The Bondi-Sachs CIVP was, however, not implemented and in subsequent work the fluid-ray (FR) formalism was developed, which was suitable for both determining the geometry of the current PNC and the solution off the PNC [91]. The FR formalism is similar to the NP formalism but where the NP tetrad only consists of null vectors and conjugates of orthogonal surfaces, the FR formalism makes use of the fluid 4-velocity, a time-like vector, in the place of one of the null vectors which makes it suitable to model both radiation and matter flow.

The FR tetrad formalism produces two matter equations

$$\dot{\mu}_m = -2\mu_m \left( \frac{\dot{B}}{2B} + \frac{\dot{C}}{C} \right), \quad (2.105)$$

$$\dot{\omega} = -3\frac{\dot{C}}{C} \left( \omega + \frac{\mu_\Lambda}{6} \right), \quad (2.106)$$

with  $\mu_m$  the relativistic mass-energy of dust with dark matter and  $\omega$  defined as

$$\omega := -\frac{1}{2C^2} + \frac{\dot{C}}{AC} \frac{C'}{BC} + \frac{1}{2} \left( \frac{C'}{BC} \right)^2. \quad (2.107)$$

Also, the following equations with (2.92) for radial derivatives

$$A' = -\dot{B}, \quad (2.108)$$

$$\frac{C''}{C} = \frac{C'}{C} \left\{ \frac{A'}{A} + \frac{B'}{B} \right\} - \frac{1}{2} B^2 \mu_m, \quad (2.109)$$

$$\left[ \left( \omega_0(y) + \frac{\mu_\Lambda}{6} \right) C_0^3 \right]' = -\frac{1}{2} \mu_{m0} B_0 C_0^2 \left( \frac{\dot{C}}{A} + \frac{C'}{B} \right), \quad (2.110)$$

$$\frac{\dot{C}'}{C} = \frac{\dot{B}}{B} \frac{C'}{C} - \left( \omega + \frac{\mu_\Lambda}{2} \right) A B, \quad (2.111)$$

and two separate equations for the time derivatives

$$\frac{\ddot{C}}{C} = \frac{\dot{C}}{C} \frac{\dot{A}}{A} + \left( \omega + \frac{\mu_\Lambda}{2} \right) A^2, \quad (2.112)$$

$$\frac{\ddot{B}}{B} = \frac{\dot{B}}{B} \frac{\dot{A}}{A} - 2\omega A^2 - \frac{1}{2} \mu_m A^2. \quad (2.113)$$

A detailed description of the solution is presented in [6, 7] and only some cursory remarks will be made here. Firstly, as already mentioned, an expression to relate  $z$  and  $y$  is obtained

from (2.109), the Raychaudhuri equation. In this case the Raychaudhuri plays a similar role as it did with the LTB approach. Remembering that  $C_0$  is known and that it was chosen that  $A_0 = B_0$ , the only unknowns on the initial PNC are  $\dot{C}_0$  and either  $A_0$  or  $B_0$ . By solving (2.111) for  $\omega_0$ , an expression is obtained for  $\dot{C}_0$  with  $\mu_\Lambda$  still unknown. This result can be used to find an expression for  $M(y)$  also with  $\mu_\Lambda$  unknown and this can then be used to find  $M$  at  $z_{max}$ . Having  $M(z_{max})$ , (2.102) can be used to find  $\mu_\Lambda$ , which in turn can be used to find  $\dot{C}$ .

From these equations, together with the observable quantities and coordinate conditions, exact solutions can be found for the metric coefficients on the current PNC. Since the solution is exact, time derivatives can be taken of the initial solutions and these can be repeated to obtain higher derivatives. Having as multiple time derivatives, the evolution off the current PNC can be determined using Taylor series expansions. It was demonstrated in [7] that the equations are stable under observational uncertainties and suitable for continuous initial functions derived from observational data.

In [7], a comparison between the OC and the LTB observer approaches was presented and it was pointed out that the PNC based coordinates of the OC approach is in principle more natural since it aligns with the PNC of the observer. Also, the OC approach do not require transformations to observations to the PNC, which introduce difficulties such as the singularity at the maximum diameter distance.

## Fundamental limitations

Observer coordinates is a particularly useful framework to investigate the theoretical limitations of deducing information from observations. The question of decidability in cosmology was investigated in [36] and it was concluded that we have to assume a theory of gravity in order to determine the geometry of the observable universe. The discussion here is based on that in [35] but simplified for spherical symmetry. It is then formalised as:

**Theorem 4 (Limits of cosmography)** *Even with perfect observations, cosmography (no gravitational field equations) cannot determine the spacetime geometry on our PNC.*

The reason for this is that the necessary data for the cosmography problem cannot fully be determined from observations. In the case of spherical symmetry, the limitation is that  $dv/dz$  and  $\rho$  cannot be separated without assuming a theory of gravity. This has been mentioned in discussing redshift-drift and number counts where  $dv/dz$  is required to interpret these quantities. Having established the limits of cosmography, it was further investigated what can be attained assuming a theory of gravity. Assuming General Relativity it then follows that:

**Theorem 5 (EFEs determine the PNC)** *Given the data set  $\{u^\mu, dv/dz, \rho\}$  – based on idealised observations of luminous sources and the assumptions on dark matter and dark energy – (Section 1.1.2 (i), (ii) and (iii)) the EFEs on the PNC (i.e. those equations without derivatives transverse to  $C^-(w_0)$ ), uniquely determine the matter distribution  $(\rho_m, u^\mu)$  and geometry  $(g_{\mu\nu})$  of the observable part of  $C^-(w_0)$ .*

Together these two theorems form the foundation of observational models: we cannot determine the geometry of spacetime from observations alone but assuming General Relativity, it can be

determined uniquely.

## 2.4 Conclusion

The concepts of parameterized and observational models were described in this chapter by providing summaries of the theoretical aspects required for the developments in this thesis. These included, the  $\Lambda$ CDM and *LTB cosmologies*, representative parameterized models, and the *LTB observer* and *observer coordinate* approaches, representative of observational models. With this as background, the requirements of a numerical observational model, which is the core development of this thesis, can now be summarised as:

- i. The model should be based on direct observations. This implies that coordinates should be transformed or aligned with the PNC or coordinates should be used that follow this alignment naturally.
- ii. The model should solve two subproblems. Firstly to determine initial values from direct observations and secondly to evolve the EFEs from the initial values off the current PNC into the past.
- iii. The model should be based on a general geometry (at least more than the FLRW models) and initial values from observable quantities should be the restriction of the geometry.
- iv. The model should include the aspects considered relevant to the  $\Lambda$ CDM model. In particular, even though not directly observable, the cosmological constant ( $\Lambda$ ) and dark matter should be included in the model.
- v. The numerical scheme for solving the model should be stable and convergent.

In the remainder of this thesis, an observable universe model will be developed based on the material described in this chapter. With reference to the list of requirements this will proceed by: (i) adapting Bondi-Sachs null coordinates for cosmology; (ii) setting up this model as a reverse CIPV thereby facilitating calculations into the interior of the PNC initiated from values on an initial PNC, which were derived from observable quantities; (iii) the model is effectively an *LTB* model on null coordinates and therefore more general than the FLRW geometry; and (iv) the model is derived with  $\Lambda$  and also incorporating the assumption regarding  $\Lambda$  and dark matter in Section 1.1. In Chapter 4, a numerical scheme is developed for solving this model and Chapter 5 addresses point (v) by testing the stability and convergence of the model.

Other topics described in this chapter that are of general interest to the developments that follow are:

- According to Theorems 4 and 5, fundamentally, cosmography alone cannot determine the spacetime geometry of the observable universe, but assuming General Relativity, it can be determined uniquely.
- Further, of interest to the application of the code in Chapter 5, according to Theorems 2 and 3, any isotropic observational scenario can be interpreted as either inhomogeneous or homogeneous with some source evolution function. Since source evolution requires

the prior assumption of a cosmological model, using isotropic observations to distinguish between homogeneous and inhomogeneous models is fundamentally obscured.

- A complication that will arise in the developments, follows from Sections 2.2.3 and 2.3.1 where it was shown that the diameter distance ( $d_D$ ), even though it is directly observable, is not unique measure of distance beyond the AH. On the other hand, an affine parameter on a null geodesic is uniquely defined (see Theorem 1) up to significantly larger distances, providing a useful radial coordinate but it is not directly observable.

These three topics will be recurring themes in the rest of the thesis.

## Chapter 3

# Characteristic formalism

The characteristic formalism is the formulation of the Einstein field equations (EFEs) as a characteristic initial value problem (CIVP). The characteristics in relativity are null geodesics, which form the frame of reference for this formalism. The topic of this chapter is the application of the characteristic formalism to study problems in observational cosmology. The basis of this development is recognising that the null geodesic frame of reference of the CIVP corresponds to the causally connected region of a cosmological observer: i.e. when considering the cosmological history, the past null cone (PNC). Initially, the CIVP as derived by Bondi and Sachs, which uses the diameter distance as radial coordinate, is adapted for cosmology. This implementation is, however, limited to the region where the diameter distance is a unique coordinate i.e. prior to the apparent horizon (AH). A new model more suitable for modelling the cosmological PNC is introduced in this chapter. The development of this model is the core of the work of this thesis. The models presented in this chapter are spherically symmetric and thereby avoid some complexities, such as the development and presence of caustics, associated with more general CIVP models. The majority of the work presented in this chapter was published in [97, 98].

### 3.1 Bondi-Sachs CIVP

#### 3.1.1 Mathematical model

The essence of the characteristic formalism in NR is a frame of reference based on outgoing null cones that evolve from values on an initial null cone. The idea is conceptualised in Figure 3.1.  $G$  is a timelike geodesic, and  $u$  is the proper time on  $G$ . (In practice, in NR simulations the inner boundary of the null cone is usually a time-like worldtube rather than a geodesic, see [101] pp. 13–15, but the problem can be formulated with a geodesic). The gauge freedom of  $u$  is limited to its scaling as a specific time parameter. Null geodesics emanating from  $G$  have constant  $(u, \theta, \varphi)$ , and near  $G$  the angular coordinates  $\theta$  and  $\varphi$  have the same meaning as in spherical polar coordinates. The coordinate  $r$  is the diameter, or area, distance defined by the condition that the surface area of a shell of constant  $r$  is  $4\pi r^2$ .<sup>1</sup>

<sup>1</sup>The use of notation here of  $u$  and  $r$  is different from that in Chapter 2.

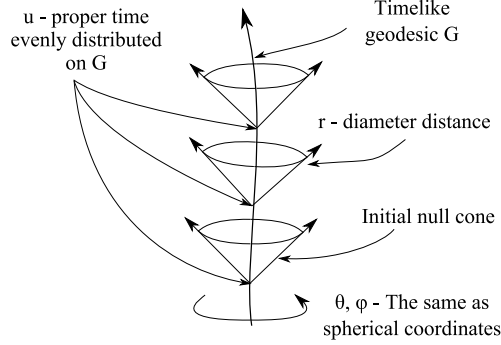


Figure 3.1: Null cone coordinates of the CIVP

A spherically symmetric null cone metric based on the Bondi-Sachs metric is:<sup>2</sup>

$$ds^2 = -e^{2\beta(u,r)} \left( 1 + \frac{W(u,r)}{r} \right) du^2 - 2e^{2\beta(u,r)} dudr + r^2 \{d\theta^2 + \sin^2 \theta d\varphi^2\}. \quad (3.1)$$

This is a generalization of the well-known Eddington-Finkelstein form of the exterior Schwarzschild metric, obtained by setting  $\beta = 0$ ,  $W = -2M$  where  $M$  is the mass of the source. The coordinate system is defined such that  $\beta$  and  $W$  vanish at the vertex of each null cone, i.e. at  $r = 0$  equation (3.1) reduces to a Minkowskian metric.

Substituting (3.1) into the EFEs, using the form  $R_{ab} = \kappa(T_{ab} - \frac{1}{2}Tg_{ab})$ , with the stress-tensor for a dust-like fluid ( $T_{ab} = \rho v_a v_b$  and  $T = -\rho$ )<sup>3</sup>, leads to expressions for  $\beta$  and  $W$

$$\beta_{,r} = \frac{1}{4} \kappa r \rho (v_1)^2 \quad (3.2)$$

$$W_{,r} = e^{2\beta} - 1 - \frac{1}{2} \kappa e^{2\beta} \rho r^2 \quad (3.3)$$

with the initial conditions inherent to the coordinate definition as  $\beta(0) = W(0) = 0$ . Further, substituting the dust stress tensor and (3.1) into the conservation equation,  $\nabla_b T^{ab} = 0$ , it follows that

$$v_{1,u} = \left( 2v_0 - \left( 1 + \frac{W}{r} \right) v_1 \right) \beta_{,r} + \frac{1}{2} v_1 \left( \frac{W_{,r}}{r} - \frac{W}{r^2} \right) + \left( \left( 1 + \frac{W}{r} \right) - \frac{v_0}{v_1} \right) v_{1,r} \quad (3.4)$$

$$\rho_{,u} = \frac{1}{v_1} \left\{ \rho \left[ \left( 1 + \frac{W}{r} \right) \left( \frac{2v_1}{r} + v_{1,r} \right) - \left( \frac{2v_0}{r} + v_{0,r} \right) + \left( \frac{W_{,r}}{r} - \frac{W}{r^2} \right) v_1 \right] + \left( \left( 1 + \frac{W}{r} \right) v_1 - v_0 \right) \rho_{,r} - \rho v_{1,u} \right\} \quad (3.5)$$

An equation for  $v_{0,u}$  is also obtained from this but making use of the normalisation condition (equation 2.14),  $g^{ab}v_a v_b = -1$ , a direct expression for  $v_0$  in terms of  $v_1$ ,  $\beta$  and  $W$  can be written

<sup>2</sup>The notation used here is based on that of [10] and substituting  $W = V - r$  will give the original notation of Bondi in [16].

<sup>3</sup>In this chapter the velocity is notated as  $v^a$ .

as

$$v_0 = \frac{1}{2}v_1 \left(1 + \frac{W}{r}\right) + \frac{1}{2}e^{2\beta}v_1^{-1}. \quad (3.6)$$

Without any cosmological considerations, having the values on the initial null cone for  $\rho$  and  $v_1$ , equations (3.2) to (3.6) forms a hierarchical system that can be solved in the order (3.2), (3.3) and (3.6), then solving equations (3.4) and (3.5) evolves the system to the next null cone where the process can be repeated until the domain of calculation has been covered. Since these equations are all interdependent an iterative scheme is required for a numerical solution.

### 3.1.2 Cosmological considerations

While equations (3.1–3.6) are based on an outgoing family of null hypersurfaces (future null cones), observational models are concerned with the PNC, which requires that the sign of the  $dudr$  coefficient in the metric be negated i.e.

$$ds^2 = -e^{2\beta} \left(1 + \frac{W}{r}\right) du^2 + 2e^{2\beta} dudr + r^2 d\theta^2 + r^2 \sin^2 \theta d\varphi^2. \quad (3.7)$$

This leads to a similar set of equations with sign changes at various places. Alternatively, changing the order of integration, will also have the same effect, following from evaluating a null ray (i.e. on a radial null geodesic  $ds = d\theta = d\varphi = 0$  in equation 3.1) on the null cone:

$$-e^{2\beta} \left(1 + \frac{W}{r}\right) du^2 - 2e^{2\beta} dudr = 0 \quad (3.8)$$

$$du \neq 0 \Rightarrow r - r_1 = -\frac{1}{2} \int_{u_1}^{u_2} \left(1 + \frac{W}{r}\right) du = \frac{1}{2} \int_{u_2}^{u_1} \left(1 + \frac{W}{r}\right) du. \quad (3.9)$$

This approach will be preferred since it makes comparison with previous CIVP developments done for astrophysical scenarios more convenient.

Furthermore, the Bondi-Sachs CIVP is restricted in the radial coordinate  $r$  which is chosen to be the diameter distance ( $r = d_D$  in Section 2.3.1). This choice of coordinate is not suitable for high cosmological redshifts since  $r$  becomes multi-valued when the PNC refocusses at the AH (e.g. see Figure 2.3). In terms of extending the radial distance past the AH, the uniqueness of geodesics (refer to Theorem 1) facilitates a more suitable mechanism. In particular, an affine parameter on a null geodesic through the PNC vertex (see [36]), leads to a system of equations that is regular at the AH. It should be noted, however, that in an application based on real data rather than on data from a model, the issue of transforming measured distance data as luminosity or diameter distance to the affine parameter without assuming a model, remains problematic. Alternatively, it has been argued in [49] that the position of the AH is an observable property by itself and knowing this, the model can be adapted to compensate for refocussing, possibly using a similar approach to [51] where the AH was crossed in redshift space making use of series expansions (see Section 2.3.2). A final aspect to take note of is that  $r$  is not comoving *viz.*  $v^1 \neq 0$ . In regards to model independent observations, in noncomoving coordinates,  $z$  is interpreted as a recession of matter without the cosmological interpretation of it being the expansion of the Universe. Noncomoving coordinates also preserve the choice of

measure (e.g.  $z$ ,  $d_D$  or  $v$ ), as a coordinate, made on the initial PNC in the evolution equations as opposed to observer coordinates, where a change in the radial coordinate ( $y$ ) is made when evolving off the initial PNC (see Section 2.3.3).

As an observational cosmology problem, where the geometry is determined from direct observations, there are two subproblems to be solved:

- i. Reconstruct the geometry of the local PNC from directly observable quantities, such as redshift-distance and galaxy number counts.
- ii. Evolve the model as a reverse CIVP to determine the interior of the PNC using the values determined in (i) as initial conditions.

Although the accumulation of cosmological data in recent years has been astounding, these are not yet sufficiently complete for a practical implementation of the first problem, which will have to incorporate aspects such as data reduction and the sensitivity of the model to observational errors. These aspects are not considered in this work and only a conceptual description of the relations between observable quantities and the required input for the model will be presented in the next section. The second subproblem will be treated in detail in the remainder of this thesis through the development of a numerical code for the Bondi-Sachs CIVP and a CIVP based on an affine radial coordinate. By itself, this provides a mechanism for testing hypothesised models by evaluating the behaviour of their PNCs under given initial values. The PNC behaviours of different models given similar initial values are particularly interesting cases to investigate.

### 3.1.3 Reconstructing the metric

As initial data for the model,  $v_1(r)$  and  $\rho(r)$  have to be determined from observations on the PNC, which require measures of the radial distribution of expansion and density. These properties were derived by Bishop and Haines [12] and is presented here in a modified form where the redshift  $z$  and the diameter distance  $r_0$  are separated.

As a measure of expansion, redshift in terms of the luminosity distance ( $d_L$ ) can be determined from redshift-magnitude observations (e.g. SNIa observations). The reciprocity theorem is used to find a relation between  $z$  and  $r_0$  (see Section 2.3.1 and the references therein) where the zero subscript refers to value on the current PNC. Accordingly, observable quantities in terms of  $z$  can be written in terms of  $r_0$  through

$$z(d_L) \quad \text{and} \quad d_L = (1+z)^2 r_0 \Rightarrow z = z(r_0). \quad (3.10)$$

It should be taken into account that, since  $r_0$  will become multi-valued as the PNC refocusses, the AH will be the observational limit using the diameter distance as radial coordinate. Unfortunately, there is not a simple expression for  $z$  at the AH. In the special case of the EdS model [12], the AH is at  $z = 1.25$ , but this does not apply in general. As with observational coordinates, through (2.58), the redshift is directly related to the time component of the contravariant velocity:

$$1+z = \frac{du}{d\tau} = v^0 \quad (3.11)$$

where  $\tau$  is the proper time along general galactic world lines (see [36]). This can be used to determine the covariant velocity  $v_1$  on the observer PNC as

$$v_1(r_0) = -e^{2\beta}v^0 = -e^{2\beta}(1 + z(r_0)). \quad (3.12)$$

The observed number density ( $n_o$ ) is a directly measurable function of  $z$  which can be used as a measure of density if it can be related to the proper density  $\rho$ . It was shown in [12] that the proper number density ( $n_p$ ) is

$$n_p = \frac{n_o}{(1+z)}e^{-2\beta}. \quad (3.13)$$

The proper density is then related to the proper number count:

$$\rho(r_0) = f(n_p(r_0)). \quad (3.14)$$

For the discussion in this section it is sufficient to point out that the observed number density ( $n_o$ ) is related through the model variables to the proper number density, which is in turn related to the proper density ( $\rho$ ), required for the stress tensor in the EFEs. As pointed out in Section 2.3.1, this is in fact a more complicated relation but it will not be discussed in detail here. Therefore, also, the details of the relation  $f(n_p)$  will not be considered at this stage but in principle it must take into account aspects such as dark matter and source evolution, preferably with factors independent of an already assumed cosmological model. A more detailed discussion of density derivation will be given in Section 3.2.3.

Solving the CIVP from observational quantities, as with the observer coordinate method, requires that the values on the initial null cone be determined from observational quantities. These values will then be used as the initial values for the evolution into the local PNC. The solution on the initial null cone follows from equations (3.12) and (3.14) but they are dependent on  $\beta$  which is still unknown. Using equations (3.2), (3.12) and (3.14), a differential equation for  $\beta$  which is only dependent on observational quantities for the initial null cone can be set up as:

$$\beta_{,r_0} = 2\pi r_0 f(n_p(r_0))(-e^{2\beta}(1 + z(r_0)))^2. \quad (3.15)$$

This equation can be solved numerically with standard ODE techniques provided that  $f(n_p)$  is well behaved.

### 3.1.4 Coordinate transformations

The relationship between CIVP coordinates and CS coordinates is important for evaluating the model's suitability for cosmological modelling. Since the model is effectively the LTB model on the PNC, the most general metric it has to be transformed to is the standard LTB metric. For the purposes of model testing, the parabolic geometry will be used. As shown in Section 2.2.2 (equation (2.42)), the metric then becomes

$$ds^2 = -dt^2 + [R_{,\tilde{r}}(t, \tilde{r})]^2 d\tilde{r}^2 + R^2(t, \tilde{r})\{d\theta^2 + \sin^2\theta d\varphi^2\} \quad (3.16)$$

and its coefficients have to be related to the Bondi-Sachs coefficients of (3.1)<sup>4</sup>. For simplicity, the Bondi-Sachs metric (3.1) will be written in the form

$$ds^2 = -h_u du^2 - 2h_r du dr + r^2 \{d\theta^2 + \sin^2 \theta d\varphi^2\} \quad (3.17)$$

and the coefficients will be rewritten in terms of  $W$  and  $\beta$  afterwards. In the transformations that follow, the contravariant forms of (3.16) and (3.17) are required at places. These are

$$\tilde{g}^{ab} = \begin{pmatrix} -1 & 0 & 0 & 0 \\ 0 & [R, \tilde{r}(t, \tilde{r})]^{-2} & 0 & 0 \\ 0 & 0 & [R(t, \tilde{r})]^{-2} & 0 \\ 0 & 0 & 0 & [R(t, \tilde{r}) \sin \theta]^{-2} \end{pmatrix} \quad (3.18)$$

and

$$g^{ab} = \begin{pmatrix} 0 & -1/h_r & 0 & 0 \\ -1/h_r & h_u/h_r^2 & 0 & 0 \\ 0 & 0 & r^{-2} & 0 \\ 0 & 0 & 0 & [r \sin \theta]^{-2} \end{pmatrix} \quad (3.19)$$

for (2.31) and (3.17), respectively.

For numerical calculations,  $(u, r)$  will be known from the grid definition. Therefore, the most important aspect of the transformations is to relate the  $(u, r)$  coordinates to corresponding  $(t, \tilde{r})$  values. Since  $\theta$  and  $\varphi$  have the same meanings in both coordinate systems, an expression for  $r$  in terms of  $\tilde{r}$  and  $t$  can be obtained by comparing the coefficient of  $\{d\theta^2 + \sin^2 \theta d\varphi\}$  giving

$$R(t, \tilde{r}) = r. \quad (3.20)$$

A second expression containing  $u$ ,  $\tilde{r}$  and  $t$  can be found by doing a contravariant transformation from LTB coordinates for the  $g^{00}$  terms, which is equal to zero, using tensor transformation rules. A first order partial differential equation follows

$$\frac{\partial u}{\partial \tilde{r}} - [R, \tilde{r}(t, \tilde{r})] \frac{\partial u}{\partial t} = 0 \quad \text{with} \quad u(t, 0) = t \quad (3.21)$$

and, using the method of characteristics, this is written as<sup>5</sup>

$$\frac{dt}{d\tilde{r}} = -[R, \tilde{r}(t, \tilde{r})]. \quad (3.22)$$

Depending on the complexity of the  $R, \tilde{r}$  term, either numerical or analytic methods can be used to solve this equation.

Expressions containing partial derivatives for the other null cone terms can be obtained

---

<sup>4</sup>LTB variables that have the same symbols as the null cone variables will be notated using a tilde e.g.  $r_{LTB} = \tilde{r}$ ,  $v_{1 LTB} = \tilde{v}_1$ ,  $g_{LTB} = \tilde{g}$  etc.

<sup>5</sup>This also follows by calculating a null trace on the metric (3.16), i.e. setting  $ds = d\theta = d\varphi = 0$ .

from covariant tensor transformations. For  $h_r$  and  $h_u$  these are:

$$h_r = \frac{\partial t}{\partial u} \frac{\partial t}{\partial r} - [R_{,\tilde{r}}(t, \tilde{r})]^2 \frac{\partial \tilde{r}}{\partial u} \frac{\partial \tilde{r}}{\partial r} \quad (3.23)$$

$$h_u = \left( \frac{\partial t}{\partial u} \right)^2 - [R_{,\tilde{r}}(t, \tilde{r})]^2 \left( \frac{\partial \tilde{r}}{\partial u} \right)^2. \quad (3.24)$$

Having values for  $h_u$  and  $h_r$ , the Bondi-Sachs coefficients can be obtained from:

$$\beta = \frac{1}{2} \ln |h_r| \quad \text{and} \quad W = r(h_u h_r - 1). \quad (3.25)$$

In order to write  $v_1$  in null coordinates, transformation of the comoving velocity ( $\tilde{v}^a = (1, 0, 0, 0)$  and  $\tilde{v}_a = (-1, 0, 0, 0)$ ) into null coordinates is required. Using vector transformation laws, it follows that

$$v^0 = \frac{\partial u}{\partial t}, \quad v^1 = \frac{\partial r}{\partial t}, \quad v_0 = -\frac{\partial t}{\partial u} \quad \text{and} \quad v_1 = -\frac{\partial t}{\partial r}. \quad (3.26)$$

For numerical differentiation a five point difference scheme, such as defined in [19] can be used to determine the grid values of equations (3.23) and (3.24);  $v_1$  from (3.26) together with  $\rho$  from (2.45) are used as the input data on the initial null cone.

The results of the transformation of the EdS model to null coordinates were previously published in [12]. This provides a good illustration of the transformation process and is repeated here in more detail. With reference to the metric (2.47), which is normalised to  $t_0 = 1$ ,  $R(t, \tilde{r}) = t^{2/3} \tilde{r} = r$  in (3.20) and  $R_{,\tilde{r}}(t, \tilde{r}) = t^{2/3}$  in (3.22). Since  $R_{,\tilde{r}}(t, \tilde{r})$  only depends on  $t$ , the righthand and lefthand sides of (3.22) can be separated for  $\tilde{r}$  and  $t$  and the integral can be solved analytically:

$$\begin{aligned} \frac{dt}{d\tilde{r}} &= -[R_{,\tilde{r}}(t, \tilde{r})] = -t^{2/3} \\ \Rightarrow \int_0^{\tilde{r}} d\tilde{r}_* &= - \int_{t_0}^t t_*^{-2/3} dt_* \\ \Rightarrow \tilde{r} &= -\frac{1}{3}(t^{1/3} + t_0^{1/3}) \\ \Rightarrow t_0 &= \left( t^{1/3} + \frac{1}{3}\tilde{r} \right)^3 \end{aligned} \quad (3.27)$$

On the lines on which  $u$  is constant,  $u$  is a function of  $t_0$  i.e.  $u = F(t_0)$  and it then follows from the knowledge that  $u = t$  at  $\tilde{r} = 0$  that

$$u^{1/3} = \frac{1}{3}\tilde{r} + t^{1/3} \quad (3.28)$$

and from (3.20)

$$\tilde{r} = rt^{-2/3}. \quad (3.29)$$

Substituting (3.29) into (3.28) gives an explicit expression for  $t$  in terms of  $u$  and  $r$  <sup>6</sup>

$$t = \left[ \frac{1}{6} \left( -36r + 8u + 12\sqrt{9r^2 - 4ru} \right)^{1/3} + \frac{2}{3} \frac{u^{2/3}}{\left( -36r + 8u + 12\sqrt{9r^2 - 4ru} \right)^{1/3}} + \frac{1}{3} u^{1/3} \right]^3. \quad (3.30)$$

Equations (3.29) and (3.30) completely determine the  $(\tilde{r}, t) \rightarrow (u, r)$  relation. For comparison with the numerical solutions,  $(\tilde{r}, t)$  can be calculated from a grid defined in terms of  $(u, r)$ .

Equations (3.23) and (3.24) can be used to determine  $h_u$  and  $h_r$  by implicitly differentiating (3.28) and (3.29) towards  $u$  and  $r$ . For this particular case, however, analytical expressions can be obtained by derivatives towards  $t$  and  $\tilde{r}$  using the *implicit function theorem* (e.g. see [84] p.224). It is therefore, more convenient to work with contravariant transformations here. Transforming the  $g^{01}$  and  $g^{11}$  terms of (3.19) then gives:

$$g^{01} = \frac{\partial u}{\partial t} \frac{\partial r}{\partial t} \tilde{g}^{00} + \frac{\partial u}{\partial \tilde{r}} \frac{\partial r}{\partial \tilde{r}} \tilde{g}^{11} \Rightarrow h_r = \left[ \frac{\partial u}{\partial t} \frac{\partial r}{\partial t} - [R, \tilde{r}(t, \tilde{r})]^{-2} \frac{\partial u}{\partial \tilde{r}} \frac{\partial r}{\partial \tilde{r}} \right]^{-1} \quad (3.31)$$

and

$$g^{11} = \left( \frac{\partial r}{\partial t} \right)^2 \tilde{g}^{00} + \left( \frac{\partial r}{\partial \tilde{r}} \right)^2 \tilde{g}^{11} \Rightarrow h_u = h_r^2 \left[ - \left( \frac{\partial r}{\partial t} \right)^2 + [R, \tilde{r}(t, \tilde{r})]^{-2} \left( \frac{\partial r}{\partial \tilde{r}} \right)^2 \right]. \quad (3.32)$$

Implicitly differentiating toward  $t$  and  $\tilde{r}$  gives:

$$\frac{\partial u}{\partial t} = \frac{u^{2/3}}{t^{2/3}}, \quad \frac{\partial u}{\partial \tilde{r}} = u^{2/3}, \quad \frac{\partial r}{\partial t} = \frac{2}{3} \frac{\tilde{r}}{t^{1/3}} \quad \text{and} \quad \frac{\partial r}{\partial \tilde{r}} = t^{2/3}.$$

By substituting into (3.31) and (3.32) it then follows that:

$$h_r = - \frac{t^{4/3} u^{-2/3}}{t^{2/3} - \frac{2}{3} r t^{-1/3}} \quad (3.33)$$

$$h_u = \frac{t^{4/3}}{u^{4/3}} + \frac{4}{3} \left( \frac{r t u^{-4/3}}{t^{2/3} - \frac{2}{3} r t^{-1/3}} \right). \quad (3.34)$$

The equations in (3.25) can then be used to get the values for  $\beta$  and  $W$ .

From the comoving velocity ( $\tilde{v}^a = (1, 0, 0, 0)$ ), using a contravariant transformation and implicit differentiation, the null contravariant time components are

$$v^0 = - \frac{u^{2/3}}{t^{2/3}}, \quad v^1 = - \frac{2}{3} \frac{r}{t}.$$

By lowering the indices, in their covariant forms, the velocity components become

$$v_0 = v^a g_{0a} \Leftrightarrow v_0 = \frac{u^{2/3}}{t^{2/3}} h_u + \frac{2}{3} \frac{r}{t} h_r$$

---

<sup>6</sup>This was obtained using the computer algebra system Maple.

and

$$v_1 = v^a g_{1a} \Leftrightarrow v_1 = \frac{u^{2/3}}{t^{2/3}} h_r.$$

Since  $t$  is known in terms of  $(u, r)$  from (3.30),  $\rho$  on the null cone is calculated directly using equation (2.46)

$$\rho = \frac{1}{6\pi[t(u, r)]^2}. \quad (3.35)$$

It is interesting to point out here that as  $t$  varies with  $u$  and  $r$  on each null cone,  $\rho$  also varies i.e. even though the EdS model is homogeneous in conventional cosmological coordinates, null cones are not hypersurfaces of radial homogeneity and the model becomes inhomogeneous in null coordinates (see [81]).

## 3.2 Affine CIVP

### 3.2.1 Mathematical model

The main problem with the Bondi-Sachs CIVP, described in Section 3.1, is the fact that the diameter distance ( $r$ ) is not monotonically increasing and therefore not a unique coordinate. The uniqueness of geodesics (Theorem 1) facilitates a suitable mechanism to address this problem. In particular, an affine parameter on radial null geodesics provides a coordinate that is monotonically increasing for all distances on the PNC. For this, an affine characteristic formalism can be derived by doing a coordinate transformation from the Bondi-Sachs coordinates. Starting with the metric (3.1), an affinely parameterized geodesic in these coordinates is determined applying equation (2.9) to the radial coordinate as

$$\frac{d^2 r}{d\lambda^2} + \Gamma^1_{11} \left( \frac{dr}{d\lambda} \right)^2 = 0 \Rightarrow \frac{d^2 r}{d\lambda^2} + 2\beta_{,r} \left( \frac{dr}{d\lambda} \right)^2 = 0. \quad (3.36)$$

Setting  $\lambda = r$  at the origin provides the initial conditions  $r(0) = \lambda(0) = 0$  and  $dr/d\lambda|_{\lambda=0} = 1$  then solving gives

$$\frac{dr}{d\lambda} = e^{-2\beta}. \quad (3.37)$$

Applying tensor transformation laws and substituting (3.37) for all  $\partial r/\partial\lambda$  terms it follows that

$$\hat{g}_{10} = 2 \frac{\partial x^a}{\partial x_1} \frac{\partial x^b}{\partial x_0} g_{ab} = -2 \frac{\partial r}{\partial \lambda} \frac{\partial u}{\partial u} e^{2\beta} = -2e^{-2\beta} e^{2\beta} = -2, \quad (3.38)$$

which is in agreement with observer coordinates when  $y = v$ , see (2.91) on page 38. The  $\hat{g}_{00}$  term is determined through a tensor transformation as

$$\begin{aligned}\hat{g}_{00} &= \frac{\partial x^a}{\partial x_0} \frac{\partial x^b}{\partial x_0} g_{ab} = \frac{\partial u}{\partial u} \frac{\partial u}{\partial u} g_{00} + 2 \frac{\partial u}{\partial u} \frac{\partial r}{\partial u} g_{01} \\ &= -e^{2\beta} \left( 1 + \frac{W}{r} \right) - 2 r_{,u} e^{2\beta}.\end{aligned}$$

The physical significance of  $\beta$  as a separate variable is not of interest here and for simplicity, a new variable<sup>7</sup>  $\hat{W}(u, \lambda)$ , which implicitly absorbs  $\beta$  and  $r_{,u}$ , is introduced to form a metric term as  $\hat{g}_{00} := -(1 + \hat{W}/r)$ . The new variable should, however, have same behaviour at  $r = 0$  as  $W$  in the Bondi-Sachs CIVP and this follows from

$$\begin{aligned}- \left( 1 + \frac{\hat{W}}{r} \right) &= -e^{2\beta} \left( 1 + \frac{W}{r} \right) - 2 r_{,u} e^{2\beta} \\ \Rightarrow \hat{W} &= r \left( e^{2\beta} \left( 1 + \frac{W}{r} \right) - 2 r_{,u} e^{2\beta} \right) - r \\ \Rightarrow \hat{W} &= e^{2\beta} (r + W - 2r r_{,u}) - r \\ &\text{with } r = 0 \Rightarrow \hat{W} = W = 0.\end{aligned}$$

Then, a new metric with the radial coordinate  $\lambda$  follows as

$$ds^2 = - \left( 1 + \frac{\hat{W}(u, \lambda)}{\hat{r}(u, \lambda)} \right) du^2 - 2dud\lambda + \hat{r}(u, \lambda)^2 \{ d\theta^2 + \sin^2 \theta d\varphi^2 \}. \quad (3.39)$$

Substituting (3.39) into the EFEs, using the form  $R_{ab} = \kappa(T_{ab} - \frac{1}{2}Tg_{ab}) + \Lambda g_{ab}$ , with the stress-tensor for a dust-like fluid ( $T_{ab} = \rho v_a v_b$  and  $T = -\rho$ ) gives<sup>8</sup>

$$\hat{r}_{,\lambda\lambda} = -\frac{1}{2}\kappa\hat{r}\rho(v_1)^2 \quad (3.40)$$

$$\hat{r}_{,u\lambda} = \frac{1}{2} \left\{ \hat{W}_{,\lambda}\hat{r}_{,\lambda} + \hat{r}\hat{r}_{,\lambda\lambda} + \hat{W}\hat{r}_{,\lambda\lambda} - 2\hat{r}_{,u}\hat{r}_{,\lambda} - 1 + (\hat{r}_{,\lambda})^2 + \frac{1}{2}\kappa\rho\hat{r}^2 + \Lambda\hat{r}^2 \right\} / \hat{r} \quad (3.41)$$

$$\hat{W}_{,\lambda\lambda} = \frac{\hat{W}}{\hat{r}}\hat{r}_{,\lambda\lambda} + 4\hat{r}_{,u\lambda} + 2\kappa \left( v_0 v_1 \rho - \frac{1}{2}\rho \right) \hat{r} - 2\Lambda\hat{r} \quad (3.42)$$

with:  $\hat{r}(0) = \hat{W}(0) = \hat{W}_{,\lambda}(0) = \hat{r}_{,u}(0) = 0$  and  $\hat{r}_{,\lambda}(0) = 1$ .

Further, substituting the dust stress-tensor and (3.39) into the continuity equation,  $\nabla_b T^{ab} =$

<sup>7</sup>Quantities in terms of  $\lambda$  will be written with a caret (“^”). It should also be noted that the definition  $\hat{W} := W/r^2$  is sometimes used in NR which is different to its use here (e.g. equation 17 in [80]).

<sup>8</sup>To make provision for a larger set of cosmological models, the cosmological constant ( $\Lambda$ ) is introduced here as part of the model.

0, the energy-momentum equations follow

$$v_{1,u} = \frac{1}{v_1} \left\{ \left( \left( 1 + \frac{\hat{W}}{\hat{r}} \right) v_1 - v_0 \right) v_{1,\lambda} + \frac{1}{2} (v_1)^2 \left( \frac{\hat{W}_{,\lambda}}{\hat{r}} - \frac{\hat{W} \hat{r}_{,\lambda}}{\hat{r}^2} \right) \right\} \quad (3.43)$$

$$\begin{aligned} \rho_{,u} = \frac{1}{v_1} \left\{ \rho \left[ \left( 1 + \frac{\hat{W}}{\hat{r}} \right) \left( \frac{2v_1}{\hat{r}} \hat{r}_{,\lambda} + v_{1,\lambda} \right) - \left( \frac{2v_0}{\hat{r}} \hat{r}_{,\lambda} + v_{0,\lambda} \right) + \left( \frac{\hat{W}_{,\lambda}}{\hat{r}} - \frac{\hat{W} \hat{r}_{,\lambda}}{\hat{r}^2} \right) v_1 - \left( \frac{2\hat{r}_{,u}}{\hat{r}} \right) v_1 \right] \right. \\ \left. + \rho_{,\lambda} \left( \left( 1 + \frac{\hat{W}}{\hat{r}} \right) v_1 - v_0 \right) - \rho v_{1,u} \right\}. \end{aligned} \quad (3.44)$$

Making use of the normalisation condition,  $g^{ab}v_a v_b = -1$ ,  $v_0$  can be written in terms of  $v_1$  as

$$v_0 = \frac{1}{2} \left( 1 + \frac{\hat{W}}{\hat{r}} \right) v_1 + \frac{1}{2} v_1^{-1}. \quad (3.45)$$

Similar to the Bondi-Sachs CIVP, having the values on the initial null cone for  $\rho$  and  $v_1$ , equations (3.40) to (3.45) form a hierarchical system that can be solved in the order (3.40), (3.41), (3.42) and (3.45), then solving equations (3.43) and (3.44) evolves the system to the next null cone where the process can be repeated until the domain of calculation has been covered. These equations are all interdependent and require an iterative scheme for a numerical solution.

### 3.2.2 Cosmological considerations

The model introduced in section 3.2.1 is essentially a null cone formalism which makes provision for a null cone that can reconverge at some distance from the cone vertex. Taking  $G$  to be the world line of an observer located at the cone vertex and integrating into the past, these coordinates can be naturally aligned with a cosmological PNC. Further, it being spherically symmetric and radially inhomogeneous, classifies it as a LTB model in null coordinates. Using this model, the simulations done in [12] and [97] can be extended beyond the AH. Comparing Figures 3.1 and 3.2 illustrates the differences between conventional characteristic coordinates and the affine coordinates. Besides being not comoving, the affine coordinates closely resemble the observer coordinates as described in Section 2.3.3 and the references therein.

### 3.2.3 Reconstructing the metric

As with the Bondi-Sachs CIVP but in terms of  $\lambda$ , initial data for the model,  $v_1(\lambda)$  and  $\rho(\lambda)$  have to be determined from observations on the PNC. Measures of the radial distribution of expansion and density are again required but since  $\lambda$  is not an observable quantity the process is somewhat different. For the density distribution some additional complications are involved around the AH.

The procedure followed here is to write the observable quantities in terms of  $r$  and then find a relation between  $r$  and  $\lambda$  to get quantities in terms of  $\lambda$ . Since equations (3.10) and (3.11) are model independent the reciprocity theorem

$$z(d_L) \quad \text{and} \quad d_L = (1+z)^2 r_0 \Rightarrow z = z(r_0) \quad (3.46)$$

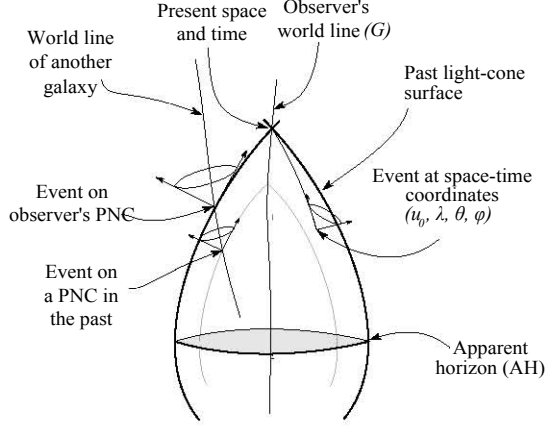


Figure 3.2: The affine CIVP coordinates for cosmology.

and redshift relation

$$1 + z = \frac{du}{d\tau} = v^0 \quad (3.47)$$

are exactly the same as that in Section 3.1.3 (also see Section 2.3.1 and the references therein). The covariant velocity  $v_1$  then follows in a slightly simpler form:

$$v_1(r_0) = -v^0 = -(1 + z(r_0)). \quad (3.48)$$

As a measure of proper density, observed galaxy number counts ( $N$ ) in terms of  $z$  can be used to determine  $\rho(r_0)$ . Writing the formula for  $\rho(z)$  from number counts (2.72) in terms of  $r$  it follows that

$$\rho(r_0) = \frac{\mathcal{M}_g}{(1 + z(r_0))J(r_0)^2 d\Omega_0} \left( \frac{dN}{dr} \frac{dr}{d\lambda} \right) \quad (3.49)$$

and by rearranging for brevity it can be written as

$$\rho(r_0) = \frac{\varrho_{obs}}{(1 + z)(r_0)^2} \left( \frac{dr}{d\lambda} \right) \quad \text{with} \quad \varrho_{obs} = \frac{\mathcal{M}_g}{Jd\Omega_0} \left( \frac{dN}{dr} \right) \quad (3.50)$$

where  $\varrho_{obs}$  consists of quantities determined from observations.

From (3.48) and (3.50) the required values of  $\rho$  and  $v_1$  are obtainable in terms of the diameter distance ( $r$ ). Since these are required in terms of  $\lambda$ , interchanging the independent variable in (3.40) provides a method to express  $\lambda$  in terms of  $r$ . Starting then with (3.40), rewritten as a system of ODEs, introducing  $\hat{S}$ ,

$$\hat{r}_{,\lambda} = \hat{S} \quad (3.51)$$

$$\hat{S}_{,\lambda} = \hat{r}_{,\lambda\lambda} = -\frac{1}{2}\kappa\hat{r}\rho(v_1)^2 \quad (3.52)$$

with:  $\hat{r}(0) = 0$  and  $\hat{S}(0) = 1$ ,

then interchanging the roles of  $\lambda$  and  $r$ , simplifying, rearranging and introducing  $\hat{U} = \hat{S}^{-1}$  provides ODE expressions for  $\lambda_{,\hat{r}\hat{r}}$

$$\lambda_{,\hat{r}} = \hat{U} \quad (3.53)$$

$$\hat{U}_{,\hat{r}} = \lambda_{,\hat{r}\hat{r}} = \left( \frac{1}{2} \kappa \hat{r} \rho(r_0) (v_1)^2 \right) \hat{U}^3 \quad (3.54)$$

with:  $\lambda(0) = 0$  and  $\hat{U}(0) = 1$ .

Furthermore, substituting equations (3.48) and (3.49) into (3.54) gives a relation in terms of observational quantities

$$\lambda_{,\hat{r}\hat{r}} = \frac{1}{2} \kappa \frac{\rho_{obs}}{\hat{r}} (1+z) (\lambda_{,\hat{r}})^2 \quad (3.55)$$

with:  $\lambda(0) = 0$  and  $\lambda_{,\hat{r}}(0) = 1$ .

Although these equations will not be solved at this stage, there are some complications that will require special consideration. These arise from the fact that the diameter distance in an expanding universe is not necessarily monotonically increasing and therefore, not a unique independent variable. In these cases,  $\hat{r}$  reaches a maximum and then decreases. At the maximum diameter distance, the AH,  $\hat{r}_{,\lambda} = 0$  and  $\lambda_{,\hat{r}}$  is singular. In general, this can be overcome by separating the solution into regions prior, around and succeeding the AH where the region around the AH is solved using series expansions. The  $\hat{r}$  denominator in (3.55) will also require special consideration with series expansions around  $\hat{r} = 0$ . Such considerations were previously implemented in [51] to handle singularities around the AH and the origin for LTB models. The uniqueness of  $r$  around the AH is a recurring theme in this thesis and since it was the reason for modifying the Bondi-Sachs CIVP to the affine CIVP, it should be emphasised that this problem is only present on the initial PNC here; the evolution procedure is completely free of singularities at the AH.

Under the assumption that the Universe can be generalised as a LTB cosmology, [49] followed by [4] and [50], derived a relationship for the cosmological constant  $\Lambda$  involving the maximum value of  $\hat{r}$  and matter data within the PNC. In order to test the theory of gravity more generally, a measurement involving a rate of change over time is required. Redshift drift  $\partial z / \partial u(z)$  [96], which is one of the design objectives of the CODEX spectrograph planned for the European Extremely Large Telescope (E-ELT) [75], can be used for this purpose. Supposing  $\partial z / \partial u(z)$  data is available and can be written in terms of  $\lambda$ , then from the definition of  $v^1$

$$v^1 = \frac{\partial \lambda}{\partial u} = \frac{d\lambda}{dz} \frac{\partial z}{\partial u}, \quad (3.56)$$

lowering the index of  $v^0$

$$v_0 = - \left( 1 + \frac{\hat{W}}{\hat{r}} \right) v^0 + (-1)v^1 \quad (3.57)$$

and substituting (3.56) and (3.48) into (3.57)

$$v_0 = \left(1 + \frac{\hat{W}}{\hat{r}}\right) v_1 - \frac{d\lambda}{dz} \frac{\partial z}{\partial u}. \quad (3.58)$$

Further, substituting (3.58) into (3.45) gives

$$\hat{W} = \hat{r} \left( \frac{1}{(v_1)^2} + \frac{2}{v_1} \frac{d\lambda}{dz} \frac{\partial z}{\partial u} - 1 \right) \quad (3.59)$$

and using (3.48),  $W$  can be written in terms of  $z$  and through  $z(\lambda)$  in terms of  $\lambda$

$$\hat{W} = \hat{r} \left( \frac{1}{(1+z)^2} - \frac{2}{(1+z)} \frac{d\lambda}{dz} \frac{\partial z}{\partial u} - 1 \right). \quad (3.60)$$

Since  $\hat{r}$ ,  $\hat{W}$  and  $\hat{r}_{,u} = (d\hat{r}/dz)(\partial z/\partial u)$  as well as, through numerical differentiation, their derivatives towards  $\lambda$  are known, the cosmological constant can now be obtained by rearranging (3.42) as

$$\Lambda = \frac{1}{2} \left( \frac{\hat{W}}{\hat{r}} \hat{r}_{,\lambda\lambda} + 4\hat{r}_{,u\lambda} + 2\kappa \left( v_0 v_1 \rho - \frac{1}{2}\rho \right) \hat{r} - \hat{W}_{,\lambda\lambda} \right) / \hat{r}. \quad (3.61)$$

Since  $\Lambda$  is expected to be constant, this equation only needs to be used on one point where all the values are known while on the other hand, testing the formula at different points can provide insight into  $\Lambda$ 's constancy.

The derivations in this section assumes that data is already available as smooth functions of the observable quantities. Actual observations, however, require data reduction and smoothing techniques, which is a challenging endeavour by itself. In the LTB models investigated in [51] and [63], data reduction methods were investigated which provide valuable insight into the methodology of converting realistic data into useful initial data. In combination with the methods introduced in this section, all options will have to be considered when data of sufficient completeness becomes available for observational models.

### 3.2.4 Coordinate transformations

In order to measure the model's applicability to cosmology, the model will be compared to known solutions in Chapter 5. For this, coordinate transformations from CS coordinates to affine null coordinates are described in this section. These transformations follow directly from calculating the geodesic paths in space and time. The general form, equation (2.9), is repeated here as reference

$$\frac{d^2 x^\mu}{d\lambda^2} + \Gamma^\mu_{\nu\sigma} \frac{dx^\nu}{d\lambda} \frac{dx^\sigma}{d\lambda} = 0. \quad (3.62)$$

The parabolic LTB metric (2.31) will again be used as a general transformation metric.

Using (3.62), the geodesic equations for the LTB model becomes

$$\frac{d^2 t}{d\lambda^2} + \Gamma^0_{11} \left( \frac{d\tilde{r}}{d\lambda} \right)^2 = 0 \quad (3.63)$$

$$\frac{d^2 \tilde{r}}{d\lambda^2} + 2\Gamma^1_{01} \frac{dt}{d\lambda} \frac{d\tilde{r}}{d\lambda} + \Gamma^1_{11} \left( \frac{d\tilde{r}}{d\lambda} \right)^2 = 0. \quad (3.64)$$

When scaled to some maximum time,  $t_0$ , as the current age of a universe, the conditions at  $\lambda = 0$  are  $t = t_0$  and  $\tilde{r} = 0$  with the initial directions constrained to be null by  $dt/d\lambda = 1$  and  $d\tilde{r}/d\lambda = R(t_0, 0)$ . As comparative values on a null cone grid, the covariant velocity follows directly from  $v_1 = dt/d\lambda$ , the diameter distance from  $\hat{r}(\lambda) = R(t, \tilde{r}(\lambda))$ , while  $\rho$  is determined from the coordinate expression for the specific model using  $(t(\lambda), \tilde{r}(\lambda))$  as the coordinates for  $t$  and  $r$  on a null cone.

The normalised EdS model will now be used to demonstrate the process of comoving to affine transformations. When substituting the metric (equation (2.47)) into equations (3.63) and (3.64), a system of equations for  $t(\lambda)$  and  $r(\lambda)$  is obtained<sup>9</sup>

$$\frac{d^2 t}{d\lambda^2} + \frac{2}{3} t^{1/3} \left( \frac{d\tilde{r}}{d\lambda} \right)^2 = 0 \quad (3.65)$$

$$\frac{d^2 \tilde{r}}{d\lambda^2} + \frac{4}{3} t^{-1} \frac{dt}{d\lambda} \frac{d\tilde{r}}{d\lambda} = 0. \quad (3.66)$$

At  $\lambda = 0$ :  $t = 1$ ,  $\tilde{r} = 0$ ,  $dt/d\lambda = -1$  and  $d\tilde{r}/d\lambda = t^{-2/3}$ .

Solving these equations numerically provides a useful example of the motivation for working with an affinely parameterized radial coordinate as opposed to the diameter distance. This is illustrated in Figure 3.3 where the diameter distance and affine parameter is plotted against the redshift. In terms of observations, with the emphasis on the AH at  $z = 1.25$ , the diameter distance reaches its maximum and then decreases while  $\lambda$  keeps on increasing and provides a unique coordinate for higher redshifts.

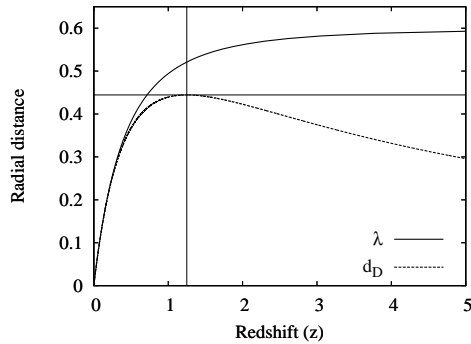


Figure 3.3: The radial distance coordinates  $d_D = r(z)$  and  $\lambda$  related to  $z$ , which is a common observational measure.

<sup>9</sup> $\tilde{r}$  in this section again refers to its definition in Chapter 2 i.e. as the comoving radial coordinate.

Substituting  $t(\lambda)$  into equation (2.46) provides the density profile on a specific null cone

$$\rho = \frac{1}{6\pi[t(\lambda)]^2}. \quad (3.67)$$

As previously mentioned, it is apparent that as  $t$  varies with  $\lambda$  on each null cone,  $\rho$  also varies, pointing out the fact that null cones are not hypersurfaces of radial homogeneity and the model becomes inhomogeneous in null coordinates (see [81]).

### 3.3 Conclusion

In this chapter, it was shown how to implement the characteristic formalism, which is usually associated with gravitational waves, as a model that represents the observable universe. For this, the CIVP in Bondi-Sachs coordinates was presented in spherical symmetry with the matter content being a dust-like fluid. This represents the LTB model in null coordinates. Since the model was originally developed to study gravitational waves, some cosmological considerations have to be taken into account. Firstly, the cosmological observer is concerned with the PNC while the model was developed for a future null cone. This has been accounted for by changing the direction of integration on the null cone. Secondly, the Bondi-Sachs coordinates are not comoving and velocity components are present, which are not usually present in cosmological models. The third aspect, which constitutes a major part of this thesis, is the behaviour of the diameter distance as radial coordinate. In particular,  $(r = d_D)$  becomes multi-valued around the AH.

To address the limitation of the radial coordinate of the Bondi-Sachs CIVP, a model was derived where the diameter distance ( $r$ ) was replaced by an affine parameter ( $\lambda$ ) on null geodesics, tracing out the surface of the PNC of a cosmological observer. The resulting *affine CIVP*, is well behaved well beyond the AH. In addition, the cosmological constant is included in the model, making it suitable to investigate the PNC behaviour of models where both inhomogeneities and the cosmological constant play a role. The model is particularly suitable for investigating the past evolution of the Universe where the current PNC is used as the initial values of a reversed CIVP. In order to do this, however, the initial values have to be determined from direct observations on the PNC. In Sections 3.1.3 and 3.2.3 it is shown how the required initial values can be obtained from the observable quantities, described in Section 2.3.1.

With these models at hand, Chapter 4 will present numerical codes for calculations in null coordinates of the past evolution of a cosmological PNC. In order to measure the accuracy of this code, comparisons with known models are required. For this purpose, in this chapter, it was shown how transformations for some known cosmologies are done from comoving to null coordinates. These transformations are used in Chapter 5 where the accuracy of the numerical code will be tested. This will also be used to generate initial values for comparisons between LTB and  $\Lambda$ CDM models.

# Chapter 4

## Numerical code

The CIVP equations in the Bondi-Sachs and affine representations, form a hierarchical system of differential equations that can be solved if the values of  $\rho$  and  $v_1$  are known on some initial null cone. As already demonstrated, the PNC of a cosmological observer can be the initial null cone for the CIVP by deriving the values of  $\rho$  and  $v_1$  from astronomical observations. This chapter is concerned with a numerical scheme to solve the CIVP equations assuming that  $\rho$  and  $v_1$  have already been derived from observations. This not only involves the development of a code to solve the CIVP equations but, to obtain second order convergence, special considerations at the domain boundaries. These considerations are described in detail in this chapter.

### 4.1 Bondi-Sachs CIVP

#### 4.1.1 Mathematical algorithm

The CIVP equations can be arranged in a convenient hierarchy where the solution of each equation provides a value to an unknown variable of the next equation. Starting from  $\rho$  and  $v_1$  values on the initial null cone, the hypersurface equations (4.1 and 4.2), which are ODEs of  $r$  on characteristic curves calculated on one time step, provide the input to the evolution equations (4.4 and 4.5), which are partial differential equations (PDEs) of  $r$  and  $u$  evolving the solution to the next time step. A solution is then obtained by iterating through the hierarchy, until all values converge.

Repeated here in the order in which they will be solved, the CIVP equations are

$$\beta_{,r} = 2\pi r \rho (v_1)^2 \tag{4.1}$$

$$W_{,r} = e^{2\beta} - 1 - 4\pi e^{2\beta} \rho r^2 \tag{4.2}$$

with  $\beta = W = 0$  at  $r = 0$ .

$$v_0 = \frac{1}{2}v_1 \left(1 + \frac{W}{r}\right) + \frac{1}{2} \frac{e^{2\beta}}{v_1} \quad (4.3)$$

$$v_{1,u} = \left(2v_0 - \left(1 + \frac{W}{r}\right)v_1\right)\beta_{,r} + \frac{1}{2}v_1 \left(\frac{W_{,r}}{r} - \frac{W}{r^2}\right) + \left(\left(1 + \frac{W}{r}\right) - \frac{v_0}{v_1}\right)v_{1,r} \quad (4.4)$$

$$\rho_{,u} = \frac{1}{v_1} \left\{ \rho \left[ \left(1 + \frac{W}{r}\right) \left(\frac{2v_1}{r} + v_{1,r}\right) - \left(\frac{2v_0}{r} + v_{0,r}\right) + \left(\frac{W_{,r}}{r} - \frac{W}{r^2}\right)v_1 \right] + \left(\left(1 + \frac{W}{r}\right)v_1 - v_0\right)\rho_{,r} - \rho v_{1,u} \right\} \quad (4.5)$$

The hierarchy of the CIVP is followed by repeating the steps below until the calculation has sufficiently converged.

- i. Calculate  $\beta$  using the initial values of  $\rho$  and  $v_1$  with (4.1).
- ii. Calculate  $W$  using  $\beta$  and  $\rho$  with (4.2).
- iii. Calculate  $v_0$  using  $v_1$ ,  $\beta$  and  $W$  with (4.3).
- vi. Calculate  $v_1$  for the next time step using  $\beta$ ,  $W$  and  $v_0$  with (4.4).
- v. Calculate  $\rho$  for the next time step using  $\rho$ ,  $v_0$ ,  $v_1$ ,  $\beta$  and  $W$  with (4.5).

By incorporating practical and theoretical aspects of the grid definition and conditions at the  $r$ -boundaries, the development of a second order convergent scheme is the objective in this chapter.

### 4.1.2 The grid and domain of calculation

The domain of calculation is the interior region of the PNC starting from the present spacetime location up to a region approaching the point where the null cone starts to refocus at the AH. As pointed out earlier, at the AH, the PNC reaches its maximum diameter and then starts to contract, which causes the null cone coordinate system to become multi-valued. The calculations presented in this work will be restricted to the well-behaved region before refocussing by introducing a characteristic line at the radial extent as a causal cut-off limit. This is required because the grid definition is not causally aligned and can include values that are theoretically not in causal contact with the past or future of the initial values. In principle, these values are artificial and solutions beyond the cut-off limit will be discarded.

A rectangular grid is used to represent the PNC as illustrated in Figure 4.1. The radial limit will initially be taken to be halfway to the theoretical refocussing point and will then be increased gradually to find the maximum region of stability for a specific model. Since the refocussing location is known analytically for the EdS model it will be used as a simple illustration of the grid generation. Normalised to a current age of  $t_0 = u_0 = 1$ , from equation (2.51), the domain of calculation for the EdS model is:

$$0 \leq r \leq B_r \frac{4}{9} \quad \text{and} \quad 1 \geq u \geq B_u \frac{8}{27}$$

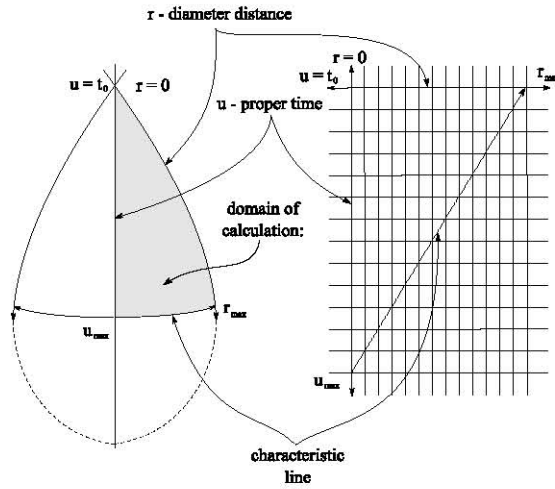


Figure 4.1: The past null cone calculated on a rectangular grid.

with  $B_r$  and  $B_u$  initially 0.5 and then increased gradually until the maximum region of stability is reached. This domain is then reduced to a domain of interest by making use of the characteristic cut-off line, which is described in more detail in Section 4.1.4.

The interior grid points for  $u$  and  $r$  are generated using

$$\begin{aligned} r_{j+1} &= r_j + \Delta r \quad \text{for } j = 1, 2, \dots, NJ \\ u^{i+1} &= u^i - \Delta u \quad \text{for } i = 1, 2, \dots, NI \end{aligned}$$

where

$$\Delta r = \frac{r_{max} - r_1}{NJ - 1} \quad \text{and} \quad \Delta u = \frac{u^{max} - u^1}{NI - 1}.$$

Here,  $NJ$  is the number of spatial grid points,  $NI$  the number of time steps and a convention is followed where spatial indices are notated using a subscript and time indices superscripts. The values of  $NJ$  and  $NI$  are chosen to provide a grid spacing that will be well within the stability expectation of the *Courant-Friedrichs-Lewy* (CFL) condition for simpler similar first-order PDEs (e.g. the Burgers' equation)

$$\left| \frac{\Delta u}{\Delta r} v_{1max} \right| \leq 1.$$

This is, however, only used as a guideline since the stability conditions were not derived specifically for the CIVP. It was found that second order stable solutions were obtainable by using reasonable *Courant numbers* ( $|(\Delta u / \Delta r) v_{1max}| \leq 0.5$ ) without needing to modify the grid generation method. This was done by taking into consideration that the number of grid point, on the regular grid, reduces at each time step as the PNC in the past becomes smaller (see Figure 4.1). The CFL should, therefore, at least apply to the youngest (smallest) PNC.

### 4.1.3 Numerical scheme

The code described in this section is based on the 3D code developed in [10] and [11] but simplified for dust and spherical symmetry. The overall numerical scheme is an explicit predictor-corrector method based on steps halfway between the  $r$  and  $u$  grid points. A combination of second and higher order finite difference methods on a regular grid are used in the implementation of the scheme in this section. The objective has been to obtain overall second order convergence in both space and time up to a distance reasonably close to the restriction imposed by the AH. With reference to Figure 4.2, the algorithm is described referring to equations (4.1) and (4.2) as the hypersurface equations and equations (4.4) and (4.5) as the evolution equations.

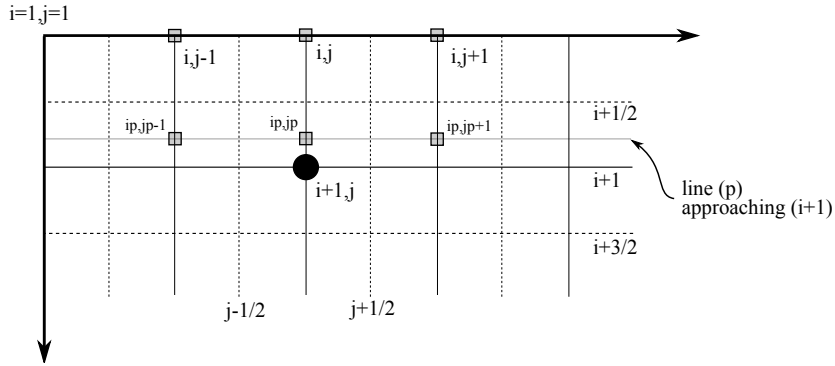


Figure 4.2: Stencil for numeric solution: points indicated with shaded squares are used to calculate the point indicated by the solid dot.

#### Hypersurface equations

Solving the hypersurface equations is done with a central difference method on half steps between the  $r$ -grid points, using

$$g_j^i = g_{j-1}^i + \frac{\Delta r}{2} [(g_{,r})_j^i + (g_{,r})_{j-1}^i] \quad (4.6)$$

where  $g$  represents  $\beta$  or  $W$  and  $g_{,r}$  the left-hand sides of equations (4.1) or (4.2) respectively. Further,  $i$  is notated as the discrete time step and  $j$  the discrete radial step.  $(g_{,r})_j^i$  is then calculated by substituting the values of  $v_1$  and  $\rho$  of the most recent iteration into equations (4.1) and (4.2), starting with the known initial values.

## Evolution equations

In order to calculate the evolution equations, the general form of equations (4.4) and (4.5) can be written as

$$v_{1,u} = F_{v1} \quad \text{and} \quad \rho_{,u} = F_{\rho} \quad (4.7)$$

with

$$\begin{aligned} F_v &= \left(2v_0 - \left(1 + \frac{W}{r}\right)v_1\right)\beta_{,r} + \frac{1}{2}v_1\left(\frac{W_{,r}}{r} - \frac{W}{r^2}\right) + \left(\left(1 + \frac{W}{r}\right) - \frac{v_0}{v_1}\right)v_{1,r} \\ F_{\rho} &= \frac{1}{v_1}\left\{\rho\left[\left(1 + \frac{W}{r}\right)\left(\frac{2v_1}{r} + v_{1,r}\right) - \left(\frac{2v_0}{r} + v_{0,r}\right) + \left(\frac{W_{,r}}{r} - \frac{W}{r^2}\right)v_1\right] \right. \\ &\quad \left. + \left(\left(1 + \frac{W}{r}\right)v_1 - v_0\right)\rho_{,r} - \rho v_{1,u}\right\}. \end{aligned}$$

Second order difference equations for  $v_1$  and  $\rho$  can then be written as:

$$v_{1j}^{n+1} = v_{1j}^n + \Delta u F_{vj}^{n+1/2} = v_{1j}^n + \frac{\Delta u}{2}(F_{vj}^n + F_{vj}^{n+1}) \quad (4.8)$$

$$\rho_j^{n+1} = \rho_j^n + \Delta u F_{\rho j}^{n+1/2} = \rho_j^n + \frac{\Delta u}{2}(F_{\rho j}^n + F_{\rho j}^{n+1}). \quad (4.9)$$

Here,  $n$  is a time iterator that will approach  $i+1$ . In these equations, the hypersurface derivatives are obtained by substituting the values of the most recent iteration at point  $(i, j)$  in Figure 4.2 directly into the numerical form of equations (4.1) and (4.2):

$$\begin{aligned} \beta_{,rj}^n &= 2\pi r_j \rho_j^n (v_{1j}^n)^2 \\ W_{,rj}^n &= e^{2\beta_j^n} - 1 - 4\pi e^{2\beta_j^n} \rho_j^n r_j^2. \end{aligned}$$

Radial matter derivatives are calculated making use of standard central difference formulae (see for instance [19] page 160-161):

$$f_{,rj} = \frac{1}{2\Delta r}[f_{j+1} - f_{j-1}] + \mathcal{O}(h^2).$$

The region where these derivatives are calculated can allow for more accurate difference approximations; the five-point formulae given in [19] can also be used here:

$$f_{,rj} = \frac{1}{12\Delta r}[f_{j-2} - 8f_{j-1} + 8f_{j+1} - f_{j+2}] + \mathcal{O}(h^4).$$

This will then modify Figure 4.2 with one additional shaded square on each side of the calculated grid point. Near the boundaries the one-sided versions of these formulae can be used. These are:

$$\begin{aligned} f_{,rj} &= \frac{1}{2\Delta r}[-3f_j + 4f_{j+1} - f_{j+2}] + \mathcal{O}(h^2) \quad \text{and} \\ f_{,1rj} &= \frac{1}{12\Delta r}[-25f_j + 48f_{j+1} - 36f_{j+2} + 16f_{j+3} - 3f_{j+4}] + \mathcal{O}(h^4) \end{aligned}$$

for the three-point and five point formulae respectively.

### Algorithm

The mathematical algorithm of Section 4.1.1 can now be implemented for the explicit scheme as follows:

- i. Set the  $\rho$  and  $v_1$  initial values on to the initial grid points. These values will, in principle, be obtained from observations.
- ii. From the initial values of  $\rho$  and  $v_1$ , calculate  $\beta$  and  $W$  from (4.1) and (4.2) using (4.6) and  $v_0$  from (4.3).
- iii. Calculate  $F_j^1$ , using (4.7) the from the initial values of  $v_1$ ,  $\rho$  and the values calculated for  $\beta$ ,  $W$  and  $v_0$  in (ii).
- iv. Set  $F_j^{n+1/2} = F_j^1$  and calculate  $v_1$  and  $\rho$ , using (4.8) and (4.9), as an initial approximation that will approach the actual values with subsequent iterations.
- v. Use the new values of  $v_1$  and  $\rho$  to calculate  $\beta$ ,  $W$  and  $v_0$  and their radial derivatives, as was done in step (ii).
- vi. Calculate  $F_j^{n+1/2}$  from values in (v) and again  $v_1$  and  $\rho$ .
- vii. Test the calculations in (vi) for accuracy and convergence. If they are sufficiently accurate, move to the next time step, otherwise repeat steps (v) and (vi) with the new values of  $v_1$  and  $\rho$ .

### 4.1.4 Boundary regions

#### Inner region $r \approx 0$

Evaluating the CIVP equations, it is evident that the terms with  $r$  and  $r^2$  denominators are not mathematically suitable at  $r = 0$  and numerically problematic to calculate around  $r \approx 0$ , especially with finite difference methods. The  $r \approx 0$  region will therefore require special treatment by making use of series expansions instead of the previously described numerical scheme.

In order to do this, all the variables in the CIVP equations are replaced by power series expressions from which the unknown terms can then be calculated by comparing coefficients in the resulting expressions. In principle, these would be infinite series but for practical reasons only the terms required to produce second order accuracy will be used i.e.:

$$v_{1,u} = v_{1u0} + v_{1u1}r + v_{1u2}r^2 + \mathcal{O}(r^3) \quad (4.10)$$

$$\rho_{,u} = \rho_{u0} + \rho_{u1}r + \rho_{u2}r^2 + \mathcal{O}(r^3) \quad (4.11)$$

The method for solving these equations can be summarised in the following steps:

- i. Write the functions  $\beta(r)$ ,  $W(r)$ ,  $v_1(r)$  and  $\rho(r)$  as series expansions. It should be taken into account that second order expansions of  $\beta$  and  $W$  do not produce second order results

in  $v_1(r)$  and  $\rho(r)$ . Therefore, initially six terms are used to evaluate how many terms are required to produce second order truncations of equations (4.10) and (4.11).

- ii. Substitute the values calculated in (i) into equations (4.1 – 4.5) using (4.10) and (4.11) as the left hand sides of (4.4) and (4.5).
- iii. Simplify the resulting equations by comparing coefficients until all expansions are expressions in terms of:

$$\begin{aligned} v_0 &= v_{00} + v_{01}r + v_{02}r^2 + v_{03}r^3 \\ v_1 &= v_{10} + v_{11}r + v_{12}r^2 + v_{13}r^3 \\ \rho &= \rho_0 + \rho_1r + \rho_2r^2. \end{aligned}$$

Taking into account that the expansions are effectively Taylor series expansions, some of the hypersurface coefficients can be eliminated by determining the higher derivatives of equations (4.1) and (4.2).

- iv. The coefficients in step (iii) will provide all the required terms for the left hand sides of the series evolution equations.

The series functions are then be used as the  $F_\rho$  and  $F_{v_1}$  terms in equations in (4.7). The resulting equations were determined using the computer algebra system, Maple, and are quite long and therefore only their general form is given here:

$$\begin{aligned} v_{00} &= v_{10} & v_{01} &= 0 \\ v_{02} &= f(\rho_0, v_{11}) & v_{03} &= f(\rho_0, \rho_1, v_{11}, v_{12}) \\ v_{1u0} &= 0 & v_{1u1} &= f(\rho_0, v_{11}) \\ v_{1u2} &= f(\rho_0, \rho_1, v_{11}, v_{12}) & \rho_{u0} &= f(\rho_0, v_{11}) \\ \rho_{u1} &= f(\rho_0, \rho_1, v_{11}, v_{12}) & \rho_{u2} &= f(\rho_0, \rho_1, \rho_2, v_{11}, v_{12}, v_{13}). \end{aligned}$$

The terms that cannot be eliminated by any previous results are:  $\rho_0, \rho_1, \rho_2, v_{11}, v_{12}$  and  $v_{13}$ . These values can then be obtained by implementing an interpolation scheme which replaces the full evolution equations around the origin. Since there are three  $\rho$  unknowns and three  $v_1$  unknowns, three interpolations points can be used on two equations, which provide six equations for the six unknowns. The region where series expansions is required is therefore calculated three grid points at a time.

For the region where the series solution meets with the CIVP solution, smooth transitions are required and this also requires special consideration to avoid artificial instabilities. A procedure is then followed where the merger region is blended smoothly by using weighted average functions between the two solutions. Both a *sine*

$$bl(r) = \frac{1}{2} + \frac{1}{2} \sin \left( \pi \left[ \frac{r - r_{blmin}}{r_{blmax} - r_{blmin}} \right] - \frac{\pi}{2} \right) \quad (4.12)$$

and a *hyperbolic tangent* function

$$bl(r) = \frac{1}{2} + \frac{1}{2} \tanh \left( 10 \left[ \frac{r - r_{blmin}}{r_{blmax} - r_{blmin}} \right] - 5 \right). \quad (4.13)$$

were found to be adequate for the required calculations. In these functions,  $r_{blmin}$  and  $r_{blmax}$  are the locations where the merger function is started and ended. In the merger region  $F_{v_1}$  and  $F_\rho$  are then calculated as

$$\begin{aligned} F_{v_1} &= [1 - bl(r)]F_{v_1 \text{ series}} + [bl(r)]F_{v_1 \text{ civp}} \\ F_\rho &= [1 - bl(r)]F_{\rho \text{ series}} + [bl(r)]F_{\rho \text{ civp}}. \end{aligned}$$

The exact size of the merger region is different for different models and the different blending functions were also more favourable for different models.

### Outer region

Since the purpose of the code is to solve the CIVP equations in a region that can, in principle, be validated against direct observations, the extent of the interior null cone must be limited by some causally connected boundary. This causal outer boundary does not correspond to the radial outer limit of the grid definition. For verification runs where known results are available, it can easily be identified when calculations correspond to expected values even beyond the causal boundary. However, when calculating from initial data where no known data is available, results cannot be assumed to be correct on grid points which are not causally connected.

To restrict the calculations to the causally connected region, the outer boundary is formed by connecting the radial limit of the initial null cone to the youngest null cone using an incoming null ray (i.e. on a radial null geodesic  $ds = d\theta = d\varphi = 0$ ). Applied to (3.1), it follows that

$$-e^{2\beta} \left(1 + \frac{W}{r}\right) du^2 - 2e^{2\beta} du dr = 0 \quad (4.14)$$

$$du \neq 0 \Rightarrow r - r_1 = -\frac{1}{2} \int_{u_1}^u \left(1 + \frac{W}{r}\right) du_*. \quad (4.15)$$

Numerically this can be solved by using an iterative scheme which starts at  $r_{NJ}$  on the observer PNC, and predicting the solution as

$$r_i = r_{i-1} - \frac{1}{2} \Delta u, \quad (4.16)$$

from which  $W(r_i)$  can be estimated to calculate

$$r_i = r_{i-1} - \frac{1}{2} \left(1 + \frac{W(r_i)}{r_i}\right) \Delta u. \quad (4.17)$$

This is repeated until the value of  $r_i$  converges. Since the value of  $r_i$  does not necessarily fall directly on grid points,  $W(r_i)$  is determined by linearly interpolating between the closest grid points and a specific  $u_i$  grid line.

## 4.2 Affine CIVP code

### 4.2.1 Mathematical algorithm

The numerical scheme described here is in structure similar to the finite difference scheme described in Section 4.1, which in turn was based on the general 3D code developed in [10] and [11]. Since the CIVP scheme is based on first order ODEs, the second order hypersurface equations (3.40)-(3.42) are rewritten by introducing  $\hat{R}(u, \lambda) = \hat{r}_{,u}$ ,  $\hat{S}(u, \lambda)$  and  $\hat{T}(u, \lambda)$ , which then gives:

$$\hat{r}_{,\lambda} = \hat{S} \quad (4.18)$$

$$\hat{S}_{,\lambda} = \hat{r}_{,\lambda\lambda} = -\frac{1}{2}\kappa\hat{r}\rho(v_1)^2 \quad (4.19)$$

$$\hat{R}_{,\lambda} = \hat{r}_{,u\lambda} = \frac{1}{2} \left\{ \hat{T}\hat{S} + \hat{r}\hat{S}_{,\lambda} + \hat{W}\hat{S}_{,\lambda} - 2\hat{R}\hat{S} - 1 + \hat{S}^2 + \frac{1}{2}\kappa\rho\hat{r}^2 + \Lambda\hat{r}^2 \right\} / \hat{r} \quad (4.20)$$

$$\hat{W}_{,\lambda} = \hat{T} \quad (4.21)$$

$$\hat{T}_{,\lambda} = \hat{W}_{,\lambda\lambda} = \frac{\hat{W}}{\hat{r}}\hat{S}_{,\lambda} + 4\hat{R}_{,\lambda} + 2\kappa \left( v_0v_1\rho - \frac{1}{2}\rho \right) \hat{r} - 2\Lambda\hat{r} \quad (4.22)$$

with:  $\hat{r}(0) = \hat{W}(0) = \hat{R}(0) = \hat{T}(0) = 0$  and  $\hat{S}(0) = 1$ .

These equations can be solved using standard ODE methods for systems of equations where (4.18) and (4.19) are solved as one system and (4.20), (4.21) and (4.22) are solved as a separate system. The evolution of the system follows from the energy-momentum equations (3.45), (3.43) and (3.44), repeated here in the order in which they will be solved as

$$v_0 = \frac{1}{2} \left( 1 + \frac{\hat{W}}{\hat{r}} \right) v_1 + \frac{1}{2} v_1^{-1} \quad (4.23)$$

$$v_{1,u} = \frac{1}{v_1} \left\{ \left( \left( 1 + \frac{\hat{W}}{\hat{r}} \right) v_1 - v_0 \right) v_{1,\lambda} + \frac{1}{2}(v_1)^2 \left( \frac{\hat{W}_{,\lambda}}{\hat{r}} - \frac{\hat{W}\hat{r}_{,\lambda}}{\hat{r}^2} \right) \right\} \quad (4.24)$$

$$\begin{aligned} \rho_{,u} = \frac{1}{v_1} \left\{ \rho \left[ \left( 1 + \frac{\hat{W}}{\hat{r}} \right) \left( \frac{2v_1}{\hat{r}}\hat{r}_{,\lambda} + v_{1,\lambda} \right) - \left( \frac{2v_0}{\hat{r}}\hat{r}_{,\lambda} + v_{0,\lambda} \right) + \left( \frac{\hat{W}_{,\lambda}}{\hat{r}} - \frac{\hat{W}\hat{r}_{,\lambda}}{\hat{r}^2} \right) v_1 - \left( \frac{2\hat{r}_{,u}}{\hat{r}} \right) v_1 \right] \right. \\ \left. + \rho_{,\lambda} \left( \left( 1 + \frac{\hat{W}}{\hat{r}} \right) v_1 - v_0 \right) - \rho v_{1,u} \right\}. \quad (4.25) \end{aligned}$$

Treating the solution of equations (4.18 and 4.19) and (4.20 - 4.22) conceptually as a single steps, the system forms a hierarchy, which can be solved using the following procedure:

- i. Calculate  $r_\lambda$  using the initial values of  $r$ ,  $\rho$  and  $v_1$  with (4.18) and (4.19).
- ii. Calculate  $W$  and  $r_{,u}$  using  $r$ ,  $v_0$  (from (4.23)),  $v_1$ ,  $\rho$  and  $\Lambda$  with (4.18-4.22). This step requires iteration between these equations.
- iii. Calculate  $v_0$  using  $v_1$ , and  $W$  with (4.23).
- vi. Calculate  $v_1$  for the next time step using  $W$  and  $v_0$  with (4.24).
- v. Calculate  $\rho$  for the next time step using  $\rho$ ,  $v_0$ ,  $v_1$ ,  $r_{,u}$  and  $W$  with (4.25).

This procedure applied to the above equations provides a system that can be solved with the scheme described in Section 4.1. The practical and theoretical aspects of the grid definition and conditions at the  $\lambda$ -boundaries also follow a pattern very similar to that of the Bondi-Sachs CIVP.

## 4.2.2 Domain of calculation

The discretisation strategy followed is based on a rectangular grid similar to the one used in Section 4.1 but using  $\lambda$  as the radial coordinate. As illustrated in Figure 4.3,  $\lambda$  does not reach a maximum and the AH does not affect the calculation. Apart from not needing to take the

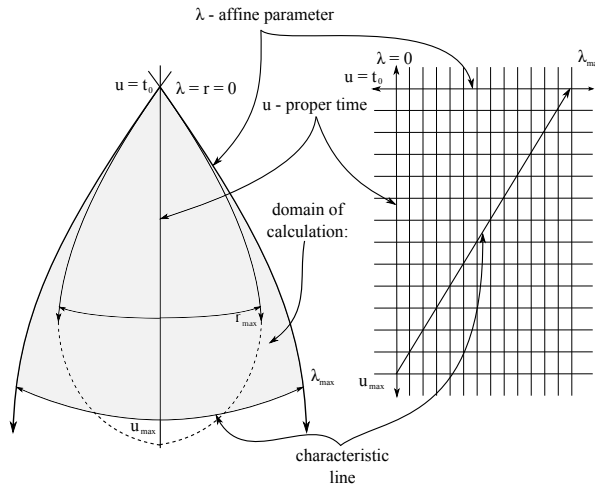


Figure 4.3: The past null cone calculated on a rectangular grid with an affine parameter ( $\lambda$ ) as the radial coordinate.

AH into consideration with  $\lambda$ , the limits and grid resolution are determined in the same way as the standard CIVP with  $\lambda$  replacing  $r$ .

## 4.2.3 Numerical scheme

### Hypersurface equations

Equation (4.6) is again implemented with the adaption to involve  $\lambda$ -grid points as

$$g_j^i = g_{j-1}^i + \frac{\Delta\lambda}{2} [(g,r)_j^i + (g,r)_{j-1}^i]. \quad (4.26)$$

Here,  $g$  represents  $\hat{r}$ ,  $\hat{S}$ ,  $\hat{R}$ ,  $\hat{W}$  or  $\hat{T}$  and  $g,r$  the left-hand sides of equations (4.18) to (4.22). As with the Bondi-Sachs CIVP,  $i$  is notated as the discrete time step and  $j$  the discrete radial step.  $(g,r)_j^i$  is calculated by substituting the values of the calculated hypersurface variables,  $v_1$  and  $\rho$  of the most recent iteration into equations (4.18) and (4.21), starting with the known initial values.

## Evolution equations

In order to solve the evolution equations, (4.24) and (4.25), their general form is the same as (4.7)

$$v_{1,u} = F_{v1} \quad \text{and} \quad \rho_{,u} = F_{\rho} \quad (4.27)$$

with

$$F_{v1} = \frac{1}{v_1} \left\{ \left( \left( 1 + \frac{\hat{W}}{\hat{r}} \right) v_1 - v_0 \right) v_{1,\lambda} + \frac{1}{2} (v_1)^2 \left( \frac{\hat{W}_{,\lambda}}{\hat{r}} - \frac{\hat{W} \hat{r}_{,\lambda}}{\hat{r}^2} \right) \right\} \quad (4.28)$$

$$F_{\rho} = \frac{1}{v_1} \left\{ \rho \left[ \left( 1 + \frac{\hat{W}}{\hat{r}} \right) \left( \frac{2v_1}{\hat{r}} \hat{r}_{,\lambda} + v_{1,\lambda} \right) - \left( \frac{2v_0}{\hat{r}} \hat{r}_{,\lambda} + v_{0,\lambda} \right) + \left( \frac{\hat{W}_{,\lambda}}{\hat{r}} - \frac{\hat{W} \hat{r}_{,\lambda}}{\hat{r}^2} \right) v_1 - \left( \frac{2\hat{r}_{,u}}{\hat{r}} \right) v_1 \right] + \rho_{,\lambda} \left( \left( 1 + \frac{\hat{W}}{\hat{r}} \right) v_1 - v_0 \right) - \rho v_{1,u} \right\} \quad (4.29)$$

and as explicit finite differences on a time half step they are written as

$$v_{1j}^{n+1} = v_{1j}^n + \Delta u F_{v1j}^{n+1/2} \quad \text{and} \quad \rho_j^{n+1} = \rho_j^n + \Delta u F_{\rho j}^{n+1/2}. \quad (4.30)$$

With,  $n$  a time iterator that will approach  $i$ . In these equations, the numerical values at the point  $(i, j)$  are used to evaluate the matter terms and hypersurface derivatives. The procedures described in Section 4.1.3 can then be applied to calculate the evolution of the affine CIVP.

## Algorithm

With some adaption for more hypersurface equations, the algorithm for the affine CIVP is essentially the same as that of the Bondi-Sachs CIVP. Again, after setting up a suitable grid, the numerical algorithm, based on Figure 4.2, iterates through the following steps:

- i. Set the  $\rho$  and  $v_1$  initial values on to the initial grid points. These values will, in principle, be obtained from observations.
- ii. Calculate  $\hat{r}$ ,  $\hat{r}_{,u}$ ,  $\hat{W}$  and  $v_0$  from  $\rho$  and  $v_1$  on the initial null cone using (4.18-4.22).
- iii. Calculate  $F_j^n$ , with  $n = 1$  for the initial step, from the values of  $v_1$ ,  $\rho$ ,  $\hat{r}$ ,  $\hat{r}_{,u}$ ,  $\hat{W}$  and  $v_0$  using (4.27).
- iv. Set  $F_j^{n+1/2} = F_j^n$ , again  $n = 1$  for the initial step, and calculate  $v_1$  and  $\rho$  as an initial approximation that will approach the actual values with subsequent iterations using (4.30).
- v. Use the new values of  $v_1$  and  $\rho$  to calculate  $\hat{r}$ ,  $\hat{r}_{,u}$ ,  $\hat{W}$  and  $v_0$  and their radial derivatives similar to (ii).
- vi. Calculate  $F_j^{n+1/2} = 1/2 (F_j^n + F_j^{n+1})$  from values in (v) and again  $v_1$  and  $\rho$  for  $F_j^{n+1}$  and the values in (iii) for  $F_j^n$ .

- vii. Test the calculations in (vi) for accuracy and convergence. If they are sufficiently accurate, move to the next time step, otherwise repeat steps v. and vi. with the new values of  $v_1$  and  $\rho$ .

#### 4.2.4 Boundary regions

As with the Bondi-Sachs CIVP, described in Section 4.1, calculations in the regions around  $\lambda = 0$  require special consideration because of  $\hat{r}$  denominators in equations (4.24) and (4.25), causing coordinate singularities. The mechanisms used in Section 4.1.4 for these regions was directly adapted for the affine CIVP model. Thereby, the region  $\lambda \approx 0$  is calculated using second order series expansions and the region where the series solution merges with the CIVP solution, blending functions (4.12 and 4.13) were used to obtain a stable merger region.

### 4.3 Conclusion

This chapter described the development of a numerical scheme for solving the Bondi-Sachs and affine CIVP models. The scheme is an adaption for cosmology of the developments for 3D modelling of gravitational waves in [10] and [11]. The numerical representation of the CIVP models is a second order explicit scheme, where the hypersurface equations are solved on the surface of a particular PNC. The resulting values are then substituted into the energy-momentum equations, which are then used to propagate the solution to a PNC in the history of the model's evolution.

The energy-momentum equations, however, contain coordinate singularities at the null cone vertices, a region excluded from calculations for gravitational wave modelling. For cosmology, the cone vertices are of particular interest since they represent the positions of observers. Since the model is not directly suitable in this region, series expansions of the CIVP equations have to be used for the region at and around the observer.

The outer radial boundary of the model is evolved without constraints but since the purpose of the model is to represent the verifiable region of a cosmological observer, the region is restricted by an incoming characteristic connected to the outer radial limit of the observer's PNC. Strictly speaking, then, the domain of calculation (Figures 4.1 and 4.3) only represents the causally connected region of a local observer.

The numerical scheme, as illustrated in Figure 4.2, is conceptually the same for the Bondi-Sachs and affine CIVPs using their respective sets of hypersurface and evolution equations. This can be summarised in following steps: <sup>1</sup>

- i. Set the initial values of  $v_1$  and  $\rho$  on the initial null cone.
- ii. Calculate the hypersurface equations, (4.1&4.2;4.18-4.22), using (4.6).
- iii. Calculate  $v_0$  using (4.3;4.23).
- iv. Calculate the inner region of  $v_1$  using the series expansion of (4.8;4.24).

---

<sup>1</sup>The equations in brackets refer to the standard CIVP equations followed by a semi-colon and the affine CIVP equations i.e. (standard eq.; affine eq.)

- v. Solve the rest of  $v_1$  with (4.8;4.24).
- vi. Solve the inner region of  $\rho$  using the series expansion of (4.9;4.25).
- vii. Solve the rest of  $\rho$  with (4.9;4.25).
- viii. Repeat steps ii to vii until sufficiently accurate and then proceed to the next time step.
- ix. Calculate the outer boundary cut-off line using (4.17) and then discard the calculations beyond this line.

In Chapter 5, accuracy and stability of the code will be evaluated using known solutions transformed to null coordinates. Having established that the code is sufficiently accurate and stable, the model will then be used to perform numerical experiments to compare the evolution of different models given initial values from identical observations. In particular, the ambiguity of LTB universes against observations that seem to favour the  $\Lambda$ CDM model is used to compare the historical behaviour of different models.

# Chapter 5

## Numerical calculations

The objective of this chapter is to demonstrate that the CIVP code, described in Chapter 4, is second order convergent and stable. In order to do this, a verification framework is defined, which will be used for various verification cases. The coordinate transformations, described in Chapter 3, will be used here to provide known solutions in null coordinates for the test cases. Having shown that the models are stable and convergent, two numerical experiments are performed with the code where the LTB model is evolved from the initial data of a  $\Lambda$ CDM model. This represents the effect where observations are regarded as model independent and different models are evaluated against the same observations. This is a particularly interesting application of the code.

### 5.1 Verification framework

The objective of the developments in this thesis is to produce a mathematical model of the observable universe which is well suited for numerical modelling. For the numerical model, it has further been the intention that the model should be second order convergent. A verification framework is defined here to systematically explore the code's ability of realising these requirements. The fundamental properties of numerical convergence for initial value PDEs are related to: the well-posedness of the mathematical model and the consistency and stability of the finite difference approximation. The definitions of these properties are [2] (pp. 46–49):

- *Well-posedness*: an initial value problem is well-posed if the solution exists, is unique and is stable subjected to small perturbations.
- *Consistency condition*: a finite difference representation is consistent if it can be shown that the difference between the PDE and its difference representation vanish as the grid is refined. Effectively this means that the truncation error becomes zero as the grid size approaches zero.
- *Stability*: a stable numerical scheme is one for which any source of errors (truncation errors, round-off errors or incorrect data) are not permitted to grow exponentially in the sequence of numerical calculations from one time step to another. In practice, the

bounds of error amplification will be determined by the precision required for a particular calculation.

- *Convergence*: the solution of the finite difference scheme approaches the solution of the PDE when the grid is refined.

For linear initial value PDEs the relation between these properties is formal and stated as [57]:

**Theorem 6 (Lax’s equivalence theorem)** *Given a properly posed<sup>1</sup> initial value problem and a finite-difference approximation to it that satisfies the consistency condition, stability is the necessary and sufficient condition for convergence.*

For nonlinear PDEs, no formal proof of this theorem has been established and exact analyses of the properties for non-trivial problems, such as the CIVPs considered here, are well beyond the scope of the current work. Even so, while convergence for the CIVPs does not strictly follow from Theorem 6, it is unlikely to follow if these conditions are not met by the model or its constituent parts. With this in mind, the elements of the theorem are considered in the selection of verification models while the dynamic behaviour of the code is explored through test runs where the stability and convergence are analysed. The consistency condition will not be considered explicitly and therefore no attempt will be made to distinguish the effects of truncation errors in the difference formulae from other errors and effects in the numerical scheme.

### 5.1.1 Verification models

In Theorem 6, the first prerequisite is that the initial value problem should be well-posed. The well-posedness of CIVPs in General Relativity is, however, a difficult unresolved problem and it is therefore conducive to restrict verification cases to simple models that are easy to analyse. The models that were chosen are the simplest of the classes they represent, they are well represented in literature and they are simple enough that if doubts should arise about their well-posedness, problems should be detectable without exact analyses. Three cosmologies representing homogeneous, inhomogeneous and the presence of a cosmological constant have been chosen as verification models: the EdS model as a homogeneous model, bang-time LTB model as an inhomogeneous model and the  $\Lambda$ CDM model, to investigate the effect of a cosmological constant. The introduction of these models in Sections 2.2.3, 2.2.2 and 2.2.1, and the coordinates transformations, presented in Sections 3.1.4 and 3.2.4 will be applied here to provide known solutions against which the numerical calculations can be compared. The process of comparing calculated against transformed results is to use the transformed values on the initial null cone as input to the code. The code is then evolved from these values and compared against the corresponding transformed results. All calculations were done on a regularly spaced grid as described in Sections 4.1.2 and 4.3.

#### Einstein-de Sitter model

The EdS model is the simplest expanding universe model and its solution and null cone transformations are analytically known for the Bondi-Sachs CIVP (see Sections 2.2.3 and 3.1.4 and

---

<sup>1</sup>The terms properly posed and well-posed will be used interchangeably in the discussions that follow.

references [37] and [12]) while for the affine CIVP, the transformation requires a simple numerical solution (Section 3.2.4). As further reference, the EdS model as a Bondi-Sachs CIVP has also been studied numerically in [12] using an axisymmetric code without rotation. A further benefit is that the LTB and  $\Lambda$ CDM models reduce to the EdS model with the selection of certain parameter values and it is, therefore, also a useful baseline to measure the accuracy of the transformation methods (described in Chapter 3) when the transformed solutions of LTB and  $\Lambda$ CDM models are calculated.

### LTB model

For inhomogeneous verification, LTB models of the bang-time type, as described in Section 2.2.2, are implemented using a linear bang-time function on which the slope of the line can be adjusted to represent specific universes. The function is

$$t_B(r) = br, \quad (5.1)$$

with  $b$  being a constant on a specific universe. This simplifies equations (2.43), (2.44) and (2.45) to

$$\begin{aligned} R(t, r) &= r(t - br)^{2/3}, \quad R_{,r}(t, r) = -\frac{1}{3} \frac{(-3t + 5br)}{(t - br)^{1/3}} \quad \text{and} \\ \rho(t, r) &= \frac{1}{2\pi(t - br)(3t - 5br)}. \end{aligned} \quad (5.2)$$

These equations are substituted into the parabolic LTB metric (2.31) and transformed using equations (3.22) and (3.26) for the Bondi-Sachs CIVP and equations (3.63) and (3.64) for the affine CIVP to obtain null cone transformed data.

### $\Lambda$ CDM model

The  $\Lambda$ CDM is used to test the code on models with a non-zero cosmological constant ( $\Lambda$ ). Since the Bondi-Sachs model does not include  $\Lambda$ , these tests are only relevant for the affine CIVP. Equations (2.27–2.29) in Section 2.2.1 describe the model. These equations are transformed to null coordinates with the method described in Section 3.2.4 using LTB transformations with  $R(t, r) = a(t)r$ . As discussed in Section 2.2.1, values representative of the actual Universe are  $\{H_0, \Omega_k, \Omega_{m0}, \Omega_\Lambda\} = \{72 \text{ Mpc s}^{-1} \text{ km}^{-1}, 0, 0.3, 0.7\}$ . However, for the purpose of code verification the model is simplified by using geometric units ( $G = 1$  and  $c = 1$ ) and time is scaled to  $t_0 = 1$  using a value of  $H_0 = 0.964$ .

### 5.1.2 General comments on models

The specific models that were taken as verification cases are models that are simple to analyse but also physically realistic. For verification purposes, the time coordinate has been scaled to  $t_0 = 1$  for all models. Although this obscures the differences in the ages of the models, which is crucial in interpreting the actual Universe, the emphasis here is on comparing calculation errors not in realistic modelling. The models with their parameter values are summarised in Table 5.1.

Model	$b$	$\Lambda$	Description
EdS	0	0	Baseline model
LTB	-0.5	0	Representing the shape of the $\Lambda$ CDM
$\Lambda$ CDM	0	0.7	The accepted standard cosmological model

Table 5.1: Summary of verification models for evaluating accuracy and stability.

The effect of different values of the bang-time constant ( $b$ ) of the LTB model on the shape of the PNC is shown in Figure 5.1 where different models have been scaled and transposed relative to an observer located at the vertex of the PNC of a normalised EdS universe. The value  $b = 0$  is exactly the EdS model and  $b > 0$  shifts the age of a universe to a younger age as  $r$  increases while  $b < 0$  provides the opposite effect where a universe is shifted to an older age as  $r$  increases. The latter case is particularly interesting since it provides a mechanism to mimic a cosmological constant [21]. In Figure 5.1 a reasonable match on the shape of the  $\Lambda$ CDM ( $\Omega_\Lambda = 0.7$ ) PNC is shown by a  $b = -0.5$  bang time model before the PNC refocusses. This is however not an exact physical match but provides a useful verification model since the shape of the null cone is a critical aspect on the stability of a CIVP code. For the  $\Lambda$ CDM model, setting  $\Lambda = 0$  will also correspond to the EdS model and therefore also to the LTB ( $b = 0$ ).

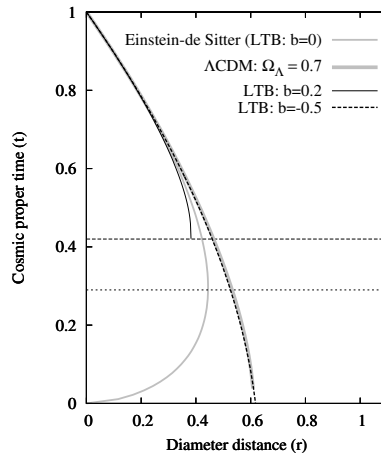


Figure 5.1: The past null cone of the bang time models compared to the Einstein-de Sitter model and the  $\Lambda$ CDM model.

It should also be noted that although the LTB model was specifically selected to represent the effects of inhomogeneities, in general, null cones are not hypersurfaces of homogeneity (see [81]) even for homogeneous spacetimes such as the EdS and  $\Lambda$ CDM models.

### 5.1.3 Methodology

The framework for evaluating the test cases will take as guideline the stability and convergence properties of Lax's theorem. This will be evaluated under the following topics:

i. *Model comparison*

The initial test is to explore how well the numerical solution follows the known values for the test models and to determine the extent of the region where the code is apparently stable by:

- Evaluating  $\rho$ ,  $v_1$  and  $r$  on historical PNCs back to the youngest stable PNC. This is of interest to evaluate the physical consistency of the model.
- The stability limits of model variables ( $\rho$ ,  $v_1$  and  $r$ ) for both  $u$  and the radial distance<sup>2</sup>( $r$  or  $\lambda$ ). This is done by starting from the position half way to the AH and then gradually increasing  $u$  and  $r$  or  $\lambda$  until the code becomes unstable.

These tests are presented for all the test models for both the Bondi-Sachs and affine CIVPs.

ii. *Convergence*

The details of the propagation of errors and how it is affected by increasing the grid resolution is considered in this test by:

- Evaluating the error distribution of the calculated density ( $\rho$ ) compared to that of known solutions. The density is a useful measure for this since it was found that errors in the other variables become amplified in the density calculation.
- Evaluating the convergence of the calculations when the grid resolution is refined to measure a code's order of convergence.

These tests are presented for all the test models for both the Bondi-Sachs and affine CIVPs.

iii. *Sensitivity to errors*

Here, it will be explored how input errors affect the error propagations of the calculations by:

- Inducing constant, cyclic and random errors into the input data and then comparing the initial error sizes to those in the output variables.
- For the cyclic errors, it is presented how input errors in each input variable affect the individual output variables<sup>3</sup>. This is to determine the most sensitive input and output variables.

These tests are presented for calculations with the affine CIVP on the EdS model.

---

<sup>2</sup>In further discussions, the term *radial distance* ( $r$  or  $\lambda$ ) will refer to  $r$  for the Bondi-Sachs CIVP or  $\lambda$  for the affine CIVP.

<sup>3</sup>Although cyclic errors are not realistic input errors, their output effects were more pronounced than with the constant or random errors. Therefore, it provides a good test case to demonstrate.

## 5.2 Model comparison

The results of numerical calculations for the models described in Section 5.1 follow in this section. The historical evolutions from data on an initial PNC of the covariant velocity ( $v_1$ ) and the density ( $\rho$ ) are presented against the radial distance ( $r$  or  $\lambda$ ) for both CIVP models. In addition, the evolutions of the diameter distance ( $\hat{r}$ ) against the affine parameter ( $\lambda$ ) and the redshift ( $z$ ) are also shown for the affine CIVP. The latter shows the relation  $\hat{r}(z)$  which is of particular interest for observations since it provides an illustration of an observer's perception of distance from a particular PNC vertex.

In the results, the initial PNC values are indicated with  $u_0$ , the youngest PNC with  $u_{\max}$  and an intermediate PNC is shown at the midpoint age in between. As already mentioned, the purpose of the calculations is to test the behaviour of the numerical models and not the physics of the specific cosmologies, hence, time is scaled to  $u_0 = 1$  and geometrised units are used. Table 5.2 gives a summary of the test cases. The stability limits mentioned in point (i) of Section 5.1.3 is shown here as  $z_{\max}$  and  $u_{\max}$ . In all cases the numerical results (points in the figures) closely follow the transformed results (lines in the figures); an illustration of the model consistency, also related to point (i) in Section 5.1.3. In the figures,  $r$  will refer to the diameter distance in all cases and the distinction between  $r$  and  $\hat{r}$  is irrelevant.

Model	$z$ at $r_{\max}$	$z_{\max}$	$u_0$	$u_{\max}$	Figures
CIVP EdS	1.25	0.47	1	0.24	5.2
Affine EdS	1.25	4.5	1	0.35	5.4, 5.3
CIVP LTB ( $b = -0.5$ )	1.02	0.48	1	0.15	5.5
Affine LTB ( $b = -0.5$ )	1.02	1.2	1	0.2	5.7, 5.6
Affine $\Lambda$ CDM ( $\Omega_\Lambda = 0.7$ ) <sup>4</sup>	1.61	6	1	0.4	5.9, 5.8

Table 5.2: Affine CIVP test cases.

<sup>4</sup>This result is in agreement with that of [5].

### 5.2.1 Einstein-de Sitter: Bondi-Sachs CIVP

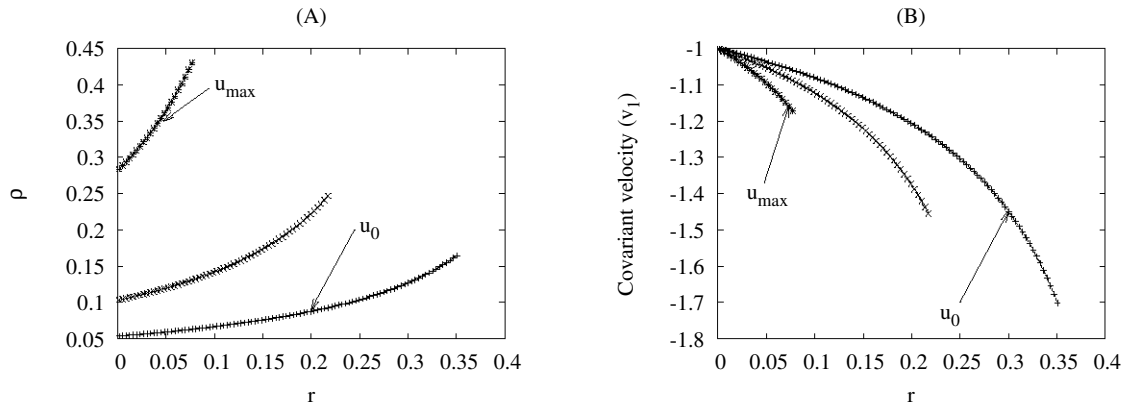


Figure 5.2: Density distribution (A) and covariant velocity (B) on PNCs at different proper times ( $u$ ) evolved from a local PNC up to  $z = 0.47$ .

## 5.2.2 Einstein-de Sitter: Affine CIVP

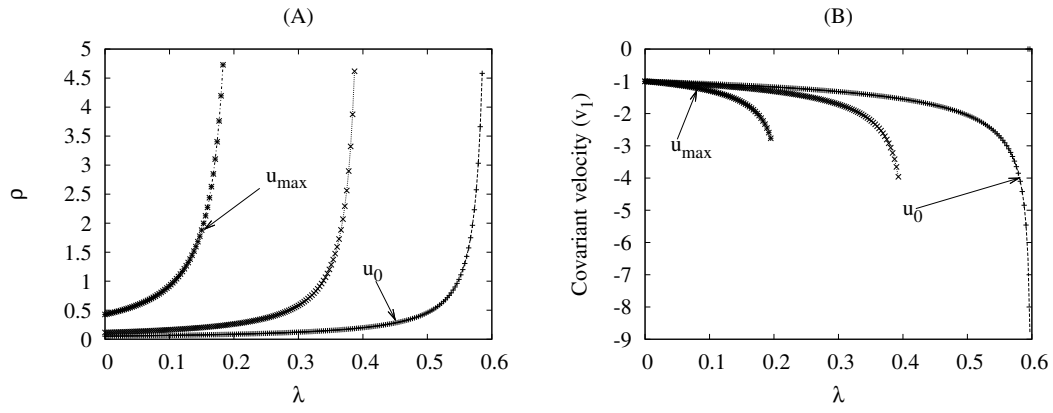


Figure 5.3: Density distribution (A) and covariant velocity (B) on PNCs at different proper times ( $u$ ) evolved from a local PNC up to  $z = 4.5$ .

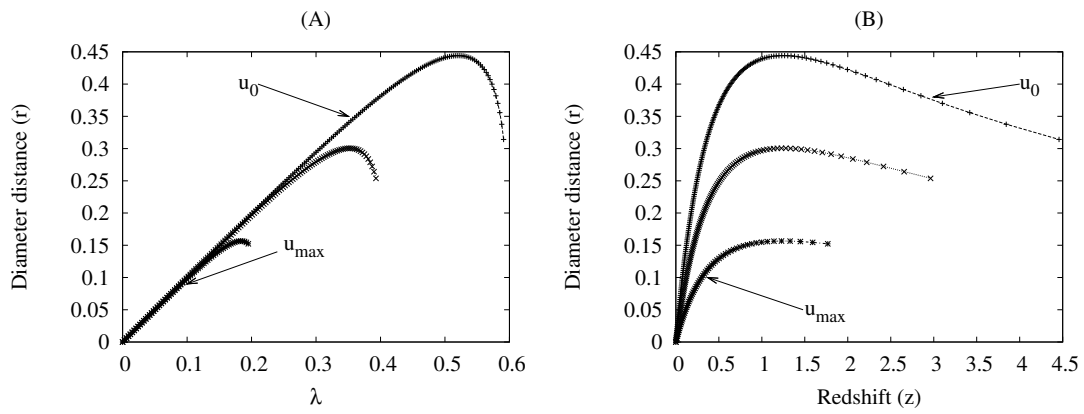


Figure 5.4: Diameter distance against  $\lambda$  (A) and against of  $z$  (B) on PNCs at different proper times ( $u$ ) evolved from a local PNC up to  $z = 4.5$ .

### 5.2.3 LTB model: Bondi-Sachs CIVP

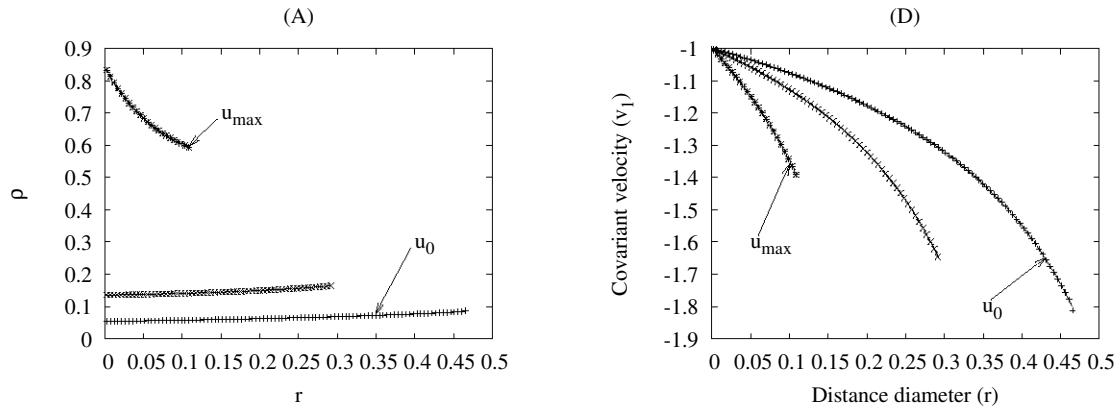


Figure 5.5: Density distribution (A) and covariant velocity (B) on PNCs at different proper times ( $u$ ) evolved from a local PNC up to  $z = 0.47$ .

### 5.2.4 LTB model: Affine CIVP

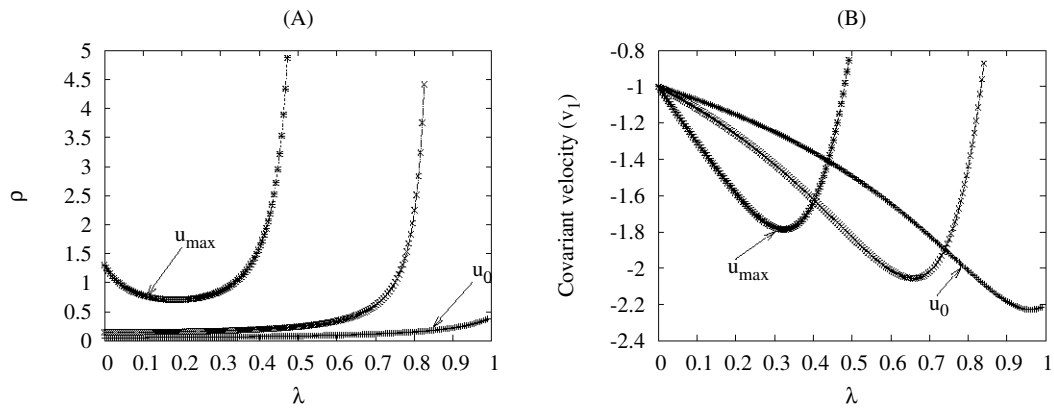


Figure 5.6: Density distribution (A) and covariant velocity (B) on PNCs at different proper times ( $u$ ) evolved from a local PNC up to  $z = 1.2$ .

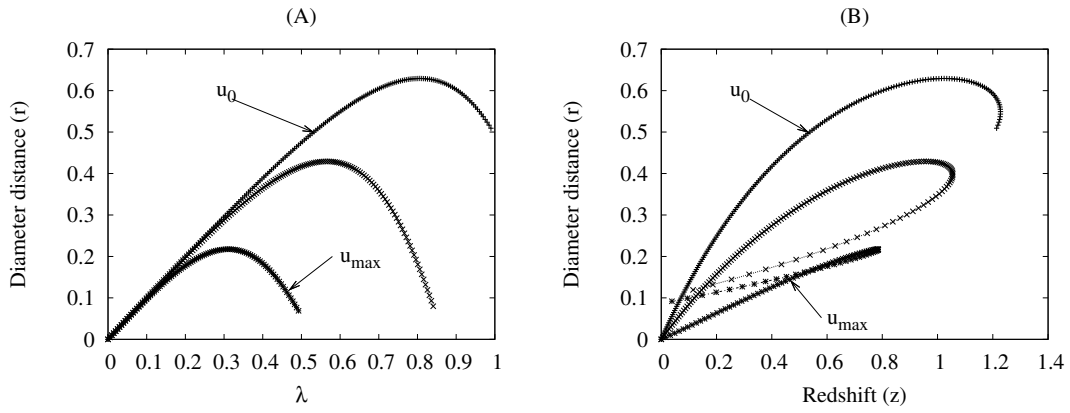


Figure 5.7: Diameter distance against  $\lambda$  (A) and against of  $z$  (B) on PNCs at different proper times ( $u$ ) evolved from a local PNC up to  $z = 1.2$ .

### 5.2.5 $\Lambda$ CDM with $\Omega_\Lambda = 0.7$

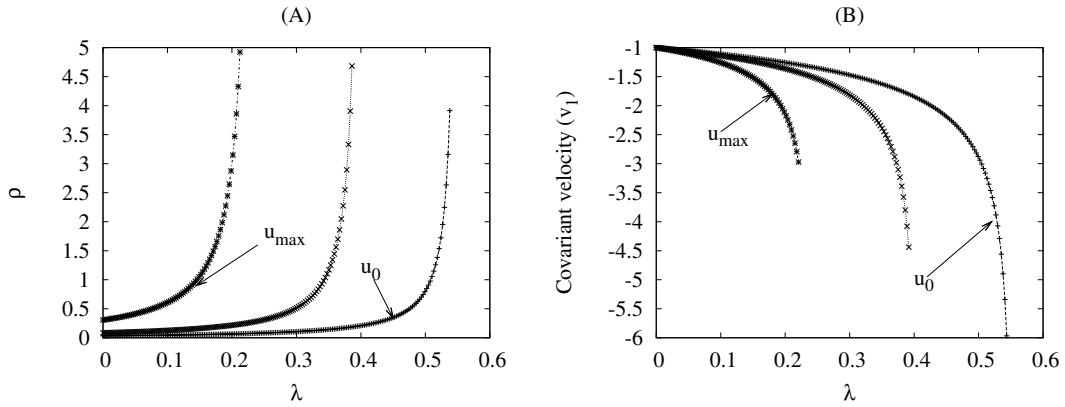


Figure 5.8: Density distribution (A) and covariant velocity (B) on PNCs at different proper times ( $u$ ) evolved from a local PNC up to  $z = 5$ .

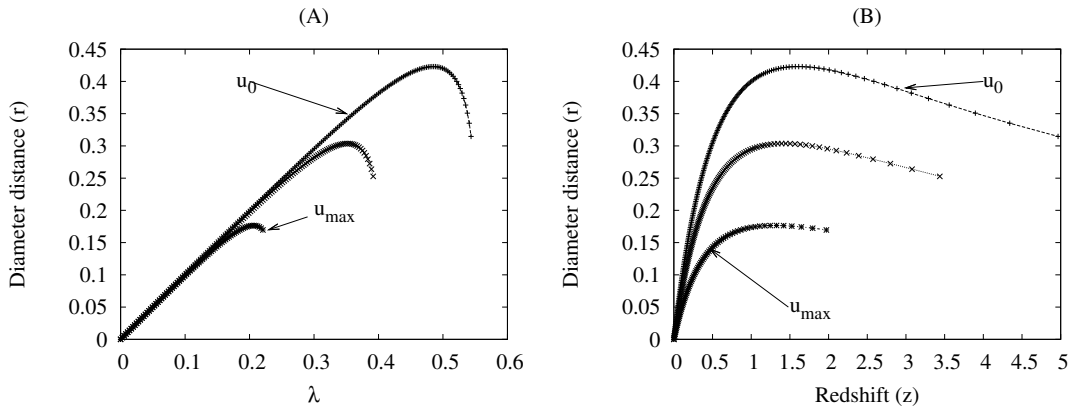


Figure 5.9: Diameter distance against  $\lambda$  (A) and against of  $z$  (B) on PNCs at different proper times ( $u$ ) evolved from a local PNC up to  $z = 5$ .

### 5.3 Convergence

This section presents the results related to point (ii) in Section 5.1.3 by comparing the error propagation for refinements on a regular grid. In the refinements, the spatial and temporal resolution were retained to a ratio of  $nu = 5nr$  where  $nr$  and  $nu$  are the number of radial and time grid points respectively. In Figure 5.10 (A and B) and Figure 5.11 (A, B and C), the relative errors for  $\rho$  on the oldest PNCs calculated is shown for the grid resolutions as indicated. In Figure 5.10 (C) and Figure 5.11 (D), the size in error against the grid spacing is shown on a log – log plot. The slopes of these lines indicate the order of convergence of the respective models. The objective was to obtain second order convergence and the respective values attained are indicated on the figures.

### 5.3.1 Bondi-Sachs CIVP

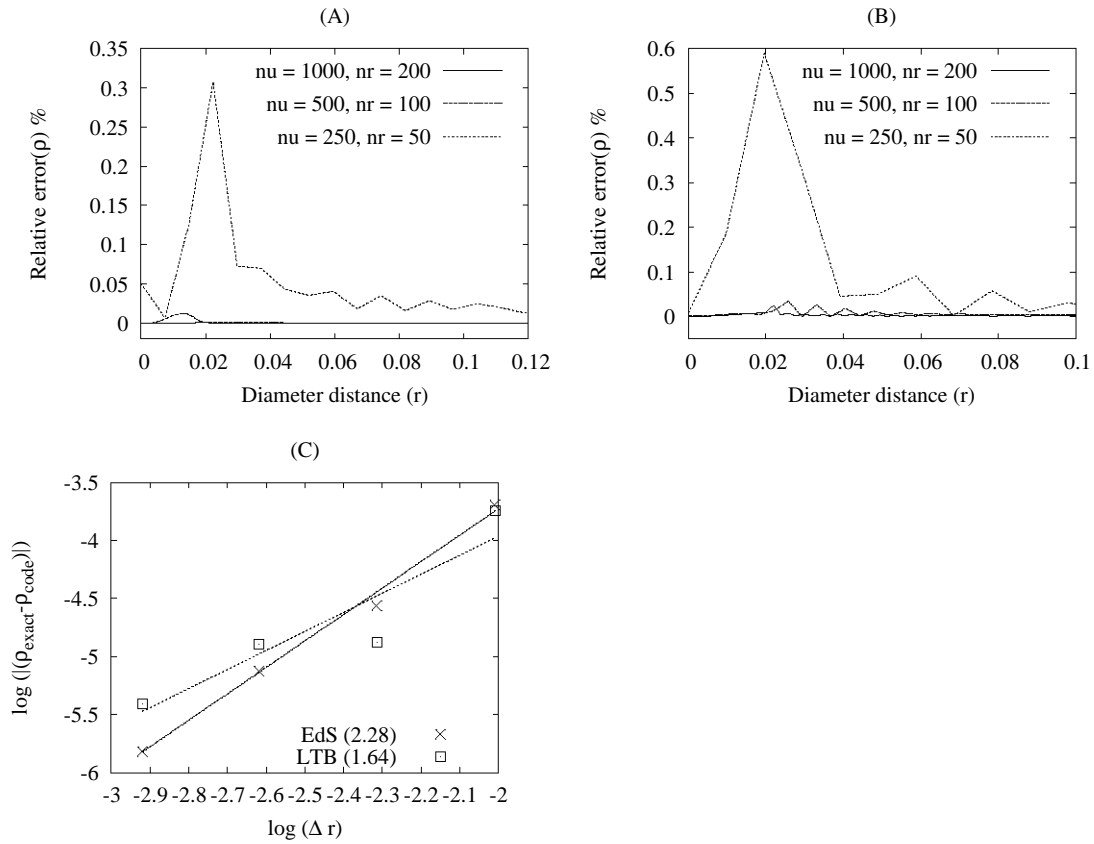


Figure 5.10: Radial error distribution on the youngest null cones for the Einstein-de Sitter ( $u_{max} = 0.24$ )(A) and LTB ( $u_{max} = 0.15$ )(B) models for different grid resolutions. In (C), the error against grid size is shown; the slope of the change in error represents the order of convergence and is indicated in brackets in the legend.

### 5.3.2 Affine CIVP

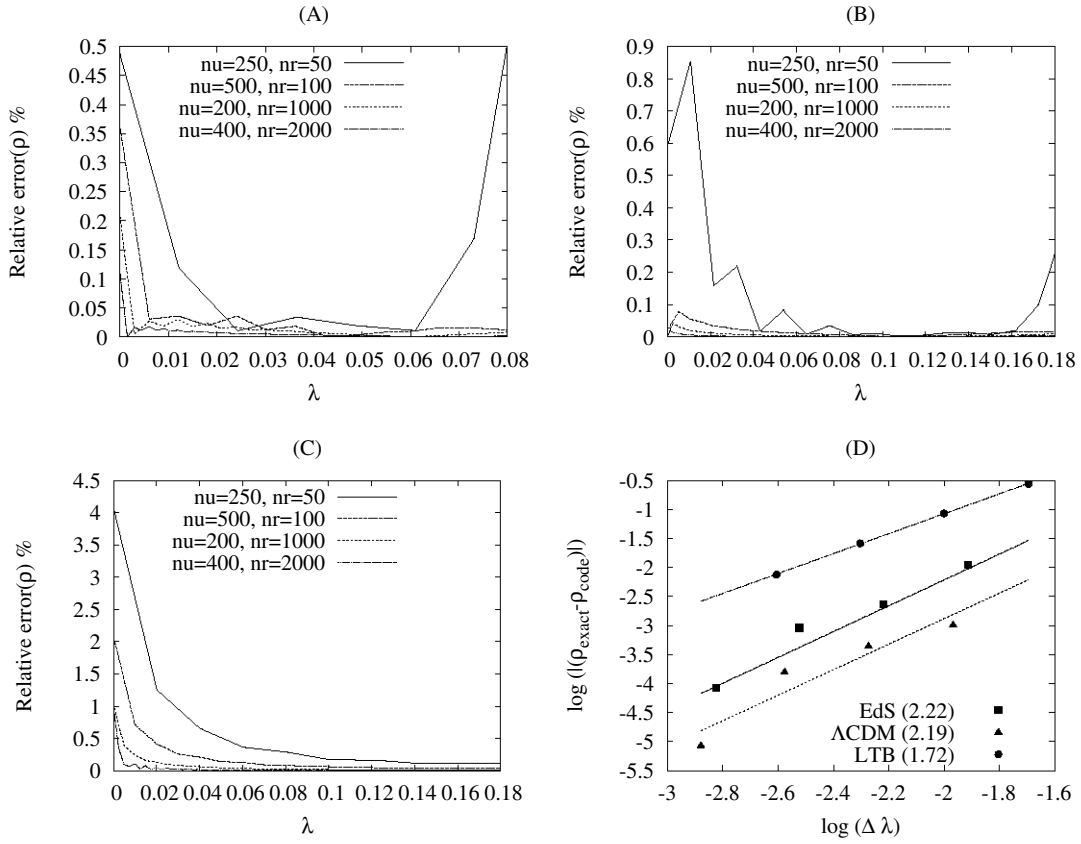


Figure 5.11: Radial error distribution on the youngest null cones for the Einstein-de Sitter ( $u_{max} = 0.35$ )(A),  $\Lambda$ CDM ( $u_{max} = 0.4$ )(B) and LTB ( $u_{max} = 0.2$ )(C) models for different grid resolutions. In (D), the error against grid size is shown; the slope of the change in error represents the order of convergence and is indicated in brackets in the legend.

## 5.4 Sensitivity to errors

The tests that follow address point (iii) in Section 5.1.3 by investigating the behaviour of the affine CIVP model when there are errors in the input data. This involves the introduction of known and also random errors into the initial data, which are then evaluated at the youngest PNC after the calculation. The introduction of constant errors can roughly be interpreted as systematic errors and the random errors as input noise or random observational errors although it is not the intention to model realistic data. The general concern here is to determine if input errors create artificial instabilities or damping effects in the numerical calculations and if an error band in input data can be interpreted as error bands in other variables from calculated data. A more specific concern is also to determine which are the most sensitive input and output variables. In the results that follow, the affine CIVP is used on the EdS model i.e. the calculations of Section 5.2.2 but with errors in the initial data.

### 5.4.1 Combined input errors

#### Combined constant errors

The combined effects of constant input errors in  $\hat{r}$ ,  $\rho$  and  $z$  at a relative value of 10% (Figure 5.13 (A)) are shown in Figures 5.13 (B), (C) and (D) after it was propagated over 500 time steps to the youngest PNC at  $u_{max} = 0.35$  for the EdS model.

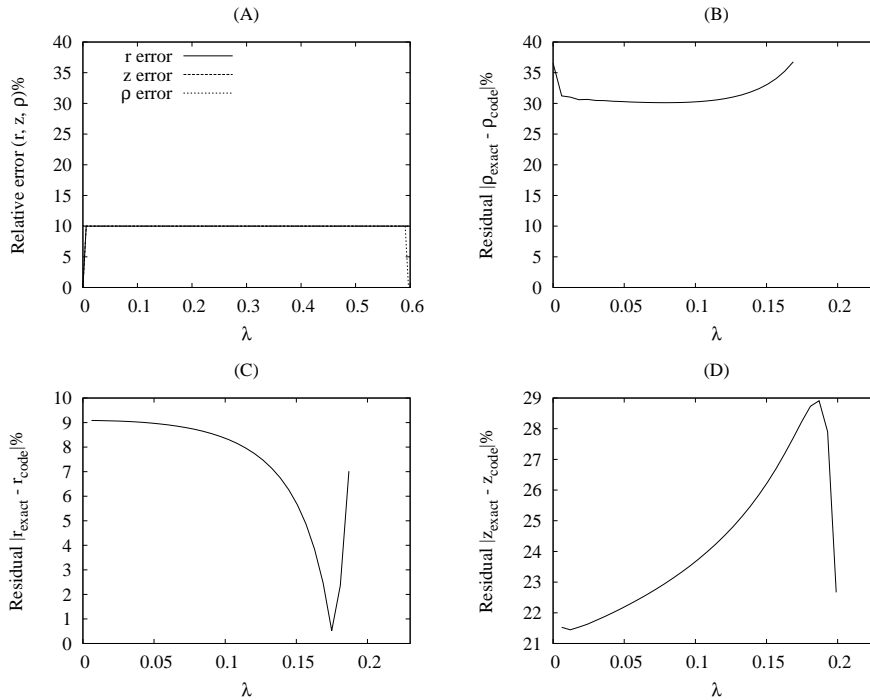


Figure 5.12: Error propagation of relative constant input errors in  $z$ ,  $\hat{r}$  and  $\rho$  with a value of 10% shown in (A). In (B), the output error on  $\rho$ , (C) the output error on  $\hat{r}$  and in (D) the output error on  $z$ .

### Combined cyclic errors

The combined effects of cyclic input errors in  $\hat{r}$  and  $\rho$  that have relative peaks of 10% and  $z$  with 1% (Figure 5.13 (A)) are shown in Figures 5.13 (B), (C) and (D) after it was propagated over 500 time steps to the youngest PNC at  $u_{max} = 0.35$  for the EdS model. The cyclic error is generated using  $g = g_{exact}(1 + (peak\%/100)\sin(20\pi(j/N_J)))$  where  $g$  represents  $\hat{r}$ ,  $\rho$  or  $z$ ;  $j$  is the radial grid index and  $N_J$  the number of grid points.

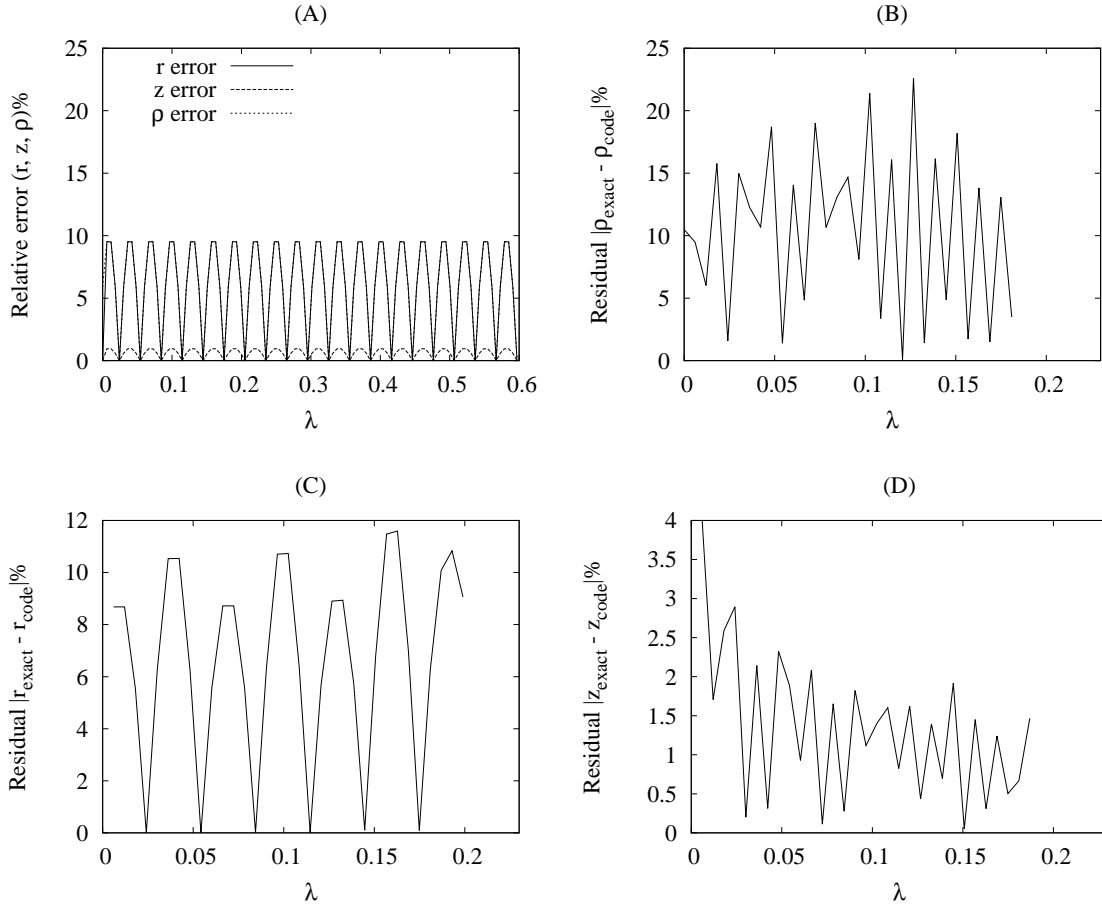


Figure 5.13: Error propagation of relative cyclic input errors in  $z$  with 1%,  $\hat{r}$  with 10% and  $\rho$  with 10% shown in (A). In (B), the output error on  $\rho$ , (C) the output error on  $\hat{r}$  and in (D) the output error on  $z$ .

### Random errors on $\rho$ , $z$ and $\hat{r}$

In this section, random errors, which follow a normal distributions, are induced into the input data. This is a more realistic representation of typical errors since it does not have cycles that repeat on the same frequency for all the variables, such as present in the sine input function. The sizes of the errors have relative peaks at  $\rho \approx 10\%$ ,  $z \approx 2\%$  and  $r \approx 10\%$ . Figure 5.14 (A) shows the input error and (B), (C) and (D), the output error after 500 time steps to the youngest PNC at  $u_{max} = 0.35$  for the EdS model.

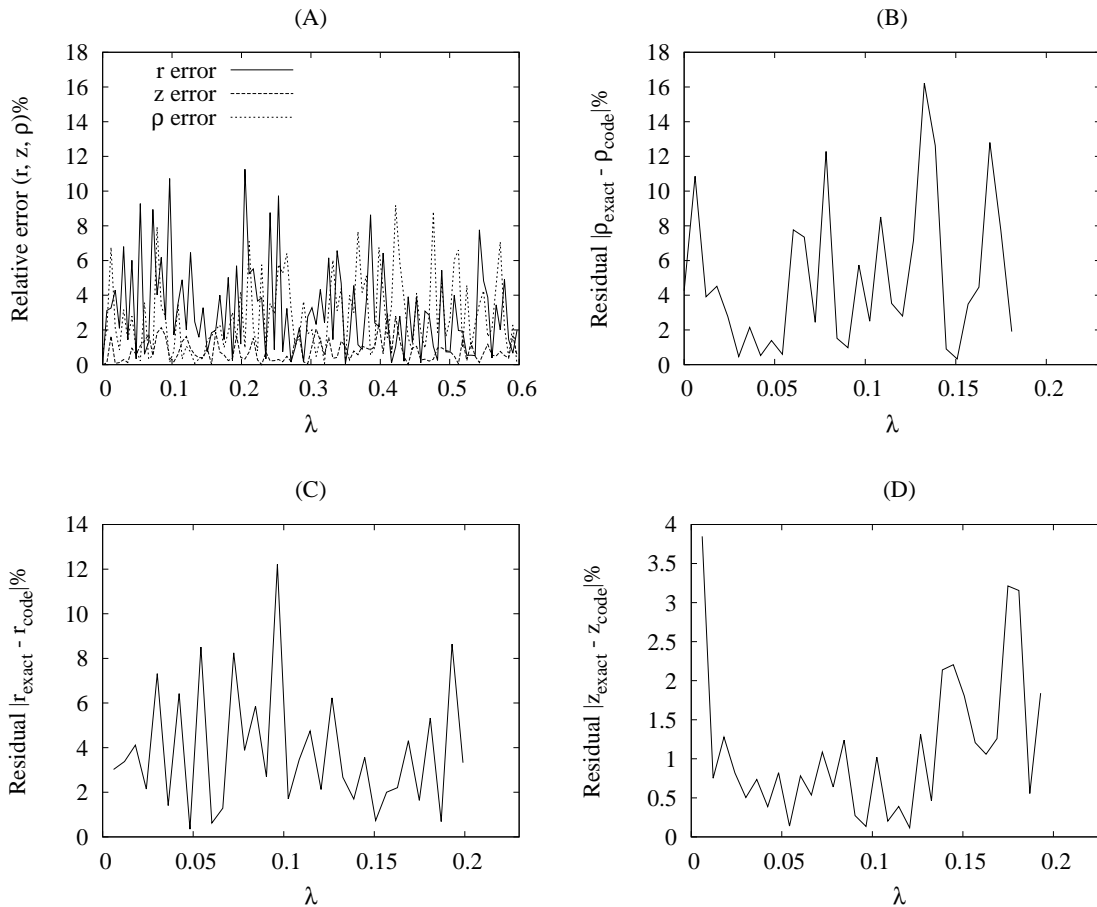


Figure 5.14: Error propagation of relative random input errors in  $z$  with peaks at 2% and  $\hat{r}$  and  $\rho$  with peaks at 10% shown in (A). In (B), the output error on  $\rho$ , (C) the output error on  $\hat{r}$  and in (D) the output error on  $z$ .

### 5.4.2 Individual input errors

In this section, the objective is to demonstrate the sensitivity of input errors in each individual input variable on each of the model variables. The intention is to determine the most sensitive input and output variables. From the cases that follow, it is identified that  $\rho$  is the most sensitive output variable and is particularly vulnerable to input errors in  $z$  (or  $v_1$ ). The results of the cyclic tests will be shown as a demonstration case since the effects of input errors were more prominent in these.

**Cyclic errors on  $r$  with  $r = r_{exact}(1 + 0.1 \sin(20\pi(j/N_J)))$**

The effects of a cyclic input error in  $\hat{r}$  that has a relative peak of 10% (Figure 5.15 (A)) are shown in Figures 5.15 (B), (C) and (D) after it was propagated over 500 time steps to the youngest PNC at  $u_{max} = 0.35$  for the EdS model.

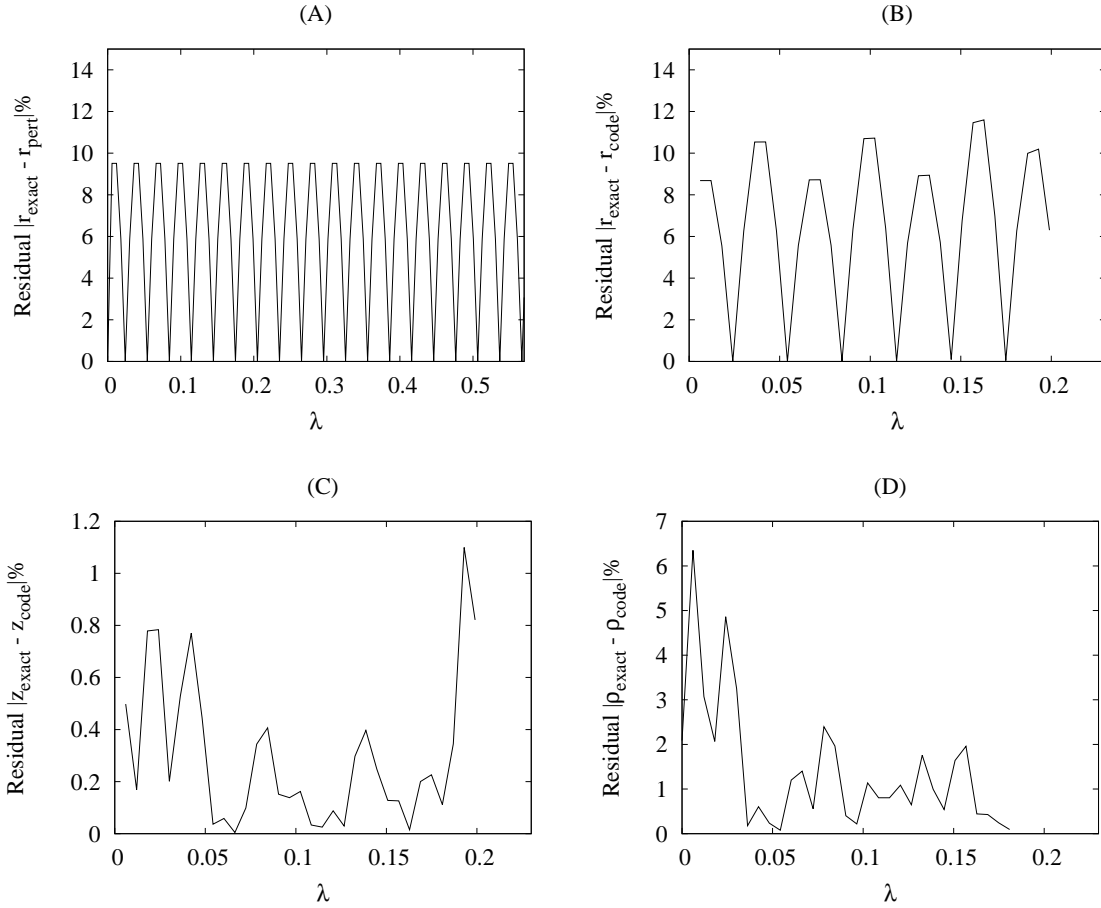


Figure 5.15: Error propagation of a 10% relative cyclic input error in  $\hat{r}$  shown in (A). In (B), the output error on  $\hat{r}$ , (C) the output error on  $z$  and in (D) the output error on  $\rho$ .

**Cyclic errors on  $\rho$  with  $\rho = \rho_{exact}(1 + 0.1 \sin(20\pi(j/N_J)))$**

The effects of a cyclic input error in  $\rho$  that has a relative peak of 10% (Figure 5.16 (A)) are shown in Figures 5.16 (B), (C) and (D) after it was propagated over 500 time steps to the youngest PNC at  $u_{max} = 0.35$  for the EdS model.

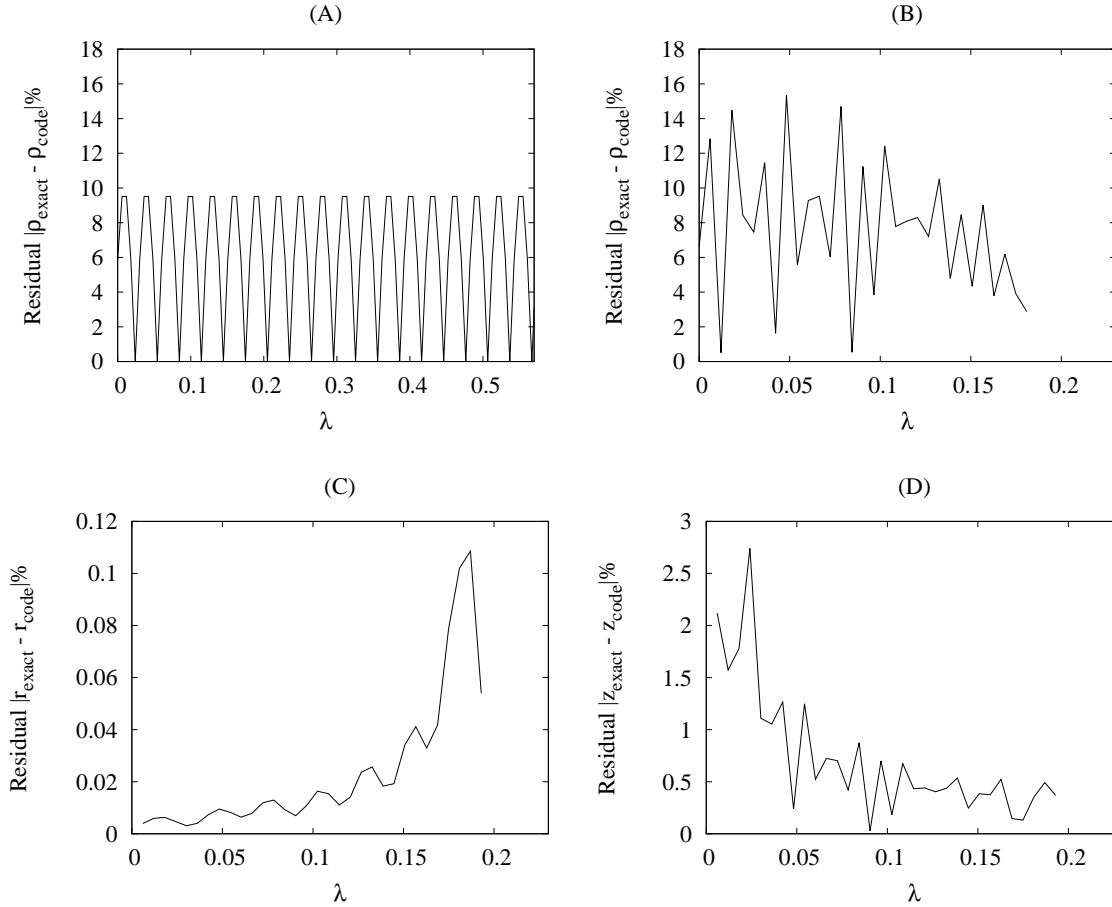


Figure 5.16: Error propagation of a 10% relative cyclic input error in  $\rho$  shown in (A). In (B), the output error on  $\rho$ , (C) the output error on  $r$  and in (D) the output error on  $z$ .

**Cyclic errors on  $z$  with  $z = z_{exact}(1 + 0.01 \sin(20\pi(j/N_J)))$**

The effects of a cyclic input error in  $z$  that has a relative peak of 1% (Figure 5.17 (A)) are shown in Figures 5.17 (B), (C) and (D) after it was propagated over 500 time steps to the youngest PNC at  $u_{max} = 0.35$  for the EdS model.

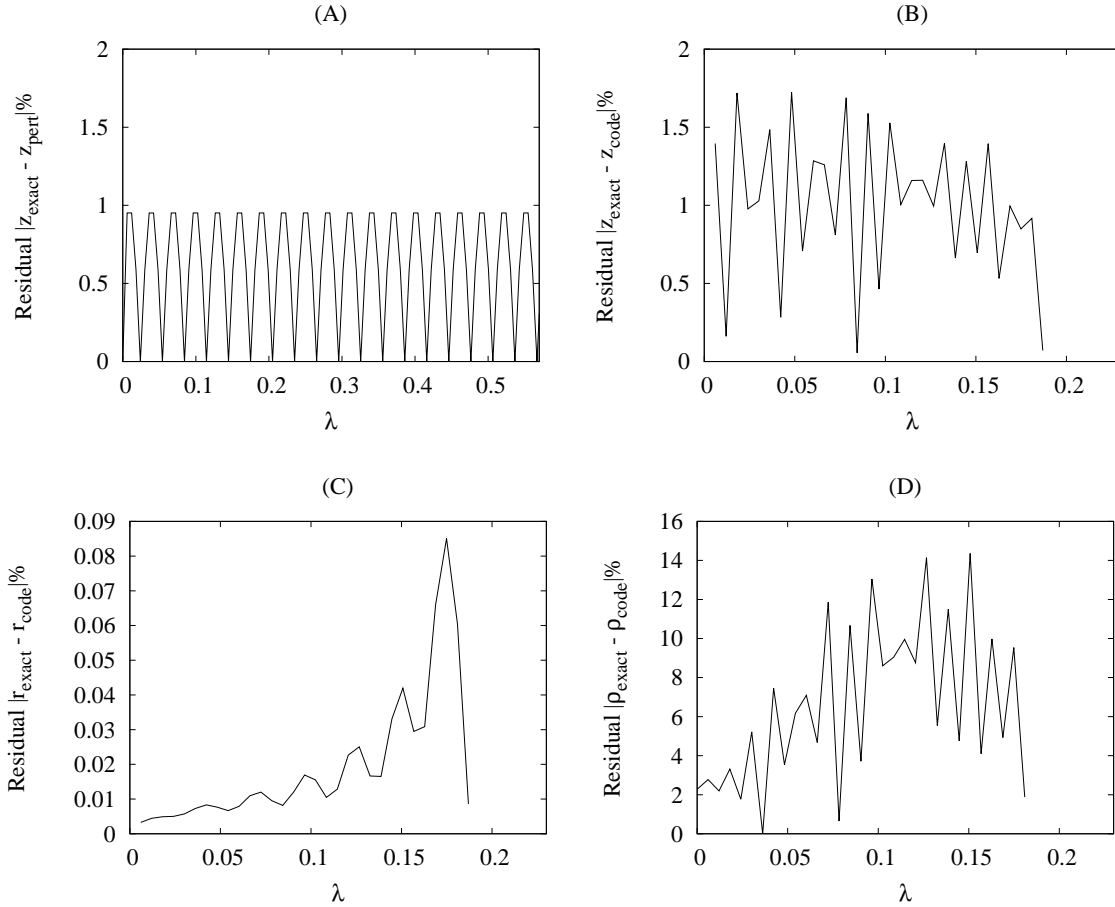


Figure 5.17: Error propagation of a 1% relative cyclic input error in  $z$  shown in (A). In (B), the output error on  $z$ , (C) the output error on  $\hat{r}$  and in (D) the output error on  $\rho$ .

**Cyclic errors on  $z$  with  $z = z_{exact}(1 + 0.03 \sin(20\pi(j/N_J)))$**

In the previous calculation, the output errors distribution of  $\rho$  is significantly higher than the output errors in the other variables. This effect is further demonstrated by repeating the calculation but adjusting the error in  $z$  to a relative peak of 3% (Figure 5.18 (A)). Figures 5.18 (B), (C) and (D) again show the output after it was propagated over 500 time steps to the youngest PNC at  $u_{max} = 0.35$  for the EdS model.

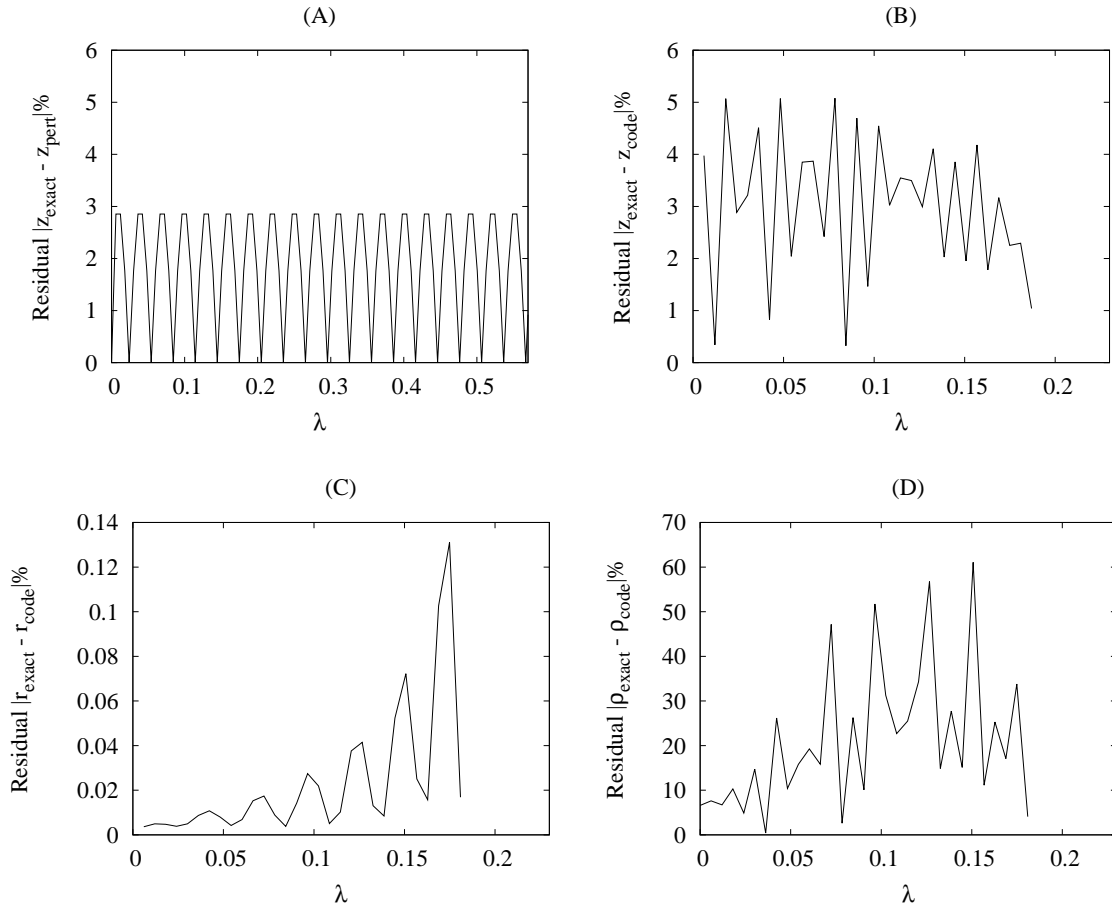


Figure 5.18: Error propagation of a 3% relative cyclic input error in  $z$  shown in (A). In (B), the output error on  $z$ , (C) the output error on  $\hat{r}$  and in (D) the output error on  $\rho$ .

**Random errors on  $z$  with  $z_{max} \approx (1 \pm 0.1)z$**

To investigate the effect of  $z$  on  $\rho$  further, the calculation is repeated but using a random error in  $z$  with relative peaks around 10% (Figure 5.19 (A)). Figures 5.19 (B), (C) and (D) again show the output after it was propagated over 500 time steps to the youngest PNC at  $u_{max} = 0.35$  for the EdS model.

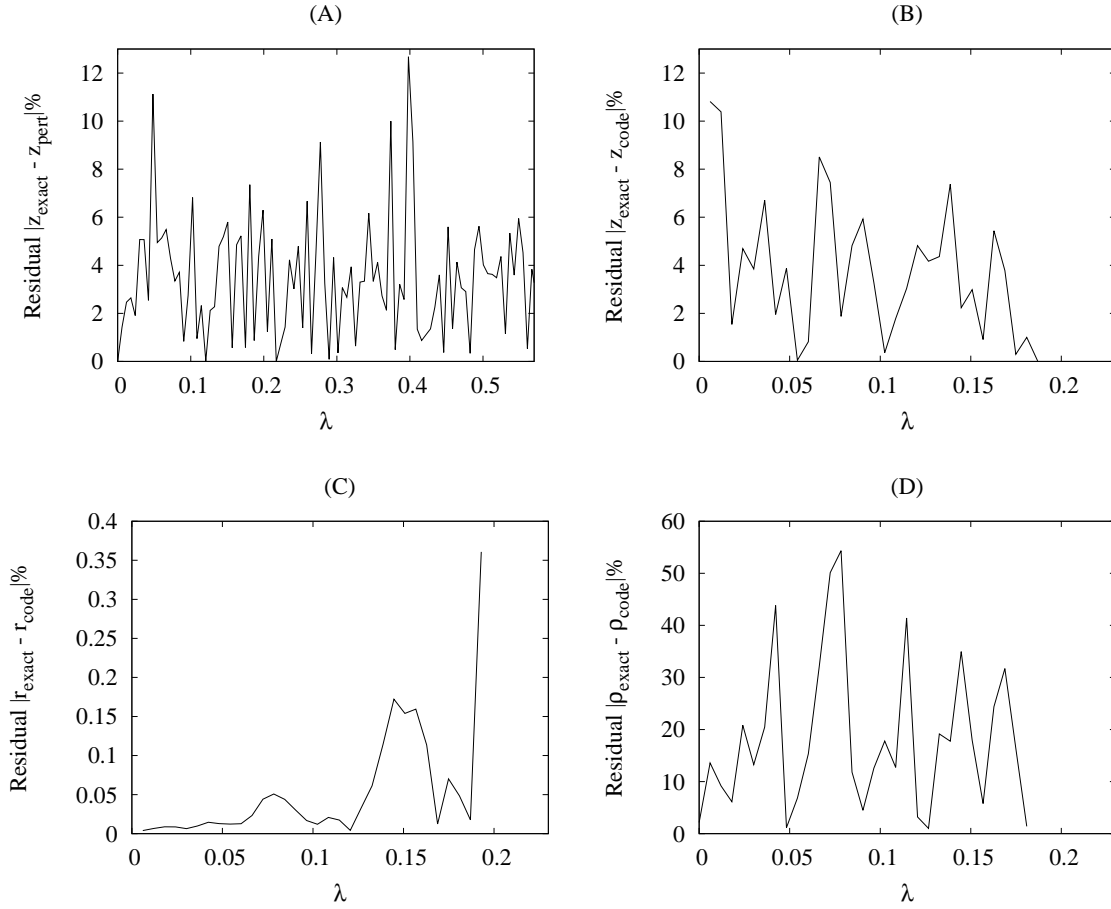


Figure 5.19: Error propagation of a relative random input error in  $z$  that peaks around 10% shown in (A). In (B), the output error on  $z$ , (C) the output error on  $\hat{r}$  and in (D) the output error on  $\rho$ .

## 5.5 Code verification: Discussion

### 5.5.1 Model comparison

#### Bondi-Sachs CIVP

Since the AH is the theoretical limitation using the diameter distance as radial coordinate for this model, it is relevant to evaluate the model's stability in terms of the time and distance relative to the AH. The EdS case was stable up to  $0.82 u_{AH}$  and  $0.82 r_{AH}$  and the LTB (bang-time with  $b = -0.5$ ) case up to  $0.75 u_{AH}$  and  $0.8 r_{AH}$  with  $u_{AH}$  and  $r_{AH}$  the time and distance values at the AH. The limits chosen are the maximum values where stable solutions were achieved on a regular grid. Extending these limits further causes the code to break down rapidly, which is the expected behaviour close to the AH. The radial outer limits of the initial PNCs correspond to observations at  $z = 0.47$  and  $z = 0.48$  in the EdS and LTB cases respectively. By reducing the extent of  $u$  limit, the radial extent can be increased and conversely reducing the radial limit allows the  $u$  limit to be increased, for instance values of  $0.2 u_{max}$  and  $0.99 r_{max}$  ( $z = 1.02$ ) also produce stable results for the EdS model. The stability in terms of the radial and evolution limits is dependent on the input data and the simulations in Section 5.6.2 were stable up to  $z \approx 1$ , which is a significant region for SNIa redshift-distance observations.

#### Affine CIVP

As before, the radial extent of the results are the maximum values for which the calculations were found to be stable on a regular grid. The region most interesting for the current investigation is that around the AH, which is well within the domain of calculation and therefore, special techniques to extend the radial boundaries were not considered. In comparison with the Bondi-Sachs calculations, significant improvements in the region covered were obtained. In terms of the redshift  $z$ , the extent of stable calculations was increased to  $z = 4.5$  and  $z = 1.2$  for EdS and LTB respectively, which are in both cases well beyond the AH (i.e.  $z$  at  $r_{max}$  in Table 5.2).

Figure 5.7 B provides a particularly interesting illustration of an observer's perception of distance in an inhomogeneous universe. Here, the  $(\hat{r}, z)$  behaviour on earlier PNCs includes loops, which will completely obscure the perception of diameter distance and redshift as measures of distance. This type of behaviour provides insight into the physical nature of a model by investigating its past behaviour. Although the initial PNC of the specific LTB model is not significantly out of line compared to more accepted models, especially on low redshifts, its past behaviour is rather unusual. This does not make it unrealistic, but does say that an observer at  $u = u_{max}$  would have found the interpretation of cosmological data particularly difficult.

### 5.5.2 Convergence

The accuracy of the code is overall very good, however, the regions where calculations were done using series expansions have visibly larger errors on all the error plots (Figures 5.10 A and B and Figures 5.11 A, B and C). For the investigations, here, accurate behaviour around the AH were of more interest and errors around  $r \approx 0$  were not handled with special techniques. While improvements are likely to be made using refinement methods, the unmodified results are presented since it illustrates that local errors were not significantly propagated radially and remained local. The errors around  $r \approx 0$  also reduced significantly when the code was refined.

The order of convergence of the different models were around second order for all the models. The calculated values are summarised in Table 5.3.

Model	Order of convergence
Bondi-Sachs EdS	2.28
Bondi-Sachs LTB ( $b = -0.5$ )	1.64
Affine EdS	2.22
Affine LTB ( $b = -0.5$ )	1.71
Affine $\Lambda$ CDM	2.19

Table 5.3: Summary of convergence results.

### 5.5.3 Sensitivity to errors

In both the constant and random cases, the model values evolved to the oldest PNCs, propagated the errors proportional to their initial values. While these are somewhat higher at the oldest PNC, they were still of the same order of magnitude when errors in corresponding input and output variables are compared. For corresponding input and output variables, the conclusion from this investigation, is that the code does not introduce significant artificial dispersion when the input data is not idealised. Conversely, Figure 5.13, which uses a *sine* input function, illustrates that input errors are not artificially diffused through the calculation.

By evaluating the errors on each input variable compared to all output variables, however, it was shown that  $\rho$  is the most sensitive output variable and particularly vulnerable to errors in  $z$  (see Figures 5.17 and 5.18). This issue was further investigated by introducing a random error on the input data of  $z$  and it was found that the effect on  $\rho$  is less severe: a random error with relative peaks around 10%, compared with a cyclic error with a relative amplitude of 3% (compare Figures 5.18 and 5.19). Nevertheless, the effect of  $z$  on  $\rho$  does not follow the stability trend of the other input variables and will require further investigation. This will form part of a more detailed analysis, which will explore the model's sensitivity with realistic data as input. This will give insight into the behaviour of the code when observational data becomes sufficiently complete for actual simulations.

## 5.6 Numerical experiments

Following from the *Isotropic Observations Theorems* (Theorems 2 and 3 in Section 2.3.2), any reasonable set of spherical symmetrical observations can be accommodated by some distribution

of inhomogeneities in a LTB model. After the discovery of dark energy from SNIa observations in 1998 [77, 83], using this principle, it was demonstrated by C el erier [21] that the observational effects perceived as dark energy can be caused by radial inhomogeneities<sup>5</sup>. In this section, two numerical experiments are presented that are related to the observational ambiguity that exists between  $\Lambda$ CDM and LTB models.

### 5.6.1 $\Lambda$ CDM versus LTB — evolution

The concept of inhomogeneities mimicking dark energy has been investigated many times since the publication of the SNIa observations, mostly as toy models demonstrating the ambiguities that exist in the interpretation of observations. The philosophical argument against LTB universes is that they place the observer in the centre of the Universe which, although not impossible is not a philosophically appealing idea. Even so, with a CIVP code at hand, an interesting numerical experiment is to test the historical evolution of an LTB model, with a zero cosmological constant, when observational data representing that of the  $\Lambda$ CDM model is interpreted as being caused by inhomogeneities.

A simple simulation set up for this experiment is done by calculating the density  $\rho$  and covariant velocity  $v_1$  profiles on the observer PNC by transforming exact solutions for a flat  $\Lambda$ CDM model to null coordinates. These are then used as input to the code, calculated with  $\Omega_\Lambda = 0$ , and compared to the transformed model where  $\Omega_\Lambda \neq 0$ . Parameter values are used to represent the actual Universe as  $\{H_0, \Omega_k, \Omega_{m0}, \Omega_\Lambda\} = \{72 \text{ Mpc s}^{-1} \text{ km}^{-1}, 0, 0.3, 0.7\}$  in the setup described in Section 5.1.1. It is, however, important to be aware that  $\rho_m$  in the  $\Lambda$ CDM model is determined by parameters related to the expansion and the density content and not by an independent measure of matter distribution such as number counts (see equation (2.29)). The additional degree of freedom introduced in the LTB model is therefore not purely satisfied by an additional boundary condition which is a limitation that should be borne in mind when interpreting redshift dimming as an LTB model.

Figure 5.20 shows the resulting LTB vs.  $\Lambda$ CDM evolutions back in time. While it might currently not be possible to distinguish these models from one another based on observations on the PNC, in the past, these universes are distinctly different. In particular, the LTB universe seems to be heading towards a singularity much faster than the  $\Lambda$ CDM universe and would therefore be significantly younger, if the trend is to continue beyond the calculations.

### 5.6.2 LTB versus $\Lambda$ CDM — matching

A question arising from the results presented in Figure 5.20 is: if the LTB null cones in the past would also represent  $\Lambda$ CDM flat space null cones? In this section an attempt is made to find a matching  $\Lambda$ CDM model for the  $t_0 - 6\text{Gyrs}$  LTB null cone. The procedure followed here is to firstly find a null cone in the past of a selected  $\Lambda$ CDM model for which the density corresponds to the LTB density at  $r = 0$ . This gives a density curve which has the same starting point but the slope of the curve differs to that of the LTB model. The slope of the curve is then matched by adjusting the Hubble rate ( $H_0$ ) until it approximately corresponds to the LTB curve. The covariant velocities ( $v_1$  as a function of  $r$ ) are then compared to see, qualitatively, if the models

<sup>5</sup> The idea of using inhomogeneities to mimic cosmic acceleration was also independently demonstrated by [95, 29, 74] but not directly based on this concept (also see [23]).

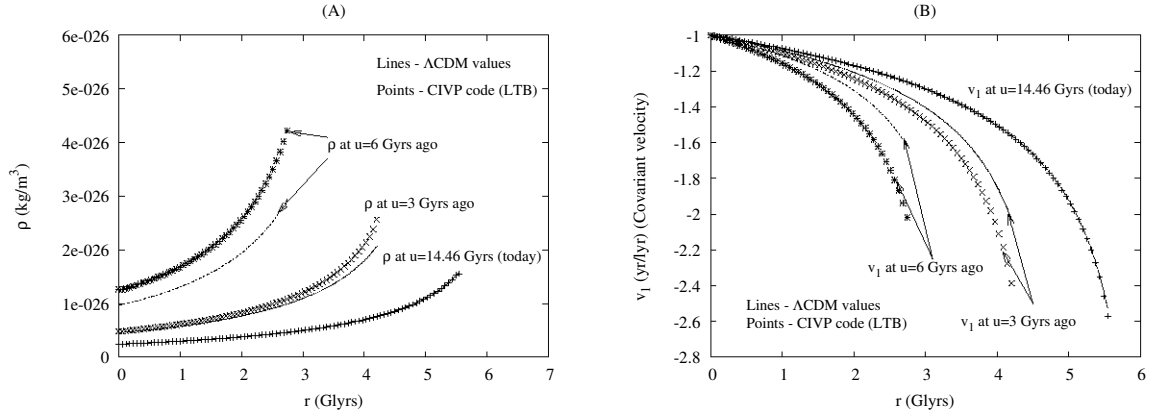


Figure 5.20: Density distribution (A) and covariant velocity (B) on past null cones at different proper times ( $u$ )

can be regarded as the same.

The models investigated are summarised in Table 5.4 and detailed results are shown in the Figures 5.21 to 5.24. From Table 5.4 it can be seen that the matching instances are from universes with different ages and matching takes place at different times in their evolutions. From the detailed results, it becomes apparent that matching both the radial matter distribution and expansion through  $\rho$  and  $v_1$  is an unlikely proposition. Applying the matching procedure to  $\rho$  causes  $v_1$  to move away from the  $\Lambda$ CDM data while  $\rho$  moves away when  $v_1$  is matched. This then suggests that the PNCs do not represent a  $\Lambda$ CDM model. This is an illustration of similar conclusions found by Yoo, Kai & Nakao [20].

$\Omega_\Lambda$	$H_0$ ( $\text{Mpc s}^{-1} \text{ km}^{-1}$ )	Age ( $t_0$ ) (Gyrs)	Density matching time ( $t_{match}$ ) (Gyrs)	Figure
0	59	12.37	7.85	5.21
0.5	68	13.28	7.70	5.22
0.7	72	14.46	7.66	5.23
0.9	64	21.48	7.52	5.24

Table 5.4:  $\Lambda$ CDM models used to match the LTB density profile.

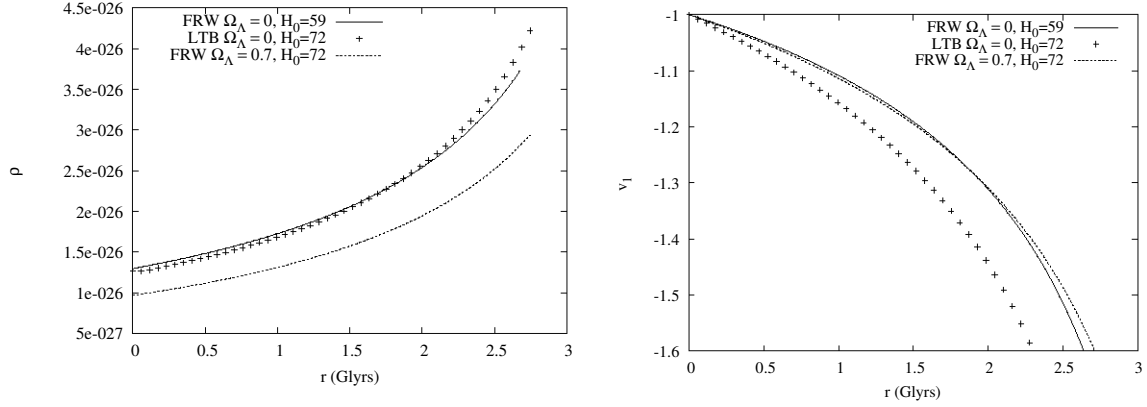


Figure 5.21: Density distribution and covariant velocity on the past null cones: LTB with  $\Omega_\Lambda = 0$  and FLRW with  $\Omega_\Lambda = 0.7$  at  $t_0 - 6\text{Gyrs}$  and the best fit FLRW  $\Omega_\Lambda = 0$  instance.

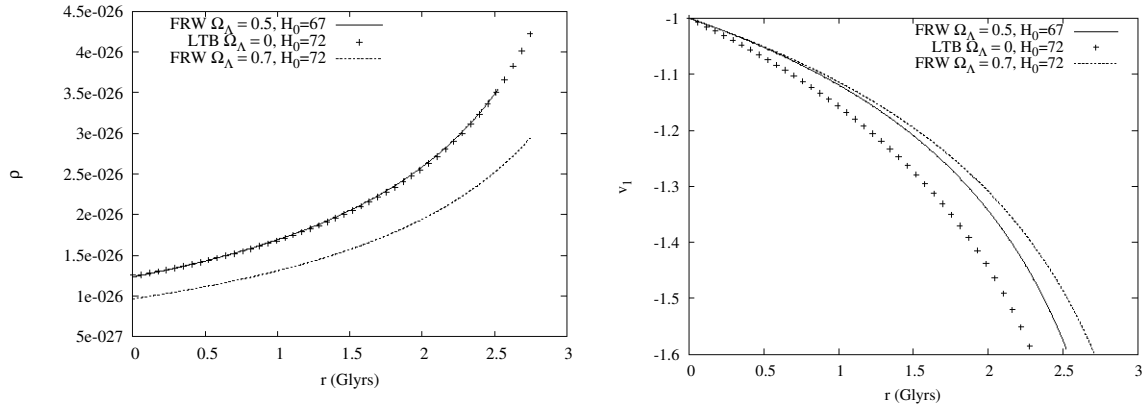


Figure 5.22: Density distribution and covariant velocity on the past null cones: LTB with  $\Omega_\Lambda = 0$  and FLRW with  $\Omega_\Lambda = 0.7$  at  $t_0 - 6\text{Gyrs}$  and the best fit FLRW  $\Omega_\Lambda = 0.5$  instance.

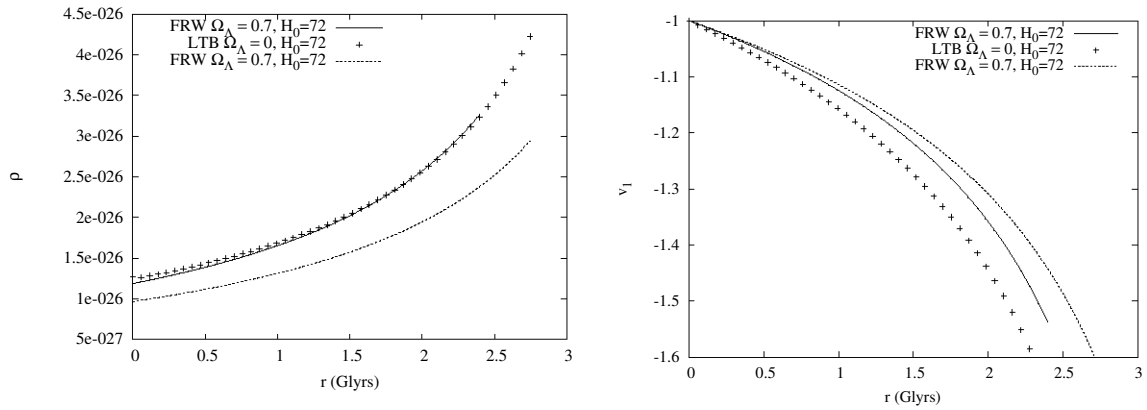


Figure 5.23: Density distribution and covariant velocity on the past null cones: LTB with  $\Omega_\Lambda = 0$  and FLRW with  $\Omega_\Lambda = 0.7$  at  $t_0 - 6\text{Gyrs}$  and the best fit FLRW  $\Omega_\Lambda = 0.7$  instance.

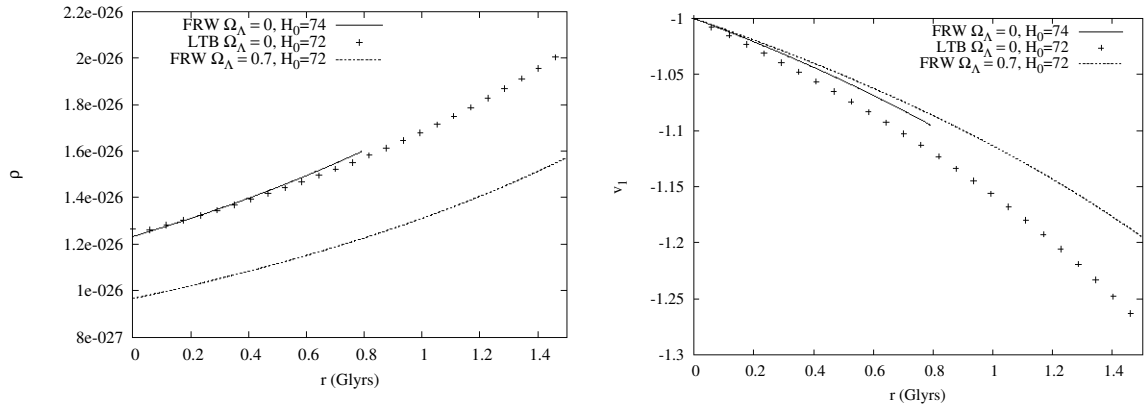


Figure 5.24: Density distribution and covariant velocity on the past null cones: LTB with  $\Omega_\Lambda = 0$  and FLRW with  $\Omega_\Lambda = 0.7$  at  $t_0 - 6\text{Gyrs}$  and the best fit FLRW  $\Omega_\Lambda = 0.9$  instance. The stable region for this plot is limited to a smaller region but also shows an unlikely match for both  $\rho$  and  $v_1$  simultaneously.

## 5.7 Conclusion

In this chapter the accuracy and stability of the code was evaluated by comparing the code evolution against known solutions of the EdS, LTB and  $\Lambda$ CDM models. The Bondi-Sachs CIVP was found to be second order accurate and convergent in the region approaching to the AH for models where  $\Lambda = 0$ . The affine CIVP, developed specifically for the cosmological PNC, produced the same level of accuracy up to regions well beyond the AH for models without the restriction of  $\Lambda = 0$ .

It was also demonstrated that errors in initial conditions propagate without being excessively amplified through the code evolution; i.e. the size of the error remains of the same order for input errors in  $\rho$  and  $r$ . It was further found that  $\rho$  is the most sensitive output variable, in particular, when cyclic input errors are introduced in  $z$ . However, without special consideration to this issue, the code remains stable within reasonable limits when subjected to random errors in all variables. These results were mostly illustrative but will be the starting point of further investigation into the model's behaviour when subjected to real observations.

In an illustration of a typical application of the code, it was shown how an LTB model will behave if evolved from  $\Lambda$ CDM initial data. This is an investigation concerning the ambiguities in observations that exist between inhomogeneities and dark energy. It was found that the density of the LTB model rises significantly more quickly indicating a much younger universe, possibly too young if this trend continues.

Further investigation on the oldest PNC calculated, demonstrated that density and redshift distributions cannot be matched by any flat  $\Lambda$ CDM model. This has an important implication: Although the initial values of the two models can correspond on the current PNC, the histories of the two models are distinctly different. Conversely, a universe that was distinctly inhomogeneous in the past can evolve to density and redshift distributions identical to that of the  $\Lambda$ CDM model

A more fundamental statement of this result is that while in our current epoch the LTB vs.  $\Lambda$ CDM ambiguity is difficult to disentangle, this is a feature of the Universe's current state and not its past. *In other words, if the Universe is inhomogeneous without a cosmological constant, not only is the observer in a privileged position (near a central point), he also lives in a specific time where the Universe can appear to be either LTB or  $\Lambda$ CDM.*

# Chapter 6

## Conclusion

This work is a presentation of developments towards a numerical model of the observable universe. For this purpose the characteristic formalism, used in gravitational wave simulations, was adapted for modelling the cosmological past null cone.

### 6.1 Summary

The distinction between parameterized and observational cosmological models is the basic argument towards the developments described in this thesis. While it is common practice in cosmology to explore the theoretical aspects of the Universe by the fitting of parameters on an assumed cosmology, this approach is effectively an existence argument, showing that there is a model that can reproduce observed cosmological parameters. On the other hand, uniqueness can be obtained by observational models where boundary conditions are derived from quantities observed on a past null cone (PNC). This idea is based on the concept of restricting a general cosmology to a more specific one using boundary conditions. Under ideal circumstances, this approach proves the fundamental limits of theoretical deductions from observations. In practice, a very precise map of the Universe is required for observational models and if the predictions of the unobservable energy-matter content by parameterized models are correct; a distant prospect that might not be practically attainable. These aspects are described in some detail in Chapter 2 with the conclusion that an observational model with some of the assumptions from parameterized models can be a valuable testing ground for proposed parameterized cosmologies.

A model of the observable universe, based on the characteristic formalism used in numerical relativity, was developed for this purpose. The characteristic formalism presents the EFEs as a characteristic initial value problem (CIVP) on a coordinate system aligned with outgoing null cones. This frame of reference was initially developed to model gravitational waves. With some minor adjustments to the original model, it was described in Chapter 3 how this model can be used to model a cosmological PNC. This involved a derivation from the EFEs, using the Bondi-Sachs metric, in spherical symmetry for a dust-like fluid. Effectively, this is the LTB model in Bondi-Sachs coordinates. An important consideration with the Bondi-Sachs coordinates is that the diameter distance ( $d_D$ ) is used as a radial coordinate. Since the diameter distance increases

with distance until a maximum and then decreases as the PNC in an expanding universe refocusses,  $d_D$  is not a unique coordinate and becomes multi-valued after the apparent horizon (AH). To address the limited radial extent of the Bondi-Sachs CIVP, a model was derived where the diameter distance was replaced by an affine parameter ( $\lambda$ ) defined on a past directed null geodesic connected to the observer (i.e. on the observer's PNC). Moreover, the model was then derived using EFEs with a cosmological constant, making it suitable to investigate the PNC behaviour of cosmologies where both inhomogeneities and the cosmological constant can be modelled. Since a null geodesic originating from the observer has a known position with a coordinate condition stating the tangent, the radial coordinate is uniquely defined. This model is expected to be suitable for simulating the PNC well beyond the AH.

A numerical implementation of this concept is described in Chapter 4. The numerical scheme used is an adaption for cosmology of the developments for 3D modelling of gravitational waves in [10] and [11]. This is a second order explicit scheme where a set of hierarchical equations are separated between geometrical (hypersurface) equations and energy-momentum (evolution) equations. The hypersurface equations are solved on a specific PNC and the resulting values are then substituted in the energy-momentum equations, which are to perform a reverse time step to a PNC in the model's historical evolution. The energy-momentum equations, however, contain coordinate singularities at the null cone vertices, a region excluded of calculations for gravitational wave modelling. For cosmology, the cone vertices are of particular interest since they represent the positions of observers. Since the model is not directly suitable in this region, series expansions of the CIVP equations have to be used in the vicinity of the observer. The outer radial boundary of the model is evolved without constraints but since the purpose of the model is to represent the verifiable region of a cosmological observer, the region is restricted by an incoming characteristic connected to the outer limit on the observer's PNC surface. In principle, then, the domain of calculation (Figures 4.1 and 4.3) only represents the causally connected region of a local observer.

The success of the implementation is the measure convergence, which by design is expected to be second order, and stability. For this purpose, the code was evaluated in Chapter 5 by comparing the evolution against known solutions of the EdS, LTB and  $\Lambda$ CDM models. The Bondi-Sachs CIVP was found to be second order convergent in the region approaching the AH for models with  $\Lambda = 0$ . In the vicinity of the AH the code broke down as expected. The affine CIVP produced the same level of accuracy up to regions well beyond the AH for the same models and also for models with  $\Lambda \neq 0$ . It was also demonstrated that errors in initial conditions propagate without being excessively amplified through the code evolution; i.e. the size of the error remains of the same order. These results are intended to be the starting point of further investigation into the model's behaviour when subjected to realistic observations.

As an illustration of a typical application of the code, it was shown how an LTB model will behave if evolved from  $\Lambda$ CDM initial data. This is an investigation concerning the observational ambiguity between inhomogeneities and dark energy. Comparing the historical PNCs, it was found that the density of the LTB model rises more rapidly than the  $\Lambda$ CDM's, suggesting a much younger universe, possibly too young if the trend continues. Further investigation on the oldest PNCs, demonstrated that density and redshift distributions cannot be matched by any flat  $\Lambda$ CDM model. This has an important implication: Although the initial values of the two models can correspond on the current PNC, the histories of the two models are distinctly different. Therefore, an inhomogeneous early universe can evolve to density and

redshift observations identical to that of the  $\Lambda$ CDM model. A more fundamental statement of this result is that while in our current epoch the LTB vs.  $\Lambda$ CDM ambiguity is difficult to disentangle, this is a feature of the Universe's current state and not its past. *In other words, if the Universe is inhomogeneous without a cosmological constant, not only is the observer in a privileged position (near a central point), he also lives at a specific time where the Universe can appear to be either LTB or  $\Lambda$ CDM.*

## 6.2 Future developments

As demonstrated in this thesis, the development of the affine CIVP model and code provides a model where parameterized investigations of the evolution of the observable universe can be done by providing some interpretation of current observations. Future developments are planned to make provision for the incorporation of actual observations. Measurement of the redshift-drift planned for the next generation of telescopes, such as the E-ELT looks particularly promising to provide such input. Data from the E-ELT is, however, still a future prospect. Until then, data from cosmic chronometers can provide interesting insight on observational models.

In addition, the code can also be expanded to incorporate more general models than the spherical symmetric dust models investigated in the work presented here. This can provide a ground for modelling inhomogeneities where the effects of nonlinearity is not fully represented when suppressing degrees of freedom. Investigating the accumulation of inhomogeneities in backreaction models would be an interesting example to model in more degrees of freedom than the typical spherical symmetric models.

# Appendix A

## Summary of symbols

### A.1 Symbols in cosmology – Chapter 2

#### A.1.1 Coordinates

Symbol	Description	Equation
$t$	Cosmic time on the observer world line	2.16
$r$	Comoving radial distance	2.16
$\theta$	Comoving spherical latitude angle	2.16
$\varphi$	Comoving spherical longitude angle	2.16
$u^a$	4-velocity (contravariant form)	2.13
$k^a$	Ray 4-vector (contravariant form)	2.53
$v$	Affine parameter	2.9

#### A.1.2 Observable quantities

Symbol	Description	Equation
$\lambda$	Wavelength of EM radiation	2.54
$\nu$	Wave frequency of EM radiation	2.55
$z$	Redshift	2.54
$n$	Proper number density	2.67
$N$	Cosmological number count	2.67
$d_L$	Luminosity distance	2.63
$d_D$	Diameter distance	2.65
$m$	Apparent magnitude	2.64
$M$	Absolute magnitude	2.64
$L$	Absolute luminosity	2.63
$F$	Radiative flux	2.63
$dS$	Intrinsic surface area	2.65
$d\Omega$	Solid angle $dS$ subtends to	2.65
$J$	Completeness parameter	2.70
$\mathcal{M}_g$	Mass per galaxy	2.71

### A.1.3 Physical quantities

Symbol	Description	Equation
$\rho$	Density	2.20
$p$	Pressure	2.20
$\Lambda$	Cosmological constant	2.10
$H$	Hubble rate	2.21
$H_0$	Hubble constant $H(t = 0)$	2.21
$q_0$	Deceleration parameter	2.25
$\Omega_i$	Density parameter	2.24
$a(t)$	FLRW scale factor	2.16
$k$	FLRW curvature index	2.16
$E(r)$	LTB curvature function	2.31
$M(r)$	LTB mass function	2.31
$t_B(r)$	LTB bang time function	2.37-2.39
$R(t, r)$	LTB scale factor	2.31
$c$	Speed of light	
$G$	Gravitational constant	
$\kappa$	Gravitational coefficient	

## A.2 Symbols in NR – Chapters 3 and 4

Symbol	Description	Equation
$u$	Proper time on a time-like geodesic	3.1
$r$	Diameter distance	3.1
$\theta$	Spherical latitude angle	3.1
$\varphi$	Spherical longitude angle	3.1
$\beta$	Bondi-Sachs cross term coefficient	3.1
$W$	Bondi-Sachs time coefficient term	3.1
$\lambda$	Affine parameter	3.36
$v^a$	4-velocity (contravariant form)	3.11
$\hat{r}$	$r(\lambda)$	3.39
$\hat{W}$	Affine metric time coefficient term	3.39
$\hat{R}$	Affine CIVP auxiliary variable	4.20
$\hat{S}$	Affine CIVP auxiliary variable	4.19
$\hat{T}$	Affine CIVP auxiliary variable	4.22
$\hat{U}$	Affine CIVP auxiliary variable	3.54
$\tilde{r}$	Comoving radial distance	3.16
$\tilde{g}_{ab}$	Metric in comoving coordinates	3.18

### A.3 Relativistic symbols

Symbol	Description	Equation
$g_{ab}$	Metric tensor	2.1
$\Gamma_{bc}^a$	Christoffel symbols	2.2
$R^d{}_{abc}$	Riemann tensor	2.4
$R_{ab}$	Ricci tensor	2.5
$R$	Ricci scalar	2.6
$T_{ab}$	Stress tensor	2.17

### A.4 Abbreviations

The following table refers to abbreviations used in the text. The reference will point to the definition of the term if it was explicitly defined, otherwise, to its first usage.

Abbreviation	Description	Reference
AH	Apparent horizon	Section 2.2.3
CIVP	Characteristic initial value problem	Chapter 3 (p. 44)
CMB	Cosmic microwave background	Section 1.1.2
CS	Comoving synchronous	Section 2.1.1
EFEs	Einstein field equations	Section 2.1.1
EMR	Electromagnetic radiation	Section 1.1
FLRW	Friedman Lemaître Robertson Walker	Section 1.1.2
FR	Fluid-ray	Section 2.3.3
HST	Hubble space telescope	Section 2.2.1
$\Lambda$ CDM	$\Lambda$ cold dark matter	Section 2.2.1
LSS	Last scattering surface	Section 1.1
LTB	Lemaître Tolman Bondi	Section 2.2.2
NR	Numerical relativity	Section 2.17
OC	Observational cosmology	Section 1.1.3
PNC	Past null cone	Section 2.2.3
SNIa	Type Ia supernovae	Section 2.1.2

# Appendix B

## Maple code

### B.1 Affine CIVP

```
#####  
#  
# Determine the hypersurface and evolution equations for the Affine CIVP  
#  
#####  
restart;  
  
#Setup coordinates  
x := array(1 .. 4);  
x[1] := u;  
x[2] := lambda;  
x[3] := theta;  
x[4] := varphi;  
  
#Setup metric  
g := array(1 .. 4, 1 .. 4);  
  
for a to 4 do  
for b to 4 do  
g[a, b] := 0  
end do  
end do;  
  
g[1, 1] := -1-W(u, lambda)/r(u, lambda);  
g[1, 2] := -1;  
g[2, 1] := -1;  
g[3, 3] := r(u, lambda)^2;  
g[4, 4] := r(u, lambda)^2*sin(theta)^2;  
  
#Setup contravariant metric  
with(linalg);  
ginv := inverse(g);  
  
#Determine Christoffel symbols  
for a to 4 do  
for b to 4 do
```

```

for c to 4 do
christoffel[a, b, c] := 0;
for d to 4 do
christoffel[a, b, c] := christoffel[a, b, c]
+(1/2)*ginv[a, d]*(diff(g[d, b], x[c])+diff(g[c, d], x[b])
-(diff(g[b, c], x[d])))
end do
end do
end do
end do;

#Determine Riemann tensor
for a to 4 do
for b to 4 do
for c to 4 do
for d to 4 do
Riemann[a, b, c, d] := diff(christoffel[a, b, d], x[c])
-(diff(christoffel[a, b, c], x[d]));
for e to 4 do
Riemann[a, b, c, d] := simplify(Riemann[a, b, c, d]
+christoffel[a, e, c]*christoffel[e, b, d]
-christoffel[a, e, d]*christoffel[e, b, c])
end do
end do
end do
end do
end do;

#Determine Ricci tensor
Ricci := array(1 .. 4, 1 .. 4);
for a to 4 do
for b to 4 do
Ricci[a, b] := 0;
for c to 4 do
Ricci[a, b] := simplify(Ricci[a, b]+Riemann[c, a, c, b])
end do
end do
end do;

#Setup covariant velocity
v := array(1 .. 4);
v[1] := v0(u, lambda);
v[2] := v1(u, lambda);
v[3] := 0; v[4] := 0;

#Setup stress tensor
for a to 4 do
for b to 4 do
T[a, b] := simplify(v[a]*v[b]*rho(u, lambda))
end do
end do;

#Stress scalar
Tscalar := -rho(u, lambda);

#Determine the EFEs

```

```

for a to 4 do
for b to 4 do
Einstein[a, b] := simplify(Ricci[a, b]
-kappa(T[a, b]-(1/2)*Tscalar*g[a, b])-Lambda*g[a, b] = 0)
end do
end do;

#Determine the matter conservation equation
convmat := 0;
for a to 4 do
for b to 4 do
convmat := convmat+(diff(rho(u, lambda), x[a]))*v[b]*ginv[a, b]
+rho(u, lambda)*(diff(v[a], x[b]))*ginv[a, b];
for c to 4 do
convmat := convmat-rho(u, lambda)*christoffel[c, a, b]*v[c]*ginv[a, b]
end do
end do
end do;

matter := simplify(isolate(convmat = 0, diff(rho(u, lambda), u)));

#Determine the momentum conservation equations
convmom := array(1 .. 4);
for i to 4 do
convmom[i] := 0
end do;

for a to 4 do
for b to 4 do
for c to 4 do
convmom[a] := convmom[a]+rho(u, lambda)*(diff(v[a], x[b]))*v[c]*ginv[b, c];
for d to 4 do
convmom[a] := convmom[a]
-rho(u, lambda)*christoffel[d, a, b]*v[d]*v[c]*ginv[b, c]
end do
end do
end do
end do;

momentum := simplify(isolate(convmom[2] = 0, diff(v1(u, lambda), u)));

#Display hypersurface equations
eval(sort(simplify(isolate(Einstein[1, 2], diff(diff(W(u, lambda), lambda), lambda))), desc));
eval(isolate(Einstein[2, 2], diff(r(u, lambda), lambda)));
eval(sort(simplify(isolate(Einstein[3, 3], diff(diff(r(u, lambda), u), lambda))), desc));

#Display evolution equations
eval(momentum);
eval(matter);

```

## Appendix C

# Fortran code

The Fortran code for the affine CIVP model is listed in this appendix. As supporting documentation to the code, a conceptual flowchart, a call graph and a list of the routines in the program is also presented.

## C.1 Code layout

### C.1.1 Flowchart

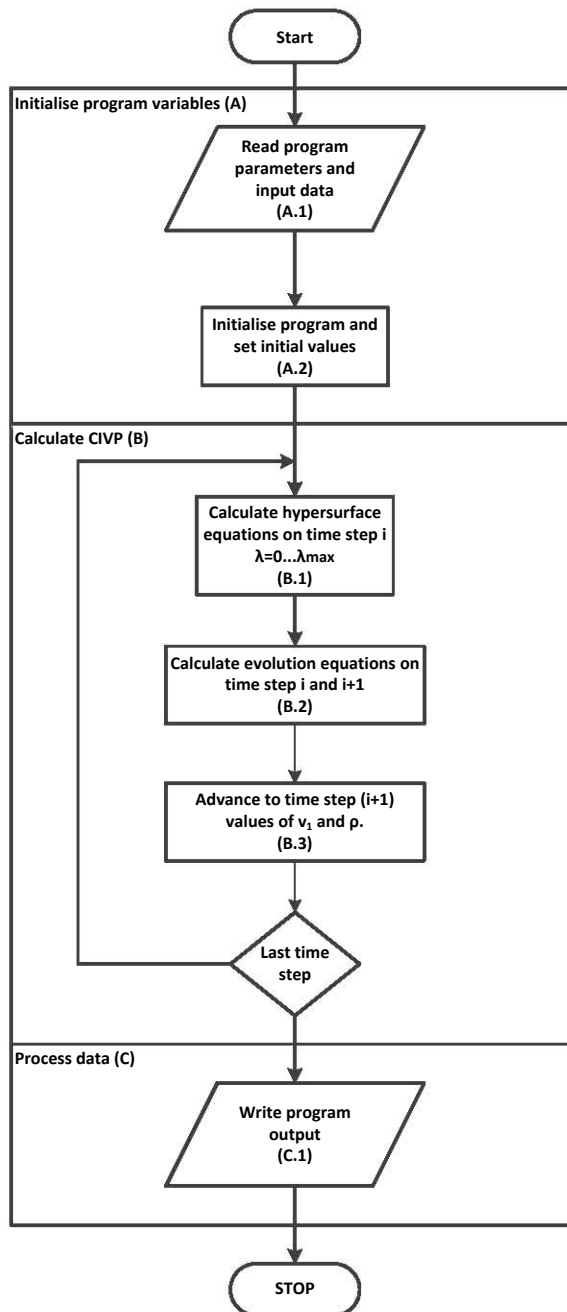


Figure C.1: Conceptual flowchart for the affine CIVP Fortran code.

### C.1.2 Call graph

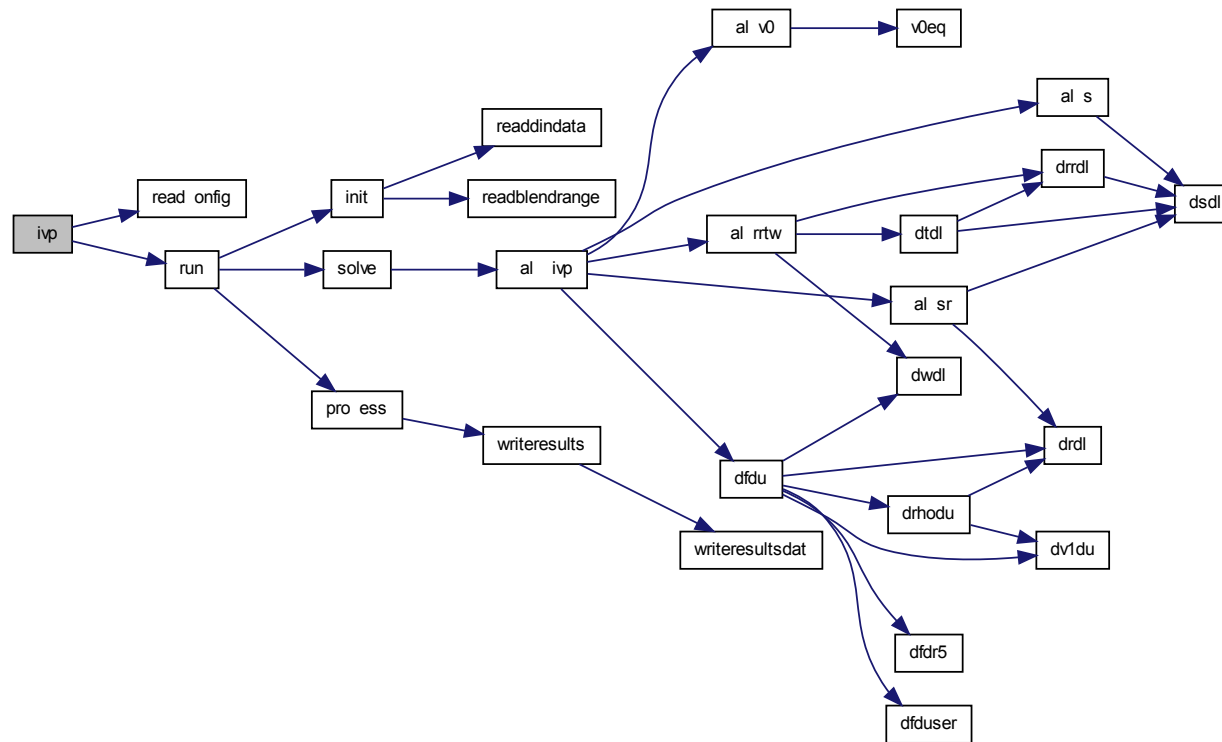


Figure C.2: Call graph for the affine CIVP Fortran code.

### C.1.3 Program routines

With reference to Figures C.2 and C.1, Table C.2 summarises the modules of the code.

Procedure	File	Description	Flowchart label
civp	affine.civp.for	Main program entry point.	
readConfig	affine.io.for	Read the grid resolution and $\Lambda$ -value. cosmological constant from the 'grid.in' file.	A.1
run	affine.civp.for	Control procedure for program execution.	
init	affine.civp.for	Initialise program variables	A
readBlendRange	affine.io.for	Read the radial region where transition between the CIVP and series solutions will be done.	A.1
readInData	affine.io.for	Read initial and comparative data from the 'affine.init.in' file.	A.1
solve	affine.civp.for	Entry point for calculation procedures.	B
calcCIVP	affine.calc.evol.for	Control procedure for main calculations.	B
calcS	affine.calc.hyp.for	Calculate the variable $S$ .	B.1 & 2
calcSr	affine.calc.hyp.for	Calculate the variables $S$ and $r$ .	B.1 & 2
calcRRTW	affine.calc.hyp.for	Calculate the variables $R$ , $W$ and $T$ .	B.1 & 2
dSdl	affine.model.for	Calculate equation (4.19).	B.1 & 2
dRdl	affine.model.for	Calculate equation (4.20).	B.1 & 2
dWdl	affine.model.for	Calculate equation (4.21).	B.1 & 2
dTdl	affine.model.for	Calculate equation (4.22).	B.1 & 2
calcv0	affine.calc.evol.for	Calculate $v_0$ using (4.23).	B.2
dv1du	affine.model.for	Calculate equation (4.24).	B.2
drhodu	affine.model.for	Calculate equation (4.25).	B.2
calcFdu	affine.calc.evol.for	Calculate $\rho_{,u}$ and $v_{1,u}$ .	B.2
calcFduser	affine.model.for	Calculate $\rho_{,u}$ and $v_{1,u}$ using a series expansion.	B.2
calclmax	affine.calc.hyp.for	Calculate the radial maximum as an incoming. characteristic line.	B.2
dfdr5	affine.support.for	Support procedure to calculate a 5-point radial derivative.	B.2

Table C.1: Affine CIVP code modules.

Table C.2 continue.

Procedure	File	Description	Flowchart label
<code>process</code>	<code>affine.civp.for</code>	Entry point for post processing of the data i.e. writing to output files etc.	C
<code>writeResults</code>	<code>affine.io.for</code>	Control procedure for writing results.	C.1
<code>writeResultsData</code>	<code>affine.io.for</code>	Write the results in the '.dat' files.	C.1

Table C.2: Affine CIVP code modules.

## C.2 Code

```
c =====
c PROGRAM TO SOLVE THE CHARACTERISTIC INITIAL VALUE PROBLEM
c =====

program civp

  implicit none
  integer :: NI, NJ
  real*8 :: Llambda
  character(8) :: date
  character(10) :: time

  call readConfig(NI, NJ, Llambda)
  call date_and_time(DATE=date, TIME=time)

  call system('cls')
  write(*,*) '=====',
  write(*,*) 'AFFINE CIVP CODE CALCULATION ', ' ',date, ' ',time
  write(*,*) '=====',
  write(*,*) 'Input report'
  write(*,*) '-----',
  write(*,*) 'R-grid : ', NJ
  write(*,*) 'U-grid : ', NI
  write(*,*) '-----',
  write(*,*) 'Progress report'
  write(*,*) '-----',

  call run(NI,NJ,Llambda)

  call date_and_time(DATE=date, TIME=time)

  write(*,*) '-----',
  write(*,*) 'Calculation completed ', ' ',date, ' ',time
  write(*,*) '=====',

  stop

end program

include 'affine.support.for'
include 'affine.model.for'
include 'affine.calc.hyp.for'
include 'affine.calc.evol.for'
include 'affine.io.for'
include 'affine.units.for'

c -----
c Driver routine
c -----
subroutine run(NI,NJ,Llambda)
```

```

implicit none

!Parameters
  integer, intent(in) :: NI, NJ
  real*8, intent(in) :: Llambda

!Grid
  real*8 :: lambda(NJ), u(NI,NJ)

!Values to calculate
  real*8 :: r(NI,NJ), W(NI,NJ), Ru(NI,NJ)
  real*8 :: v1(NI,NJ), v0(NI,NJ), rho(NI,NJ)
  real*8 :: v1u(NI,NJ)

!Support variables
  real*8 :: dell, delu
  real*8 :: lbmin, lbmax
  integer :: ljmax(NI), uimax
  real*8 :: lmax(NI)

  write(*,*) 'Reading input data...'

  call init(lambda, u, dell, delu
    & , r, W, v0, v1, rho
    & , NI, NJ, ljmax, uimax
    & , lbmin, lbmax, Llambda)

  write(*,*) 'Solving CIVP equations...'

  call solve(lambda, u, delu, dell
    & , r, W, v0, v1, rho, v1u
    & , NI, NJ, ljmax, uimax, lmax
    & , lbmin, lbmax, Llambda)

  write(*,*) ''
  write(*,*) 'Processing data...'

  call process(lambda, u, dell, delu
    & , r, W, v0, v1, rho, v1u
    & , NI, NJ
    & , ljmax, lmax)

end subroutine

c -----
c Set initial values.
c -----
subroutine init(lambda, u, dell, delu
  & , r, W, v0, v1, rho
  & , NI, NJ, ljmax, uimax
  & , lbmin, lbmax, Llambda)

  implicit none

```

```

!Subroutine parameters
integer, intent(in) :: NI, NJ
  real*8, intent(inout) :: lambda(NJ), u(NI,NJ), dell, delu
  real*8, intent(inout) :: r(NI,NJ), W(NI,NJ)
    real*8, intent(inout) :: v0(NI,NJ), v1(NI,NJ), rho(NI,NJ)
  integer, intent(inout) :: ljmax(NI)
  integer, intent(inout) :: uimax
  real*8, intent(inout) :: lbmin, lbmax
real*8, intent(in) :: Llambda

  !Local variables

  integer :: i,j

real*8 :: rI(NJ), v1I(NJ), rhoI(NJ)
  real*8 :: lmax, umax

!Setup grid
call readGridData(lambda, u
  & , NI, NJ)

!Read initial data
  call readInitData(rI, v1I, rhoI
    & , NJ)

    call readBlendRange(lbmin, lbmax)

  umax = u(1,1) - u(NI,1)
  lmax = lambda(NJ)

  delu = umax / (NI-1)
  dell = lmax / (NJ-1)

!Display parameters
write(*,*) 'Uo-Umin      : ', umax
write(*,*) 'U-min       : ', u(NI, NJ)
write(*,*) 'lambda-max    : ', lmax
write(*,*) 'Del-U        : ', delu
write(*,*) 'Del-lambda   : ', dell
write(*,*) 'l-bmin      : ', lbmin
write(*,*) 'l-bmax      : ', lbmax
write(*,*) 'Lambda      : ', Llambda
write(*,*) 'CFL         : ', abs(delu/dell)
  write(*,*) '-----'
  write(*,*) ''

!Find uimax
uimax = NI

!Initialise r, W, v0, v1 & rho
do i=1,NI
do j=1,NJ
r(i,j) = 0.DO
W(i,j) = 0.DO
v0(i,j) = 0.DO
v1(i,j) = 0.DO
rho(i,j) = 0.DO

```

```

end do
end do

!Set boundary conditions on the current PNC
do j=1,NJ
r(1,j) = rI(j)
rho(1,j) = rhoI(j)
v1(1,j) = v1I(j)
end do

call readRadialMax(ljmax, NI)

end subroutine

c -----
c Solve the CIVP
c -----
subroutine solve(lambda, u, delu, dell
& , r, W, v0, v1, rho, v1u
& , NI, NJ, ljmax, uimax, lmax
& , lbmin, lbmax, Llambda)

implicit none

!Subroutine parameters
integer, intent(in) :: NI, NJ
real*8, intent(in) :: lambda(NJ), u(NI,NJ), dell, delu
real*8, intent(inout) :: r(NI,NJ), W(NI,NJ)
real*8, intent(inout) :: v0(NI,NJ), v1(NI,NJ), rho(NI,NJ)
real*8, intent(inout) :: v1u(NI,NJ)
real*8, intent(inout) :: lmax(NI)
integer, intent(inout) :: ljmax(NI)
integer, intent(in) :: uimax
real*8, intent(in) :: lbmin, lbmax, Llambda

!Local variables
integer :: i, j, report, p

report = NI/10

do i=1,uimax-1

if(mod(i,report) == 0 .or. i==uimax-1) then
write(*,*) ' time step=', i
end if

call calcCIVP(lambda, u, dell, delu
& , r, W, v0, v1, rho, v1u
& , NI, NJ, i, ljmax(i)
& , lbmin, lbmax, Llambda)

end do

write(*,*) ''
write(*,*) 'Calculating incoming geodesic cut-off...'

```

```

write(*,*) ' lmax 1: ', lmax(1)
write(*,*) ' lmax NI: ', lmax(NI)

end subroutine

c -----
c Process data and store in a file.
c -----
subroutine process(lambda, u, dell, delu
& , r, W, v0, v1, rho, v1u
& , NI, NJ
& , ljmax, lmax)

implicit none

!Parameters
integer, intent(in) :: NI, NJ, ljmax(NI)
real*8, intent(in) :: lambda(NI,NJ), u(NI,NJ)

real*8, intent(in) :: r(NI,NJ), W(NI,NJ)
real*8, intent(in) :: v0(NI,NJ), v1(NI,NJ), rho(NI,NJ)
real*8, intent(in) :: v1u(NI,NJ)

real*8, intent(in) :: delu, dell

real*8, intent(in) :: lmax(NI)

write(*,*) '-----',

call writeResults(lambda, u, dell, delu
& , r, W, v0, v1, rho, v1u
& , NI, NJ
& , ljmax, lmax)

end subroutine

c -----
c Calculate dSdl
c -----

real*8 function dSdl(S, lambda, par)

implicit none

!Parameters
real*8, intent(in) :: lambda !Required for general ODE function
real*8, intent(in) :: S !Required for general ODE function
real*8, intent(in) :: par(7)

!Local variables
real*8, parameter :: PI = 3.141592653589793
real*8 :: r, v1, rho
real*8 :: kappa, Llambda, G, c
c = 2.999e8

```

```

G = 6.667e-11
kappa = 8.D0*PI !*G !/c**4.D0

!Extract parameters
  r = par(1)
  v1 = par(2)
  rho = par(3)

!Calculate dSdl
  dSdl = -0.5D0*kappa*r*rho*v1**2.D0

end function

c -----
c Calculate drdl
c -----

real*8 function drdl(r, lambda, par)

  implicit none

!Parameters
  real*8, intent(in) :: lambda !Required for general ODE function
  real*8, intent(in) :: r !Required for general ODE function
  real*8, intent(in) :: par(7)

!Local variables
  real*8, parameter :: PI = 3.141592653589793
  real*8 :: S

!Extract parameters
S = par(1)

!Calculate drdl
  drdl = S

end function

c -----
c Calculate dRdl
c -----

real*8 function dRRdl(RR, lambda, par)

  implicit none

!Parameters
  real*8, intent(in) :: lambda !Required for general ODE function
  real*8, intent(in) :: RR !Required for general ODE function
  real*8, intent(in) :: par(7)

!Local variables
  real*8, parameter :: PI = 3.141592653589793
  real*8 :: r, S, T, W, v1, rho, dSdl
real*8 :: kappa, Llambda, G, c

```

```

c = 2.999e8
G = 6.667e-11
kappa = 8.D0*PI !*G !/c**4.D0
!Llamba = -1.25e-2

!Extract parameters
r = par(1)
S = par(2)
T = par(3)
W = par(4)
      v1 = par(5)
rho = par(6)
Llamba = par(7)
      dSdl = -0.5D0*kappa*r*rho*v1**2.D0

!Calculate drdl
      if (r == 0) then
dRRdl = 0.D0
else
dRRdl = 0.5D0*(T*S
      & + r*dSdl
      & + W*dSdl
      & - 2.D0*RR*S
      & - 1.D0
      & + S**2.D0
      &      + 0.5D0*kappa*rho*r**2.D0
      & - Llamba*r**2.D0)/r

      endif

!write(*,*) dRRdl

      end function

c -----
c Calculate dTdl
c -----

real*8 function dTdl(T, lambda, par)

      implicit none

!Parameters
      real*8, intent(in) :: lambda !Required for general ODE function
      real*8, intent(inout) :: T !Required for general ODE function
      real*8, intent(in) :: par(8)

!Local variables
      real*8, parameter :: PI = 3.141592653589793
      real*8 :: r, RR, S, W, v0, v1, rho, dSdl, dRRdl
real*8 :: kappa, Llamba, G, c
c = 2.999e8
G = 6.667e-11
kappa = 8.D0*PI !*G !/c**4.D0
!Llamba = -1.25e-2

```

```

!Extract parameters
r = par(1)
RR = par(2)
S = par(3)
T = par(4)
W = par(5)
v1 = par(6)
rho = par(7)
Llamba = par(8)

v0 = 0.5D0*((1.D0+W/r)*v1 + 1.D0/v1)

dSdl = -0.5D0*kappa*r*rho*v1**2.D0

dRRdl = 0.5D0*(T*S
& + r*dSdl
& + W*dSdl
& - 2.D0*RR*S
& - 1.D0
& + S**2.D0
& + 0.5D0*kappa*rho*r**2.D0
& - Llamba*r**2.D0)/r

!Calculate dTdl
if( r==0) then
dTdl = 0.D0
else
dTdl = W/r*dSdl
& + 4.D0*dRRdl
& + 2.D0*kappa*(v0*v1*rho*r
& - 0.5D0*rho*r)
& + 2.D0*Llamba*r
endif

end function

c -----
c Calculate dWdl
c -----

real*8 function dWdl(W, lambda, par)

implicit none

!Parameters
real*8, intent(in) :: lambda !Required for general ODE function
real*8, intent(in) :: W !Required for general ODE function
real*8, intent(in) :: par(7)

!Local variables
real*8 :: T

!Extract parameters
T = par(1)

```

```

!Calculate drdl
  dWdl = T

end function

c -----
c Calculate the value of v0
c -----

real*8 function v0eq(Vw, v1)

  implicit none

!Parameters
  real*8, intent(in) :: Vw, v1

  !Calculate v1 time derivative
v0eq = 1.DO/2.DO*Vw*v1
      & + 1.DO/2.DO*1.DO/v1

end function

c -----
c Calculate dv1du
c -----

real*8 function dv1du(Vw, dVwdl, v0, v1 ,dv1dl)

  implicit none

!Parameters
  real*8, intent(in) :: Vw, dVwdl
  real*8, intent(in) :: v0, v1 ,dv1dl

!write(*,*) Vw, dVwdl, v0, v1 ,dv1dl

  !Calculate v1 time derivative
dv1du = 1.DO/v1*((Vw*v1 - v0)*dv1dl
          & + 0.5D0*(v1**2.DO)*dVwdl)

end function

c -----
c Calculate drhodu
c -----

real*8 function drhodu(Vw, dVwdl, r, drdl, RR, v0, dv0dl
  & ,v1 ,dv1dl, rho, drhodl, dv1du)

  implicit none

!Parameters
  real*8, intent(in) :: Vw, dVwdl, r, drdl, RR
  real*8, intent(in) :: v0, dv0dl,v1 ,dv1dl, rho, drhodl

```

```

real*8, intent(in) :: dv1du

!Calculate rho time derivative
drhodu = 1.D0/v1*(rho*(
  & Vw*(2.D0*v1/r*drdl + dv1dl)
  & - (2.D0*v0/r*drdl + dv0dl)
  & + dVwdl*v1
  & - (2.D0*RR/r)*v1)
  & + (Vw*v1 - v0)*drhodl
  & - rho*dv1du)

end function

c -----
c Calculate dFdu using a series solution
c - the functions were generated with Maple
c -----
subroutine dFduser(r1, r2, r3, r4
  & , rhor1, rhor2, rhor3, rhor4
  & , v1r1, v1r2, v1r3, v1r4
  & , rho0u, rho1u, rho2u, rho3u
  & , v10u, v11u, v12u, v13u
  & , Llambda)

  implicit none

  real*8, intent(in) :: r1, r2, r3, r4
  real*8, intent(in) :: rhor1, rhor2, rhor3, rhor4
  real*8, intent(in) :: v1r1, v1r2, v1r3, v1r4
  real*8, intent(inout) :: rho0u, rho1u, rho2u, rho3u
  real*8, intent(inout) :: v10u, v11u, v12u, v13u
real*8, intent(in) :: Llambda

  real*8 :: rho0, rho1, rho2, rho3
  real*8 :: v10, v11, v12, v13
  real*8 :: v00, v01, v02, v03

!Local variables
  real*8, parameter :: PI = 3.141592653589793
  real*8 :: kappa

  kappa = 8.D0*PI

  rho0=rhor1

  rho1=-(-r2**2*rhor3+r2**2*rho0+rhor2*r3**2-rho
  #0*r3**2)/r2/r3/(-r3+r2)

  rho2=(rhor2*r3-rho0*r3-r2*rhor3+r2*rho0)/r2/r3
  #/(-r3+r2)

  v10=v1r1

  v11=-(-r2**3*r3**2*v1r4+r3**2*v1r1*r2**3-v1r

```

```

#1*r4**2*r2**3+v1r3*r4**2*r2**3-r3**3*v1r1
#r2**2+r2**2*r3**3*v1r4-v1r3*r4**3*r2**2+
#v1r1*r4**3*r2**2+r3**3*v1r1*r4**2-r3**3*v1
#r2*r4**2-r4**3*r3**2*v1r1+r4**3*r3**2*v1r2
#)/r2/r3/r4/(r2*r4**2-r2**2*r4+r3*r2**2-r
#3*r4**2+r3**2*r4-r3**2*r2)

v12=(-r4*r3**3*v1r2+r4*r3**3*v1r1+r3**3*r2*
#v1r4-r3**3*v1r1*r2+r3*v1r1*r2**3+r3*r4**3*
#v1r2-v1r1*r4**3*r3-r3*r2**3*v1r4-v1r3*r4**3*
#r2+v1r3*r4*r2**3-v1r1*r4*r2**3+v1r1*r4**3
#r2)/(-r4+r3)/r4/r3/(r3*r4-r3*r2+r2**2-r4
#r2)/r2

v13=-(-v1r3*r4**2*r2+v1r1*r4**2*r2+v1r3*r4*r
#2**2-v1r1*r4*r2**2-r2**2*r3*v1r4+r3*v1r1*r
#2**2+r3*v1r2*r4**2-r3**2*v1r2*r4-r3*v1r1*r
#4**2+r3**2*v1r1*r4+r2*r3**2*v1r4-r3**2*v1r
#1*r2)/r2/r3/r4/(r2*r4**2-r2**2*r4+r3*r2**
#2-r3*r4**2+r3**2*r4-r3**2*r2)

v10u = 0.D0

v11u=-v11**2-kappa*rho0/0.6D1-Llambd/0.3D1

v12u=-rho1*kappa/0.8D1+0.3D1/0.8D1*kappa*v11*rho0
#+0.10D2/0.3D1*0.3141592654D1*rho0*v11+v11u*v11-v11
***3/0.2D1-0.3D1*v11*v12+v11*Llambd

v13u=0.D0

rho0u=-3*rho0*v11

rho1u=-dble(6*rho0*v11**2)+dble(rho0**2*kappa)/0.2
#D1+dble(rho0*Llambd)-dble(4*rho0*v12)-0.8D1/0.3D1*
#dble(rho0**2)*0.3141592654D1-dble(4*rho1*v11)

rho2u=-0.7D1*0.3141592654D1*v11*rho0**2-0.5D1*v13*
#rho0+0.23D2/0.24D2*rho1*kappa*rho0-0.3D1/0.8D1*rho
#0**2*v11*kappa-0.15D2*v11*v12*rho0+0.4D1/0.3D1*
#rho1*Llambd-0.15D2/0.2D1*v11**2*rho1-0.10D2*v11*
#3*rho0-rho0*Llambd*v11-0.5D1*0.3141592654D1*rho0*
#rho1-0.5D1*v11*rho2-0.5D1*v12*rho1

rho3u=0.D0

end subroutine

c ===== =
c ROUTINES TO SOLVE THE HYPERSURFACE EQUATIONS OF THE AFFINE CIVP
c =====
c
c =====
c -----

```

```

c   Solve the differential equation for S using a centrel step
c   method.
c   -----

subroutine calcS(lambda, S, r, v1, rho, dell, NI, NJ, i)

  implicit none

  !Parameters
  integer, intent(in) :: NI, NJ, i
  real*8, intent(in) :: lambda(NJ), r(NI,NJ)
real*8, intent(in) :: rho(NI,NJ), v1(NI,NJ)
real*8, intent(in) :: dell
  real*8, intent(inout) :: S(NI,NJ)

  !Local variables
  real*8, parameter :: PI = 3.141592653589793
  integer :: j, p
  real*8 :: dSd1, dSd11, dSd12
  real*8 :: yp, par(7)

  !Initialise par
  do p=1,7
par(p) = 0.D0
  end do

  !Calculate S
  S(i,1) = 1.D0

  do j=2,NJ

par(1) = r(i,j-1)
  par(2) = v1(i,j-1)
par(3) = rho(i,j-1)
dSd11 = dSd1(S(i,j-1), lambda(j-1), par)

  par(1) = r(i,j)
  par(2) = v1(i,j)
par(3) = rho(i,j)
dSd12 = dSd1(S(i,j), lambda(j), par)

  S(i,j) = S(i,j-1) + 0.5D0*dell*(dSd11+dSd12)

  end do

  end subroutine

c   -----
c   Solve the differential equation for S and r alternating using
c   a centrel step method.
c   -----

subroutine calcSr(lambda, S, r, v1, rho, dell, NI, NJ, i)

  implicit none

```

```

!Parameters
integer, intent(in) :: NI, NJ, i
real*8, intent(in) :: lambda(NJ)
real*8, intent(in) :: rho(NI,NJ), v1(NI,NJ)
real*8, intent(in) :: dell
real*8, intent(inout) :: S(NI,NJ), r(NI,NJ)

!External routines
!external dSdl

!Local variables
real*8, parameter :: PI = 3.141592653589793
integer :: j, p, m
real*8 :: dSdl, dSdl1, dSdl2
real*8 :: drdl, drdl1, drdl2
real*8 :: yp, par1(7), par2(7), Sp, delS

!Initialise par
do p=1,7
par1(p) = 0.D0
par2(p) = 0.D0
end do

!Calculate S
S(i,1) = 1.D0

do j=2,NJ

par1(1) = r(i,j-1)
par1(2) = v1(i,j-1)
par1(3) = rho(i,j-1)
dSdl1 = dSdl(S(i,j-1), lambda(j-1), par1)

par2(1) = S(i,j-1)
drdl1 = drdl(r(i,j-1), lambda(j-1), par2)

do m=1,5

par1(1) = r(i,j)
par1(2) = v1(i,j)
par1(3) = rho(i,j)
dSdl2 = dSdl(S(i,j), lambda(j), par1)

S(i,j) = S(i,j-1) + 0.5D0*dell*(dSdl1+dSdl2)

par2(1) = S(i,j)
drdl2 = drdl(r(i,j), lambda(j), par2)

r(i,j) = r(i,j-1) + 0.5D0*dell*(drdl1+drdl2)

end do

end do

end subroutine

```

```

c      =====
c      -----
c      Solve the differential equation for r using a central step
c      method
c      -----

subroutine calcr(lambda, r, S, dell, NI, NJ, i)

  implicit none

  !Parameters
  integer, intent(in) :: NI, NJ, i
  real*8, intent(in) :: lambda(NJ), S(NI,NJ)
real*8, intent(in) :: dell
  real*8, intent(inout) :: r(NI,NJ)

  !External routines
  !external drdl

  !Local variables
  integer :: j, p
  real*8 :: drdl, drdl1, drdl2
  real*8 :: par(7)

  !Initialise par
    do p=1,7
par(p) = 0.D0
    end do

  !Calculate r
    r(i,1) = 0.D0

    do j=2,NJ
par(1) = S(i,j-1)
drdl1 = drdl(r(i,j-1), lambda(j-1), par)

par(1) = S(i,j)
drdl2 = drdl(r(i,j), lambda(j), par)

    r(i,j) = r(i,j-1) + 0.5D0*dell*(drdl1+drdl2)
    end do

  end subroutine

c      =====
c      -----
c      Solve the differential equations for R, T, W using a central step
c      method
c      -----

subroutine calcRRTW(lambda, RR, T, W, r, S, v1, rho, dell
  & , NI, NJ, i, Llambda)

```

```

implicit none

!Parameters
integer, intent(in) :: NI, NJ, i
real*8, intent(in) :: lambda(NJ), r(NI,NJ)
    real*8, intent(in) :: S(NI,NJ)
    real*8, intent(in) :: v1(NI,NJ), rho(NI,NJ)
real*8, intent(in) :: dell
    real*8, intent(inout) :: T(NI,NJ), RR(NI,NJ), W(NI,NJ)
real*8, intent(in) :: Llambda

!External routines
!external dTdl

!Local variables
real*8, parameter :: PI = 3.141592653589793
integer :: j, p, m
real*8 :: dRRdl, dRRdl1, dRRdl2
real*8 :: dTdl, dTdl1, dTdl2
real*8 :: dWdl, dWdl1, dWdl2
    real*8 :: par1(7), par2(8), par3(7)
real*8 :: rho0, rho1, v11, dfdr5

!Initialise par
    do p=1,7
par1(p) = 0.D0
par2(p) = 0.D0
par3(p) = 0.D0
    end do

par2(8) = 0.D0

!Calculate T
RR(i,1) = 0.D0
    T(i,1) = 0.D0
W(i,1) = 0.D0

do j=2,NJ

do m=1,5

par1(1) = r(i,j-1)
par1(2) = S(i,j-1)
par1(3) = T(i,j-1)
par1(4) = W(i,j-1)
    par1(5) = v1(i,j-1)
par1(6) = rho(i,j-1)
par1(7) = Llambda
dRRdl1 = dRRdl(RR(i,j-1), lambda(j-1), par1)

par1(1) = r(i,j)
par1(2) = S(i,j)
par1(3) = T(i,j)
par1(4) = W(i,j)
    par1(5) = v1(i,j)

```

```

par1(6) = rho(i,j)
par1(7) = Llambda
dRRd12 = dRRd1(RR(i,j), lambda(j), par1)

if (j < 1) then
RR(i,j)=-0.7073637596D-1*0.3141592654D1*lambda(j)**3
else
RR(i,j) = RR(i,j-1) + 0.5D0*de11*(dRRd11+dRRd12)
endif

par2(1) = r(i,j-1)
par2(2) = RR(i,j-1)
par2(3) = S(i,j-1)
par2(4) = T(i,j-1)
par2(5) = W(i,j-1)
par2(6) = v1(i,j-1)
par2(7) = rho(i,j-1)
par2(8) = Llambda
dTd11 = dTd1(T(i,j-1), lambda(j-1), par2)

par2(1) = r(i,j)
par2(2) = RR(i,j)
par2(3) = S(i,j)
par2(4) = T(i,j)
par2(5) = W(i,j)
par2(6) = v1(i,j)
par2(7) = rho(i,j)
par2(8) = Llambda
dTd12 = dTd1(T(i,j), lambda(j), par2)

T(i,j) = T(i,j-1) + 0.5D0*de11*(dTd11+dTd12)

par3(1) = T(i,j-1)
dWd11 = dWd1(W(i,j-1), lambda(j-1), par3)

par3(1) = T(i,j)
dWd12 = dWd1(W(i,j), lambda(j), par3)

if(j<1) then
W(i,j)=0.7073552906D
# -1*0.3141592654D1*lambda(j)**3+0.4715641081D
# -1*0.3141592654D1*lambda(j)**4
else
W(i,j) = W(i,j-1) + 0.5D0*de11*(dWd11+dWd12)
endif

end do

end do

end subroutine

c -----
c Calculate the incoming characteristic cut-off line.
c -----

```

```

subroutine calclmax(ljmax, lambda, delu, dell
  & , W, ni, nj, lmax)

implicit none

integer, intent(in) :: ni, nj
integer, intent(inout) :: ljmax(ni)
real*8, intent(in) :: lambda(nj), delu, dell, W(ni,nj)
real*8, intent(inout) :: lmax(ni)

real*8 :: lp, lprev, tol, Wp
integer :: i, jmax

tol = 1.0e-7
lp = lambda(nj)
lmax(1) = lambda(nj)
ljmax(1) = nj

do i=2,ni

!predict the lambda value
lp = lmax(i-1) - 0.5D0*delu
lprev = 0.D0

do while(abs(lp - lprev) > tol)

!store previous value
lprev = lp

!interpolate to the closest W value
jmax = lp/dell

if (jmax < 2) then
jmax = 2
endif

Wp = W(i,jmax)
  & + (lp-lambda(jmax))*(W(i,jmax-1)
  & - W(i,jmax))/dell

!correct the lambda value
lp = lmax(i-1) - 0.5D0*(1+Wp/lp)*delu

end do

lmax(i) = lp
ljmax(i) = jmax

end do

end subroutine

```

```

c -----
c Calculate the next step for the velocity and density using
c a finite difference iteration to the half step

```

```

c -----
subroutine calcCIVP(lambda, u, dell, delu
  & , r, W, v0, v1, rho, v1u
  & , NI, NJ, i, jmax
  & , lbmin, lbmax
  & , Llambda)

implicit none

!Subroutine parameters
real*8, intent(in) :: lambda(NJ), u(NI,NJ)
  real*8, intent(inout) :: r(NI,NJ), W(NI,NJ)
  real*8, intent(inout) :: v0(NI,NJ), v1(NI,NJ), rho(NI,NJ)
real*8, intent(inout) :: v1u(NI,NJ)
  real*8, intent(in) :: dell, delu
  integer, intent(in) :: NI, NJ, i, jmax
  real*8, intent(in) :: lbmin, lbmax, Llambda

!Local variables
integer :: j, m
real*8 :: Frho, Fv1, Frhop, Fv1p
  real*8 :: rp(NI,NJ), Wp(NI,NJ)
  real*8 :: S(NI,NJ), RR(NI,NJ), T(NI,NJ)
  real*8 :: Sp(NI,NJ), RRp(NI,NJ), Tp(NI,NJ)
real*8 :: vOp(NI,NJ), v1p(NI,NJ), rhop(NI,NJ)

real*8, parameter :: PI = 3.141592653589793D0

!Initialise local matter variables
do j=1,jmax
  rp(i,j) = r(i,j)
  rhop(i,j) = rho(i,j)
  v1p(i,j) = v1(i,j)
  RR(i,j) = 0.D0
    T(i,j) = 0.D0
    S(i,j) = 0.D0
    W(i,j) = 0.D0
  end do

!Calculate hypersurface variables on previous step

do m=1,5

call calcS(lambda, S, r, v1, rho, dell, NI, NJ, i)

call calcRRTW(lambda, RR, T, W, r, S, v1, rho, dell
  & , NI, NJ, i, Llambda)

  call calcv0(r, v0, v1, W
  & , NI, NJ, i, jmax, 1)

  end do

do j=1,jmax
  rp(i,j) = r(i,j)

```

```

Sp(i,j) = S(i,j)
RRp(i,j) = RR(i,j)
Wp(i,j) = W(i,j)
  Tp(i,j) = T(i,j)
v1p(i,j) = v1(i,j)
v0p(i,j) = v0(i,j)
  end do

  !Iterative loop
  do m=1,5

      call calcSr(lambda, Sp, rp, v1p, rhop, dell, NI, NJ, i)

call calcRRTW(lambda, RRp, Tp, Wp, rp, Sp, v1p, rhop, dell
  & , NI, NJ, i, Llambda)

call calcv0(rp, v0p, v1p, Wp
  & , NI, NJ, i, jmax, 1)

  do j=1,jmax

      !Calculate previous step's time derivatives
call dFdu(Frho, Fv1, dell
  & , lambda, r, W, S(i,j), RR(i,j), v0, v1, rho
  & , NI, NJ, j, i, jmax
  & , lbmin, lbmax, Llambda)

!Calculate predictor time derivatives
call dFdu(Frhop, Fv1p, dell
  & , lambda, rp, Wp, Sp(i,j), RRp(i,j), v0p, v1p, rhop
  & , NI, NJ, j, i, jmax
  & , lbmin, lbmax, Llambda)

!Calculate rho
rhop(i,j) = rho(i,j) + delu*0.5D0*(Frho + Frhop)

!Calculate v1
  v1p(i,j) = v1(i,j) + delu*0.5D0*(Fv1 + Fv1p)
v1u(i,j) = Fv1p

!Calculate r
  rp(i,j) = r(i,j) + delu*0.5D0*(RR(i,j) + RRp(i,j))

  end do

!stop

end do

!Update to the calculated time step
  do j=1,jmax
if (isnan(rhop(i,j))) then

```

```

rho(i+1,j) = rho(i,j)
v1(i+1,j) = v1(i,j)
r(i+1,j) = r(i,j)
else
rho(i+1,j) = rhop(i,j)
v1(i+1,j) = v1p(i,j)
r(i+1,j) = rp(i,j)
endif
end do

end subroutine

c -----
c Calculate the values of the velocity and density time derivatives
c -----
subroutine dFdu(Frho, Fv1, dell
& , lambdaa, ra, Wa, S, RR, v0a, v1a, rhoa
& , NI, NJ, j, i, jmax
& , lbmin, lbmax, Llambda)

implicit none

!Subroutine parameters
real*8, intent(inout) :: Frho, Fv1
real*8, intent(in) :: dell, lambdaa(NJ)
real*8, intent(in) :: ra(NI,NJ), Wa(NI,NJ), RR, S
real*8, intent(in) :: v0a(NI,NJ), v1a(NI,NJ), rhoa(NI,NJ)
integer, intent(in) :: NI, NJ, j, i, jmax
real*8, intent(in) :: lbmin, lbmax, Llambda

!Local variables
real*8 :: lambda, r, W, v0, v1, rho
real*8 :: dv0dl, dv1dl, drhodl, dv1du, drhodu
real*8 :: Vw, dVwdl, drdl, dWdl
real*8 :: dfdr5
real*8 :: rho0u, rho1u, rho2u, rho3u
real*8 :: v10u, v11u, v12u, v13u
real*8 :: bf

real*8, parameter :: PI = 3.141592653589793D0

integer :: ser

!Current point values
lambda = lambdaa(j)
r = ra(i,j)
drdl = S
W = Wa(i,j)
v0 = v0a(i,j)
v1 = v1a(i,j)
rho = rhoa(i,j)

!Matter derivatives from five-point formulae
dWdl = dfdr5(Wa, dell, i, j, NI, NJ, jmax)
dv1dl = dfdr5(v1a, dell, i, j, NI, NJ, jmax)
drhodl = dfdr5(rhoa, dell, i, j, NI, NJ, jmax)

```

```

!Calculate dVwdr
Vw = 1.D0 + W/r

      !Calculate dVwdr
      dVwdl = dWdl/r - W*drdl/(r**2.D0)

!dv0dr from derivative of the normiliased v0 equation
dv0dl = 0.5D0*dv1dl*Vw + 0.5D0*v1*dVwdl
      & - 0.5D0*dv1dl/(v1**2.D0)

!Series solution
if( lambda < lbmin ) then

call dFduser(lambdaa(1), lambdaa(2)
      & , lambdaa(3), lambdaa(4)
      & , rhoa(i,1), rhoa(i,2), rhoa(i,3), rhoa(i,4)
      & , v1a(i,1), v1a(i,2), v1a(i,3), v1a(i,4)
      & , rho0u, rho1u, rho2u, rho3u
      & , v10u, v11u, v12u, v13u, Llambda)

Fv1 = v10u + v11u*lambda + v12u*lambda**(2.D0)

Frho = rho0u + rho1u*lambda + rho2u*lambda**(2.D0)

ser = 0

endif

!Blended series solution
if (lambda>=lbmin .and. lambda<=lbmax) then

call dFduser(lambdaa(1), lambdaa(2)
      & , lambdaa(3), lambdaa(4)
      & , rhoa(i,1), rhoa(i,2), rhoa(i,3), rhoa(i,4)
      & , v1a(i,1), v1a(i,2), v1a(i,3), v1a(i,4)
      & , rho0u, rho1u, rho2u, rho3u
      & , v10u, v11u, v12u, v13u, Llambda)

!Calculate blend function
      bf = 0.5D0
      & + 0.5D0*tanh(
      & -5.D0+(lambda-lbmin)/(lbmax-lbmin)*10.D0)

!Calculate v1 time derivative
Fv1 = (1.D0-bf)
      & *(v10u + v11u*lambda + v12u*lambda**(2.D0))
      & + (bf)
      & *dv1du(Vw, dVwdl, v0, v1 ,dv1dl)

!Calculate rho time derivative
Frho = (1.D0-bf)
      & *(rho0u + rho1u*lambda + rho2u*lambda**(2.D0))
      & + (bf)
      & *drhodu(Vw, dVwdl, r, drdl, RR, v0, dv0dl
      & ,v1 ,dv1dl, rho, drhodl, Fv1)

```

```

ser = 1

endif

!CIVP solution
if (lambda>lbmax) then

!Calculate v1 time derivative
Fv1 = dv1du(Vw, dVwdl, v0, v1 ,dvidl)

!Calculate rho time derivative
Frho = drhodu(Vw, dVwdl, r, drdl, RR, v0, dv0dl
& ,v1 ,dvidl, rho, drhodl, Fv1)

ser = 2

endif

end subroutine

c -----
c Calculate v0
c -----

subroutine calcv0(r, v0, v1, W
& , NI, NJ, i, jmax, jser)

implicit none

!Parameters
integer, intent(in) :: NI, NJ, i, jmax, jser
real*8, intent(in) :: v1(NI,NJ), W(NI,NJ), r(NI,NJ)
real*8, intent(inout) :: v0(NI,NJ)

!Local variables
integer :: j
real*8 :: Vw, v0eq

do j=1,jmax
if (r(i,j)==0) then
v0(i,j) = -1.D0
else
Vw = 1.D0 + W(i,j)/r(i,j)
v0(i,j) = v0eq(Vw, v1(i,j))
endif
end do

end subroutine

c =====
c GENERAL SUPPORT ROUTINES FOR AFFINE CIVP
c =====

```

```

c -----
c Calculate radial derivatives using a 5-point stencil
c -----
real*8 function dfdr5(f, h, i, j, NI, NJ, jmax)

  implicit none
  real*8, intent(in) :: f(NI,NJ), h
  integer, intent(in) :: i, j, NI, NJ, jmax
  character :: method

  if (j < 3) then
    method = 'l'
  endif

  if (j >= 3 .and. j < jmax-2) then
    method = 'm'
  endif

  if (j >= jmax-2) then
    method = 'r'
  endif

  if (method == 'l') then

    dfdr5 = (-25.D0*f(i,j) + 48.D0*f(i,j+1)
      & - 36.D0*f(i,j+2) + 16.D0*f(i,j+3)
      & - 3.D0*f(i,j+4))
      & /(12.D0*h)

  endif

  if (method == 'm') then

    dfdr5 = (f(i,j-2) - 8.D0*f(i,j-1)
      & + 8.D0*f(i,j+1) - f(i,j+2))
      & /(12.D0*h)
  endif

  if (method == 'r') then

    dfdr5 = -(-25.D0*f(i,j) + 48.D0*f(i,j-1)
      & - 36.D0*f(i,j-2) + 16.D0*f(i,j-3)
      & - 3.D0*f(i,j-4))
      & /(12.D0*h)

  endif

end function

c =====
c ROUTINES TO READ CONFIG AND INITIAL DATE AND WRITE RESULTS
c =====
c -----

```

```

c  Read config data file
c  -----

subroutine readConfig(NI, NJ, LLambda)

  implicit none

  !Subroutine parameters
  integer, intent(inout) :: NI, NJ
  real*8, intent(inout) :: LLambda

  !Local variables
  integer :: i,j

  open(1,file='data\grid.in')

  read(1,*) NI, NJ
  read(1,*) LLambda

  close(1)

end subroutine

c  -----
c  Read input data file
c  -----

subroutine readInitData(rI, v1I, rhoI
  & , NJ)

  implicit none

  !Subroutine parameters
  integer, intent(in) :: NJ
  real*8, intent(inout) :: rI(NJ), v1I(NJ), rhoI(NJ)

  !Local variables
  integer :: i,j,k

  k = 1

  open(1,file='data\affine.init.in')
  do j=1,NJ

  read(1,"(E23.16,2E25.16)")
    & rI(j), v1I(j), rhoI(j)

  end do

  close(1)

end subroutine

c  -----
c  Read known data file
c  -----

```

```

subroutine readGridData(lambda, u
    & , NI, NJ)

    implicit none

    !Subroutine parameters
    integer, intent(in) :: NI, NJ
    real*8, intent(inout) :: lambda(NJ), u(NI,NJ)

    !Local variables
    integer :: i,j,k

    k = 1

    open(1,file='data\affine.grid.in')
    do i=1,NI
    do j=1,NJ

    read(1,"(E23.16,E25.16)")
        & lambda(j), u(i,j)

    end do
    end do

    close(1)

end subroutine

c -----
c Read known data file
c -----

subroutine readRadialMax(ljmax, NI)

    implicit none

    !Subroutine parameters
    integer, intent(in) :: NI
    integer, intent(inout) :: ljmax(NI)

    !Local variables
    integer :: i, io, ri
    real :: r

    open(1,file='data\affine.lmax.in')
    do i=1,NI
    read(1,*,iostat=io) ljmax(i)
    end do

    close(1)

end subroutine

c -----
c Read known data file

```

```

c -----
subroutine readKnownData(rE, WE, vOE, v1E, rhoE
    & , NI, NJ)

    implicit none

    !Subroutine parameters
    integer, intent(in) :: NI, NJ
    !real*8, intent(inout) :: lambda(NJ), u(NI,NJ)
    real*8, intent(inout) :: rE(NI,NJ), WE(ni,nj)
    real*8, intent(inout) :: VOE(NI,NJ), v1E(NI,NJ), rhoE(NI,NJ)

    !Local variables
    integer :: i,j,k
    real*8 :: lambda, u

    k = 1

    open(1,file='data\affine.known.in')
    do i=1,NI
    do j=1,NJ
    read(1,"(E23.16,2E24.16,3E25.16)")
        & lambda, u, rE(i,j)
        & , vOE(i,j), v1E(i,j), rhoE(i,j)
    end do
    end do

    close(1)

end subroutine

c -----
c Read blend range
c -----

subroutine readBlendRange(lbmin, lbmax)

    implicit none
    real*8, intent(inout) :: lbmin, lbmax

    open(10,file='data\blend.in')

    read(10,*) lbmin, lbmax

    close(10)

end subroutine

c -----
c Write the results in an output file
c -----

subroutine writeResults(lambda, u, dell, delu
    & , r, W, v0, v1, rho, v1u

```

```

& , NI, NJ
& , ljmax, lmax)

implicit none

!Parameters
integer, intent(in) :: NI, NJ, ljmax(NI)
real*8, intent(in) :: lambda(NJ), u(NI,NJ)

    real*8, intent(in) :: r(NI,NJ), W(NI,NJ)
    real*8, intent(in) :: v0(NI,NJ), v1(NI,NJ), rho(NI,NJ)
real*8, intent(in) :: v1u(NI,NJ)

    real*8 :: rE(NI,NJ), WE(NI,NJ)
    real*8 :: vOE(NI,NJ), v1E(NI,NJ), rhoE(NI,NJ)

real*8, intent(in) :: delu, dell
real*8, intent(in) :: lmax(NI)

!Local variables
integer :: p1, p2, p3, writefreq

!Read the known data to compare results with
call readKnownData(rE, WE, vOE, v1E, rhoE
& , NI, NJ)

!Trend data parameters
p1 = 2 !NI/100
p2 = NI/2
p3 = NI-1

!Write every NJ/100th value
if (NJ>=51) then
    writefreq = 1 !NJ/51
else
writefreq = 1
endif

!Trend data .dat
call writeResultsDAT(lambda, u, dell, delu
& , r, W, v0, v1, rho, v1u
& , rE, WE, vOE, v1E, rhoE
& , NI, NJ
& , ljmax, lmax
& , p1, p2, p3, writefreq)

end subroutine

c -----
c Routines for output formats
c -----

subroutine writeResultsDAT(lambda, u, dell, delu
& , r, W, v0, v1, rho, v1u
& , rE, WE, vOE, v1E, rhoE

```

```

& , NI, NJ
& , ljmax, lmax
& , p1, p2, p3, writefreq)

implicit none

!Parameters
integer, intent(in) :: NI, NJ, ljmax(NI)
real*8, intent(in) :: lambda(NJ), u(NI,NJ)

real*8, intent(in) :: r(NI,NJ), W(NI,NJ)
real*8, intent(in) :: v0(NI,NJ), v1(NI,NJ), rho(NI,NJ)
real*8, intent(in) :: v1u(NI,NJ)

real*8, intent(in) :: rE(NI,NJ), WE(NI,NJ)
real*8, intent(in) :: v0E(NI,NJ), v1E(NI,NJ), rhoE(NI,NJ)

real*8, intent(in) :: delu, dell
integer, intent(in) :: p1, p2, p3, writefreq

real*8, intent(in) :: lmax(NI)

!Local variables
integer :: i,j, ep
real*8 :: zero, rmax, umax, rhomax, rhoav, error
real*8 :: mu, muE, dL, dLE, z, zE

zero = 0.0

!Beta Trend data

write(*,*) ' + 1. Writing r-trend data...'

open(1,file='data\plot\a.r1.dat')

do j=1,NJ
if(mod(j,writefreq) == 0) then
if (abs(rE(p1,j)) > 0.DO) then
write(1,*) lambda(j), r(p1,j), rE(p1,j)
end if
end if
end do

close(1)

open(1,file='data\plot\a.r2.dat')

do j=1,NJ
if(mod(j,writefreq) == 0) then
if (abs(rE(p2,j)) > 0.DO) then
write(1,*) lambda(j), r(p2,j), rE(p2,j)
end if
end if
end do

close(1)

```

```

open(1,file='data\plot\a.r3.dat')

do j=1,NJ
if(mod(j,writefreq) == 0) then
if (abs(rE(p3,j)) > 0.D0) then
write(1,*) lambda(j), r(p3,j), rE(p3,j)
end if
end if
end do

close(1)

!Write rho data

write(*,*) ' + 3. Writing rho trend data...'

open(1,file='data\plot\c.rho1.dat')

do j=1,NJ-1 !ljmax(p1)
if(mod(j,writefreq) == 0) then
if (abs(rho(p1,j)) < 5.D0) then
write(1,*) lambda(j), rho(p1,j), rhoE(p1,j)
end if
end if
end do

close(1)

open(1,file='data\plot\c.rho2.dat')

do j=1,NJ !ljmax(p2)
if(mod(j,writefreq) == 0) then
if (abs(rho(p2,j)) < 5.D0 .and. rhoE(p2,j).NE.0.D0) then
write(1,*) lambda(j), rho(p2,j), rhoE(p2,j)
end if
end if
end do

close(1)

open(1,file='data\plot\c.rho3.dat')

do j=1,NJ !ljmax(p3)
if(mod(j,writefreq) == 0) then
if (abs(rho(p3,j)) < 5.D0 .and. rhoE(p3,j).NE.0.D0) then
write(1,*) lambda(j), rho(p3,j), rhoE(p3,j)
end if
end if
end do

close(1)

!v1 Trend data

```

```

write(*,*) ' + 4. Writing v1 dat trend data'

open(1,file='data\plot\d.v11.dat')

do j=1,NJ
    if(mod(j,writfreq) == 0) then
if (abs(v1E(p1,j)) > 0.D0) then
write(1,*) lambda(j), v1(p1,j), v1E(p1,j)
end if
    end if
end do

close(1)

open(1,file='data\plot\d.v12.dat')

do j=1,NJ
    if(mod(j,writfreq) == 0) then
if (abs(v1E(p2,j)) > 0.D0) then
write(1,*) lambda(j), v1(p2,j), v1E(p2,j)
end if
    end if
end do

close(1)

open(1,file='data\plot\d.v13.dat')

do j=1, NJ
    if(mod(j,writfreq) == 0) then
if (abs(v1E(p3,j)) > 0.D0) then
write(1,*) lambda(j), v1(p3,j), v1E(p3,j)
end if
    end if
end do

close(1)

!Write rho error

write(*,*) ' + 5. Writing error trend data...'

    open(1,file='data\plot\e.err3.rho.dat')

        do j=1,NJ !ljmax(p3)
if (abs(rho(p3,j)) < 5.D0 .and. rhoE(p3,j).NE.0.D0) then
write(1,*) lambda(j)
    & , 100*abs(rho(p3,j) - rhoE(p3,j))/rho(p3,j)
end if

        end do

close(1)

    open(1,file='data\plot\e.err3.rho.csv')

```

```

        do j=1,NJ !ljmax(p3)
if (abs(rho(p3,j)) < 5.D0 .and. rhoE(p3,j).NE.0.D0) then
write(1,*) lambda(j), ', '
    & , 100*abs(rho(p3,j) - rhoE(p3,j))/rho(p3,j)
end if

        end do

        close(1)

! v1 error

open(1,file='data\plot\e.err3.v1.dat')

        do j=1,NJ !ljmax(p3)
if (abs(v1(p3,j)) < 8.D0 .and. v1E(p3,j).NE.0.D0) then
write(1,*) lambda(j)
    & , 100*abs(v1(p3,j) - v1E(p3,j))/abs(v1(p3,j))
end if

        end do

        close(1)

! z error

open(1,file='data\plot\e.err3.z.dat')

        do j=1,NJ !ljmax(p3)
if (abs(v1(p3,j)) < 8.D0 .and. v1E(p3,j).NE.0.D0) then
z = abs(1.D0+v1(p3,j))
zE = abs(1.D0+v1E(p3,j))
write(1,*) lambda(j)
    & , 100*abs(z - zE)/abs(z)
end if

        end do

        close(1)

! r error

open(1,file='data\plot\e.err3.r.dat')

        do j=1,NJ !ljmax(p3)
if ((rE(p1,j)) > 0.D0) then
write(1,*) lambda(j)
    & , 100*abs(r(p3,j) - rE(p3,j))/abs(r(p3,j))
end if

        end do

        close(1)

open(1,file='data\plot\f.rz1.dat')

```

```

        do j=1,NJ
          if(mod(j,writefreq) == 0) then
            if (abs(rE(p1,j)) > 0.D0) then
              write(1,*) abs(1.D0+v1(p1,j))
                & , abs(1.D0+v1E(p1,j))
                & , r(p1,j)
                & , rE(p1,j)
            end if
          end if
        end do

        close(1)

        open(1,file='data\plot\f.rz2.dat')

        do j=1,NJ
          if(mod(j,writefreq) == 0) then
            if (abs(rE(p2,j)) > 0.D0) then
              write(1,*) abs(1.D0+v1(p2,j))
                & , abs(1.D0+v1E(p2,j))
                & , r(p2,j)
                & , rE(p2,j)
            end if
          end if
        end do

        close(1)

        open(1,file='data\plot\f.rz3.dat')

        do j=1,NJ
          if(mod(j,writefreq) == 0) then
            if (abs(rE(p3,j)) > 0.D0) then
              write(1,*) abs(1.D0+v1(p3,j))
                & , abs(1.D0+v1E(p3,j))
                & , r(p3,j)
                & , rE(p3,j)
            end if
          end if
        end do

        close(1)

        end subroutine

```

# Appendix D

## Scilab code

The Scilab code is used to generate the input data for the Fortran code. This includes the grid definition, the initial values and the known solutions. The code listed here is the routines to generate EdS, bang-time LTB and  $\Lambda$ CDM data using numerical solutions of the transformations described in Section 3.2.4.

### D.1 Einstein-de Sitter transformation

```
clear();
lines(0);
warning('off')
format('v',20);

//Caclulate geodesic curve
function dydl = F(lambda,y)
    dydl(1) = y(3);
    dydl(2) = y(4);
    dydl(3) = -2/3*y(1)^(1/3)*y(4)^2;
    dydl(4) = -4/3*y(1)^(-1)*y(3)*y(4);
endfunction

//Setup grid resolution
NI = 500;
NJ = 100;

localdir = 'data/';

//Setup physical region
umin = 1;
lmin = 0;
umax = 0.35;
lmax = 0.597;

//Determine grid size
delu = abs(umin-umax)/(NI-1);
dell = abs(lmax-lmin)/(NJ-1);

u = umin:-delu:umax;
lambda = lmin:dell:lmax;
```

```

//Write to file 1
fd_w1 = mopen(localdir + 'affine.init.in','wt');
format1 = '%6.16e %6.16e %6.16e\n'

//Write to file 2
fd_w2 = mopen(localdir + 'affine.grid.in','wt');
format2 = '%6.16e %6.16e\n'

//Write to file 3
fd_w3 = mopen(localdir + 'affine.known.in','wt');
format3 = '%6.16e %6.16e %6.16e %6.16e %6.16e %6.16e\n'

//Write to file 4
fd_w4 = mopen(localdir + 'affine.lmax.in','wt');
format4 = '%i\n'

//Write to file 5
fd_w5 = mopen(localdir + 'affine.init.err.in','wt');
format5 = '%6.16e %6.16e %6.16e %6.16e\n'

printf('Solving system ...\n');
printf('-----\n');
t1 = clock();

for i=1:NI

    //Initial data
    t0 = u(i);

    y0(1) = t0;           //t(0)=1
    y0(2) = 0;           //r(0) = 0
    y0(3) = -1;         //dt/dlambda = -1
    y0(4) = t0^(-2/3);   //dr/dlambda = t(0)^(-2/3)
    lambda0 = 0;

    //Solve ODEs
    y = ode(y0, lambda0, lambda, F);

    //Calculate r
    t = y(1,:);          //t (comoving)
    x = y(2,:);          //x (r-comoving)
    rv = x.*t.^(2/3);    //Diameter distance
    v1v = y(3,:);        //dt/dlambda = v1
    rlv = y(4,:);        //dr/dlambda (not used)

    rhov = 1 ./ (6*pi*t.^2);

    //Pad v1 data with 0 to get consistent vector sizes
    v1n = size(v1v);

    if (v1n(2) < NJ) then
        n = NJ-v1n(2);
        v1z = linspace(0,0,n);
        v1 = [v1v,v1z];
    else

```

```

    v1 = v1v;
end

//Pad rho data with 0 to get consistent vector sizes
rhon = size(rhov);

if (rhon(2) < NJ) then
    n = NJ-rhon(2);
    rhoz = linspace(0,0,n);
    rho = [rhov,rhoz];
else
    rho = rhov;
end

//Pad r data with 0 to get consistent vector sizes
rn = size(rv);

if (rn(2) < NJ) then
    n = NJ-rn(2);
    rz = linspace(0,0,n);
    r = [rv,rz];
else
    r = rv;
end

//Replace large rho and v1 values with 0
//Not necessary but was relevant for some
//simulations
for j=1:NJ
    if (rho(j)>9) then
        rho(j) = 0;
    end

    if (v1(j)<-9) then
        v1(j) = 0;
    end
end

ljmax = NJ;

//Determine the index of the extent of rho
for j=1:NJ
    if (rho(j) == 0) then
        ljmax = j;
        break;
    end
end

//Generate random error

//Write initial data to file
if (i == 1) then

    //Generate random errors
    rerrz = grand(NJ,1,"nor",0,0.05)+1;
    rerrr = grand(NJ,1,"nor",0,0.05)+1;

```

```

rerrrho = grand(NJ,1,"nor",0,0.05)+1;

for j=1:NJ
    z = -v1(j)-1;
    //vlerr = -(1.0 + 1.2*z)
    vlerr = -(1.0 + rerrz(j)*z)
//    mfprintf(fd_w1,format1, 1.2*r(j), vlerr, 1.2*rho(j));
    mfprintf(fd_w1,format1, rerrr(j)*r(j), vlerr, rerrrho(j)*rho(j));
    mfprintf(fd_w5,format5, lambda(j), rerrr(j), rerrz(j), rerrrho(j));
end
end

//Write grid data to file
for j=1:NJ
    mfprintf(fd_w2,format2,lambda(j),u(i));
end

//Write known data to file
for j=1:NJ
    mfprintf(fd_w3,format3,lambda(j),u(i),r(j),v1(j),v1(j),rho(j));
end

//Write known data to file
mfprintf(fd_w4,format4,ljmax);

end

mclose(fd_w1);
mclose(fd_w2);
mclose(fd_w3);
mclose(fd_w4);
mclose(fd_w5);

t2 = clock();
e = etime(t2,t1);

//Report on computation parameters
printf('\n=====\n');
printf(' Solution parameters \n');
printf('-----\n');
printf('Elapsed time (min): %2.3f\n', e/60);
printf('-----\n');
printf('NI = %2.f\n', NI);
printf('NJ = %2.f\n', NJ);
printf('umin = %2.16f\n', umin);
printf('umax = %2.16f\n', umax);
printf('lmin = %2.16f\n', lmin);
printf('lmax = %2.16f\n', lmax);
printf('dellambda/delu = %2.16f\n', dell/delu);
printf('=====');

```

## D.2 LTB transformation

```
clear();
lines(0);
warning('off')
format('v',20);

function dydl = F(lambda,y)

    t = y(1);
    r = y(2);
    f = y(3);
    g = y(4);

    dydl(1) = f;
    dydl(2) = g;

    dydl(3) = -2/27*(-3*t+5*b*r)*(-3*t+2*b*r) ..
              /((t-b*r)^(5/3)) *g^2;

    dydl(4) = -2/3*b*(5*b*r-6*t) ..
              /((-t+b*r)*(-3*t+5*b*r)) *g^2..
              + 4/3*(2*b*r-3*t) ..
              /((-t+b*r)*(-3*t+5*b*r)) *f*g;

endfunction

//Setup grid resolution
NI = 500;
NJ = 100;

b = -0.5;

localdir = 'E:/a.civp/code/affine/scilab/a.ltb/data/';

//Setup physical region
umin = 1;
lmin = 0;
umax = 0.2;
lmax = 0.98;

//Determine grid size
delu = abs(umin-umax)/(NI-1);
dell = abs(lmax-lmin)/(NJ-1);

u = umin:-delu:umax;
lambda = linspace(lmin,lmax,NJ);

//Write to file 1
fd_w1 = mopen(localdir + 'affine.init.in','wt');
format1 = '%6.16e %6.16e %6.16e\n'

//Write to file 2
fd_w2 = mopen(localdir + 'affine.grid.in','wt');
format2 = '%6.16e %6.16e\n'

//Write to file 3
```

```

fd_w3 = mopen(localdir + 'affine.known.in', 'wt');
format3 = '%6.16e %6.16e %6.16e %6.16e %6.16e %6.16e\n'

//Write to file 4
fd_w4 = mopen(localdir + 'affine.lmax.in', 'wt');
format4 = '%i\n'

printf('Solving system ...\n');
printf('-----\n');
t1 = clock();

for i=1:NI

    t0 = u(i);

    y0(1) = t0;
    y0(2) = 0;
    y0(3) = -1;
    y0(4) = t0^(-2/3);
    lambda0 = 0;

    y = ode(y0, lambda0, lambda, F);

    t = y(1,:);
    x = y(2,:);
    rv = x.*(t-b*x).^(2/3);
    v1v = y(3,:);

    rhov = 1 ./ (2*pi*(t-b*x).*(3*t-5*b*x));

    v1n = size(v1v);

    if (v1n(2) < NJ) then
        n = NJ-v1n(2);
        v1z = linspace(0,0,n);
        v1 = [v1v,v1z];
    else
        v1 = v1v;
    end

    rhon = size(rhov);

    if (rhon(2) < NJ) then
        n = NJ-rhon(2);
        rhoz = linspace(0,0,n);
        rho = [rhov,rhoz];
    else
        rho = rhov;
    end

    rn = size(rv);

    if (rn(2) < NJ) then
        n = NJ-rn(2);
        rz = linspace(0,0,n);
        r = [rv,rz];

```

```

else
    r = rv;
end

tn = size(t);

if (tn(2) < NJ) then
    n = NJ-tn(2);
    tz = linspace(0,0,n);
    tt = [t,tz];
else
    tt = t;
end

xn = size(x);

if (xn(2) < NJ) then
    n = NJ-xn(2);
    xz = linspace(0,0,n);
    xx = [x,xz];
else
    xx = x;
end

//z = t.^(-2/3)-1;

for j=1:NJ
    if (rho(j)>9) then
        rho(j) = 0;

    end

    if (v1(j)<-9) then
        v1(j) = 0;
    end

end

ljmax = NJ;

//Determine the index of the extent of rho
for j=1:NJ
    if (rho(j) == 0) then
        ljmax = j;
        break;
    end
end

//Write initial data to file
if (i == 1) then
    for j=1:NJ
        z = -v1(j)-1;
        vlerr = -(1.0 + 1.2*z)
        fprintf(fd_w1,format1, r(j), v1(j), rho(j));
    end
end

```

```

end

//Write grid data to file
for j=1:NJ
    mfprintf(fd_w2,format2,lambda(j),u(i));
end

//Write known data to file
for j=1:NJ
    mfprintf(fd_w3,format3,lambda(j),u(i),r(j),v1(j),v1(j),rho(j));
end

//Write known data to file
mfprintf(fd_w4,format4,ljmax);

end

fclose(fd_w1);
fclose(fd_w2);
fclose(fd_w3);
fclose(fd_w4);

t2 = clock();
e = etime(t2,t1);

//Report on computation parameters
printf('\n=====');
printf(' Solution parameters \n');
printf('-----\n');
printf('Elapsed time (min): %2.3f\n', e/60);
printf('-----\n');
printf('NI          = %2.f\n', NI);
printf('NJ          = %2.f\n', NJ);
printf('umin        = %2.16f\n', umin);
printf('umax        = %2.16f\n', umax);
printf('lmin        = %2.16f\n', lmin);
printf('lmax        = %2.16f\n', lmax);
printf('delr/delu = %2.16f\n', dell/delu);
printf('=====');

```

## D.3 $\Lambda$ CDM transformation

```
clear();
lines(0);
warning('off')
format('v',20);

//Function to solve the coordinates of a affine geodesic
// for the LCDM model

function dydl = F(lambda,y)

    t = y(1);
    r = y(2);
    f = y(3);
    g = y(4);

    dydl(1) = f;
    dydl(2) = g;

    dydl(3) = -(Om/Ol)^(2/3)*(sinh(3/2*Ho*sqrt(Ol)*t))^(1/3) ..
        * cosh(3/2*Ho*sqrt(Ol)*t)*(Ho)*sqrt(Ol) ..
        *g^2;

    dydl(4) = -2*cosh(3/2*Ho*sqrt(Ol)*t)*(Ho)*sqrt(Ol)..
        / sinh(3/2*Ho*sqrt(Ol)*t) ..
        *f*g;

endfunction

//Setup grid resolution
NI = 50;
NJ = 10;

//Set the physical parameters
Ol = 0.7;
Om = 0.3;
Ho = 72
//Ho = 2/3*(sqrt(Ol))^(1/2)*asinh((Ol/Om)^(1/2));
t00 = 2/3*(Ho*sqrt(Ol))^(1/2)*asinh((Ol/Om)^(1/2));
G = 6.667e-11;
c = 2.999e8;

rhom = 3*Ho^2*Om/(8*pi*G);
rhoc = rhom/Om;
rhol = Ol/Om*rhom;
kappa = 8*pi*G/c^4;
Lambda = rhol*kappa;

//Set boundaries
umin = 1;
lmin = 0;
umax = //0.4; //0.4*umin;
lmax = 0.549;

//Determine grid size
```

```

delu = abs(umin-umax)/(NI-1);
dell = abs(lmax-lmin)/(NJ-1);

printf('Solving system ...\n');
printf('-----\n');
t1 = clock();

//Calculate grid
u = umin:-delu:umax;
lambda = linspace(lmin,lmax,NJ); //lmin:dell:lmax;

//Setup file parameters
localdir = 'data/';

//Write to file 1
fd_w1 = mopen(localdir + 'affine.init.in','wt');
format1 = '%6.16f %6.16f %6.16f\n';

//Write to file 2
fd_w2 = mopen(localdir + 'affine.grid.in','wt');
format2 = '%6.16f %6.16f\n';

//Write to file 3
fd_w3 = mopen(localdir + 'affine.known.in','wt');
format3 = '%6.16f %6.16f %6.16f %6.16f %6.16f %6.16f\n';

//Write to file 4
fd_w4 = mopen(localdir + 'affine.lmax.in','wt');
format4 = '%i\n';

size(u)

for i=1:NI

    //Set initial values
    t0 = u(i);
    lambda0 = 0;

    y0(1) = t0;
    y0(2) = 0;
    y0(3) = -1;
    y0(4) = 1/((0m/0l)^(1/3)*(sinh(3/2*Ho*sqrt(0l)*t0))^(2/3));

    //Solve ODE
    y = ode('stiff', y0, lambda0, lambda, F);

    //Extract values from results
    t = y(1,:);
    x = y(2,:);
    v1v = y(3,:);

    //Calculate the expansion function
    S = (0m/0l)^(1/3)*(sinh(3/2*Ho*sqrt(0l)*t))^(2/3);

    //Calculate the diameter distance
    rv = x.*S;

```

```

//Calculate the density
rhov = 3*Ho^2/(8*pi*G)*Om ./ (S.^3);

//Pad v1 data with 0 to get consistent vector sizes
v1n = size(v1v);
if (v1n(2) < NJ) then
    n = NJ-v1n(2);
    v1z = linspace(0,0,n);
    v1 = [v1v,v1z];
else
    v1 = v1v;
end

//Pad rho data with 0 to get consistent vector sizes
rhon = size(rhov);
if (rhon(2) < NJ) then
    n = NJ-rhon(2);
    rhoz = linspace(0,0,n);
    rho = [rhov,rhoz];
else
    rho = rhov;
end

//Pad r data with 0 to get consistent vector sizes
rn = size(rv);
if (rn(2) < NJ) then
    n = NJ-rn(2);
    rz = linspace(0,0,n);
    r = [rv,rz];
else
    r = rv;
end

//Replace large rho and v1 values with 0
//Not necessary but was relevant for some
//simulations
for j=1:NJ
    if (rho(j)>9) then
        rho(j) = 0;
    end
    if (v1(j)<-9) then
        v1(j) = 0;
    end
end

ljmax = NJ;

//Determine the index of the extent of rho
for j=1:NJ
    if (rho(j) == 0) then
        ljmax = j;
        break;
    end
end
end

```

```

//Write initial data to file
if (i == 1) then
    for j=1:NJ
        fprintf(fd_w1,format1, r(j), v1(j), rho(j));
    end
end

//Write grid data to file
for j=1:NJ
    fprintf(fd_w2,format2,lambda(j),u(i));
end

//Write known data to file
for j=1:NJ
    fprintf(fd_w3,format3,lambda(j),u(i),r(j),v1(j),v1(j),rho(j));
end

//Write known data to file
fprintf(fd_w4,format4,ljmax);

end

fclose(fd_w1);
fclose(fd_w2);
fclose(fd_w3);
fclose(fd_w4);

t2 = clock();
e = etime(t2,t1);

disp((0m/0l)^(1/3)*(sinh(3/2*Ho*sqrt(0l)))^(2/3))

//Report on computation parameters
printf('\n===== \n');
printf(' Solution parameters \n');
printf('----- \n');
printf('Elapsed time (min): %2.3f \n', e/60);
printf('----- \n');
printf('NI          = %2.f \n', NI);
printf('NJ          = %2.f \n', NJ);
printf('Ho          = %2.16f \n', Ho);
printf('rhoc       = %2.16e \n', rhoc);
printf('rhol       = %2.16e \n', rhol);
printf('rhom       = %2.16e \n', rhom);
printf('Lambda     = %2.16f \n', Lambda);
printf('umin       = %2.16f \n', umin);
printf('umax       = %2.16f \n', umax);
printf('lmin       = %2.16f \n', lmin);
printf('lmax       = %2.16f \n', lmax);
printf('delr/delu = %2.16f \n', dell/delu);
printf('=====');

```

# Bibliography

- [1] V. V. L. Albani, A. S. Iribarrem, M. B. Ribeiro, and W. R. Stoeger. Differential Density Statistics of the Galaxy Distribution and the Luminosity Function. *Astrophys. J.*, 657:760–772, 2007.
- [2] D. A. Anderson, J. C. Tannehill, and R. H Pletcher. *Computational Fluid Mechanics and Heat Transfer*. Hemisphere Publishing Corporation, first edition, 1984.
- [3] M. E. Araújo and W. R. Stoeger. Exact spherically symmetric dust solution of the field equations in observational coordinates with cosmological data functions. *Phys. Rev. D*, 60(10):104020–+, 1999.
- [4] M. E. Araújo and W. R. Stoeger. Obtaining the time evolution for spherically symmetric Lemaitre-Tolman-Bondi models given data on our past light cone. *Phys. Rev. D*, 80(12):123517–+, 2009.
- [5] M. E. Araújo and W. R. Stoeger. The angular-diameter distance maximum and its redshift as constraints on  $\Lambda \neq 0$  Friedmann-Lemaitre-Robertson-Walker models. *Mon. Not. Roy. Astr. Soc.*, 394:438–442, 2009.
- [6] M. E. Araújo and W. R. Stoeger. Using time drift of cosmological redshifts to find the mass-energy density of the Universe. *Phys. Rev. D*, 82(12):123513–+, 2010.
- [7] M. E. Araújo and W. R. Stoeger. Finding a spherically symmetric cosmology from observations in observational coordinates – advantages and challenges. *JCAP*, 7:29–+, 2011.
- [8] B. A. Bassett and M. Kunz. Cosmic Acceleration versus Axion-Photon Mixing. *Astrophys. J.*, 607:661–664, 2004.
- [9] N. T. Bishop. Numerical relativity: combining the Cauchy and characteristic initial value problems. *Class. Quantum Grav.*, 10:333–341, 1993.
- [10] N. T. Bishop, R. Gómez, L. Lehner, M. Maharaj, and J. Winicour. High-powered gravitational news. *Phys. Rev. D*, 56:6298–6309, 1997.
- [11] N. T. Bishop, R. Gómez, L. Lehner, M. Maharaj, and J. Winicour. Incorporation of matter into characteristic numerical relativity. *Phys. Rev. D*, 60(2):024005–+, 1999.
- [12] N.T. Bishop and P. Haines. Observational Cosmology and Numerical Relativity. *Quaest. Math.*, 19:259–274, 1996.
- [13] K. Bolejko, A. Krasinski, C. Hellaby, and M.-N. Célérier. *Structures in the Universe by Exact Methods: Formation, Evolution, Interactions*. Cambridge University Press, first edition, 2009.
- [14] M. Bolzonella, J.-M. Miralles, and R. Pelló. Photometric redshifts based on standard SED fitting procedures. *A&A*, 363:476–492, 2000.

- [15] H. Bondi. Spherically symmetrical models in general relativity. *Mon. Not. Roy. Astr. Soc.*, 107:410–+, 1947.
- [16] H. Bondi. Gravitational waves in general relativity. *Nature*, 186:535–535, 1960.
- [17] H. Bondi. *Cosmology*. Cambridge University Press, second edition, 1961.
- [18] H. Bondi, M. G. J. van der Burg, and A. W. K. Metzner. Gravitational Waves in General Relativity. VII. Waves from Axi-Symmetric Isolated Systems. *Proc. Roy. Soc. London A*, 269:21–52, 1962.
- [19] R. L. Burden and J.D. Faires. *Numerical Analysis*. PWS Publishing Company Boston, fifth edition, 1993.
- [20] K. Nakao C-M. Yoo, T. Kai. Solving the Inverse Problem with Inhomogeneous Universes. *Prog. Theor. Phys.*, 120:937–960, 2008.
- [21] M.-N. Célérier. Do we really see a cosmological constant in the supernovae data? *A & A*, 353:63–71, 2000.
- [22] M.-N. Célérier. Models of universe with a delayed big-bang singularity. III. Solving the horizon problem for an off-center observer. *A & A*, 362:840–844, 2000.
- [23] M.-N. Célérier. The Accelerated Expansion of the Universe Challenged by an Effect of the Inhomogeneities. A Review. <http://arxiv.org/abs/astro-ph/0702416>, 2007.
- [24] M.-N. Célérier. Some clarifications about Lemaître-Tolman models of the Universe used to deal with the dark energy problem. *A&A*, 543:A71–+, 2012.
- [25] M. N. Célérier and J. Schneider. A solution to the horizon problem: A delayed big bang singularity. *Phys. Lett. A*, 249:37–45, 1998.
- [26] D. S. Chellone. A cosmological characteristic initial value problem. *Journal of Physics A Mathematical General*, 9:337–342, 1976.
- [27] D. S. Chellone. A characteristic initial-value problem approach to the formation of inhomogeneities in the early universe. *Journal of Physics A Mathematical General*, 14:2339–2343, 1981.
- [28] C. A. Clarkson. On the Observational Characteristics of Inhomogeneous Cosmologies: Undermining the Cosmological Principle. <http://arxiv.org/abs/astro-ph/0008089>, 2000.
- [29] M. P. Dabrowski and M. A. Hendry. The Hubble Diagram of Type IA Supernovae in Non-Uniform Pressure Universes. *Astrophys. J.*, 498:67–+, 1998.
- [30] G. Dautcourt. The cosmological problem as initial value problem on the observer’s past light cone - Geometry. *Journal of Physics A Mathematical General*, 16:3507–3528, 1983.
- [31] G. Dautcourt. The cosmological problem as initial value problem on the observer’s past light cone - Observations. *Astronomische Nachrichten*, 304:153–161, 1983.
- [32] G. Ellis. Editorial note to: Jerome Kristian and Rainer K. Sachs, Observations in cosmology. *Gen. Rel. Grav.*, 43:331–336, 2011.
- [33] G. F. R. Ellis. Cosmology and verifiability. *Q. J. Roy. Astr. Soc.*, 16:245–264, 1975.
- [34] G. F. R. Ellis and T. Buchert. The universe seen at different scales [rapid communication]. *Physics Letters A*, 347:38–46, 2005.

- [35] G. F. R. Ellis, R. Maartens, and M. A. H. MacCallum. *Relativistic Cosmology*. Cambridge University Press, first edition, 2012.
- [36] G. F. R. Ellis, S. D. Nel, R. Maartens, W. R. Stoeger, and A. P. Whitman. Ideal observational cosmology. *Phys. Reports*, 124:315–417, 1985.
- [37] G. F. R. Ellis and T. Rothman. Lost horizons. *American Journal of Physics*, 61:883–893, 1993.
- [38] G. F. R. Ellis and H. van Elst. Cosmological Models (Cargèse lectures 1998). In *NATO ASIC Proc. 541: Theoretical and Observational Cosmology*, pages 1–116. Kluwer, Dordrecht, The Netherlands, 1999.
- [39] G.F.R Ellis. Relativistic Cosmology. In *General Relativity and Cosmology, Proc. Int. School of Physics ‘Enrico Fermi’ (Varennna), Course XLVII, Ed. R.K. Sachs*, pages 104–179. Academic Press, 1971. Reprinted in *Gen. Rel. Grav.* 41, 581 (2009).
- [40] K. Enqvist. Lemaitre Tolman Bondi model and accelerating expansion. *Gen. Rel. Grav.*, 40:451–466, 2008.
- [41] I. M. H. Etherington. On the Definition of Distance in General Relativity. *Philosophical Magazine*, 15:761, 1933.
- [42] W. Fischler, S. Paban, M. Žanić, and C. Krishnan. Vacuum bubble in an inhomogeneous cosmology. *Journal of High Energy Physics*, 5:41–+, 2008.
- [43] P. S. Florides and W. H. McCrea. Observable relations in relativistic cosmology III. With 3 figures in the text. *Zs. f. Astrophys.*, 48:52–+, 1959.
- [44] J. Foster and J. D. Nightingale. *A Short Course in General Relativity*. Springer, second edition, 1995.
- [45] W. L. Freedman, B. F. Madore, B. K. Gibson, L. Ferrarese, D. D. Kelson, S. Sakai, J. R. Mould, R. C. Kennicutt, Jr., H. C. Ford, J. A. Graham, J. P. Huchra, S. M. G. Hughes, G. D. Illingworth, L. M. Macri, and P. B. Stetson. Final Results from the Hubble Space Telescope Key Project to Measure the Hubble Constant. *Astrophys. J.*, 553:47–72, 2001.
- [46] H. Friedrich and J.M. Stewart. Characteristic Initial Data and Wavefront Singularities in General Relativity. *Proc. R. Soc. London, Ser A*, 385:345–371, 1983.
- [47] J. Garcia-Bellido and T. Haugbølle. Confronting Lemaitre Tolman Bondi models with observational cosmology. *JCAP*, 4:3, 2008.
- [48] S. W. Hawking and G. F. R. Ellis. *The large-scale structure of space-time*. Cambridge University Press, first edition, 1973.
- [49] C. Hellaby. The mass of the cosmos. *Mon. Not. R. Astron. Soc.*, 370:239–244, 2006.
- [50] C. Hellaby and A. H. A. Alfedeel. Solving the observer metric. *Phys. Rev. D*, 79(4):043501–+, 2009.
- [51] T. Hui-Ching Lu and C. Hellaby. Obtaining the spacetime metric from cosmological observations. *Class. Quantum Grav.*, 24:4107–4131, 2007.
- [52] A. S. Iribarrem, A. R. Lopes, M. B. Ribeiro, and W. R. Stoeger. Relativistic cosmology number densities and the luminosity function. *A & A*, 539:A112–+, 2012.
- [53] M. Ishak. Perfect fluid models in noncomoving observational spherical coordinates. *Phys. Rev. D*, 69(12):124027, 2004.

- [54] R. Kantowski. Inhomogeneities and the Intergalactic Distance-Redshift Relation. <http://arxiv.org/abs/astro-ph/9804249>, 1998.
- [55] S. Khosravi, E. Kourkchi, R. Mansouri, and Y. Akrami. An inhomogeneous model universe behaving homogeneously. *Gen. Rel. Grav.*, 40:1047–1069, 2008.
- [56] J. Kristian and R. K. Sachs. Observations in Cosmology. *Astrophys. J.*, 143:379, 1966.
- [57] P. D. Lax and R. D. Richtmyer. Survey of the stability of linear finite difference equations. *Communications on Pure and Applied Mathematics*, 9(2):267–293, 1956.
- [58] M. S. Longair. *The cosmic century : a history of astrophysics and cosmology*. Cambridge University Press, 2006.
- [59] R. Maartens. *Idealised observations in relativistic cosmology*. University of Cape Town PhD thesis, 1980.
- [60] R. Maartens, N. P. Humphreys, D. R. Matravers, and W. R. Stoeger. Inhomogeneous universes in observational coordinates. *Class. Quantum Grav.*, 13:253–264, 1996.
- [61] R. Maartens and D. R. Matravers. Isotropic and semi-isotropic observations in cosmology. *Class. Quantum Grav.*, 11:2693–2704, 1994.
- [62] T. Mattsson. Dark energy as a mirage. *Gen. Rel. Grav.*, 42:567–599, 2010.
- [63] M. L. McClure and C. Hellaby. Determining the metric of the Cosmos: Stability, accuracy, and consistency. *Phys. Rev. D*, 78(4):044005–+, 2008.
- [64] W. H. McCrea. Observable relations in relativistic cosmology. Mit 1 Abbildung. *Zs. f. Astrophys.*, 9:290–+, 1935.
- [65] W. H. McCrea. Observable Relations in Relativistic Cosmology. II. *Zs. f. Astrophys.*, 18:98–+, 1939.
- [66] G. C. McVittie. Appendix to The Change of Redshift and Apparent Luminosity of Galaxies due to the Deceleration of Selected Expanding Universes. *Astrophys. J.*, 136:334–+, 1962.
- [67] P. Mishra, M.-N. C el erier, and T. P. Singh. Redshift-drift as a test for discriminating between decelerating inhomogeneous and accelerating universe models. <http://arxiv.org/abs/1301.4358>, 2013.
- [68] C. W. Misner, K. S. Thorne, and J. A. Wheeler. *Gravitation*, pages 715–717. 1973.
- [69] J. W. Moffat. Late-time inhomogeneity and acceleration without dark energy. *JCAP*, 5:1–+, 2006.
- [70] M. Moresco *et al.* Improved constraints on the expansion rate of the Universe up to  $z \sim 1.1$  from the spectroscopic evolution of cosmic chronometers. *JCAP*, 8:6–+, 2012.
- [71] N. Mustapha, C. Hellaby, and G. F. R. Ellis. Large-scale inhomogeneity versus source evolution - Can we distinguish them observationally? *Mon. Not. R. Astron. Soc.*, 292:817–+, 1997.
- [72] J. V. Narlikar. *An Introduction to Cosmology*. Cambridge University Press, third edition, 2002.
- [73] J. Oprea. *Differential Geometry and its Applications*. The Mathematical Association of America, second edition, 2007.

- [74] J.-F. Pascual-Sánchez. Cosmic Acceleration: Inhomogeneity Versus Vacuum Energy. *Modern Physics Letters A*, 14:1539–1544, 1999.
- [75] L. Pasquini, S. Cristiani, R. Garcia-Lopez, M. Haehnelt, and M. Mayor. CODEX: An Ultra-stable High Resolution Spectrograph for the E-ELT. *The Messenger*, 140:20–21, 2010.
- [76] R. Penrose. Asymptotic properties of fields and space-times. *Phys. Rev. Lett.*, 10:66–68, 1963.
- [77] S. Perlmutter *et al.* Measurements of  $\omega$  and  $\lambda$  from 42 high-redshift supernovae. *Astrophys. J.*, 517(2):565–586, 1999.
- [78] J. Plebański and A. Krasinski. *An Introduction to General Relativity and Cosmology*. Cambridge University Press, first edition, 2006.
- [79] M. Quartin and L. Amendola. Distinguishing between void models and dark energy with cosmic parallax and redshift drift. *Phys. Rev. D*, 81(4):043522–+, 2010.
- [80] C. Reisswig, N. T. Bishop, and D. Pollney. General relativistic null-cone evolutions with a high-order scheme. <http://arxiv.org/abs/1208.3891>, 2012.
- [81] M. B. Ribeiro. Observations in the Einstein-De Sitter cosmology: Dust statistics and limits of apparent homogeneity. *Astrophys. J.*, 441:477–487, 1995.
- [82] M. B. Ribeiro and W. R. Stoeger. Relativistic Cosmology Number Counts and the Luminosity Function. *Astrophys. J.*, 592:1–16, 2003.
- [83] A. G. Riess *et al.* Observational evidence from supernovae for an accelerating universe and a cosmological constant. *Astronomical Journal*, 116:1009, 1998.
- [84] W. Rudin. *Principle of Mathematical Analysis*. McGraw-Hill Book Company, third edition, 1976.
- [85] R. K. Sachs. Gravitational Waves in General Relativity. VIII. Waves in Asymptotically Flat Space-Time. *Proc. Roy. Soc. London A*, 270:103–126, 1962.
- [86] A. Sandage. The Change of Redshift and Apparent Luminosity of Galaxies due to the Deceleration of Selected Expanding Universes. *Astrophys. J.*, 136:319–+, 1962.
- [87] J. Schneider and M.-N. Célérier. Models of Universe with an inhomogeneous Big Bang singularity. II. CMBR dipole anisotropy as a byproduct of a conic Big-Bang singularity. *A & A*, 348:25–30, 1999.
- [88] W. R. Stoeger, M. E. Araujo, and T. Gebbie. The Limits on Cosmological Anisotropies and Inhomogeneities from COBE Data. *Astrophys. J.*, 476:435–+, 1997.
- [89] W. R. Stoeger, G. F. R. Ellis, and S. D. Nel. Observational cosmology. III. Exact spherically symmetric dust solutions. *Class. Quantum Grav.*, 9:509–525, 1992.
- [90] W. R. Stoeger, G. F. R. Ellis, and C. Xu. Observational cosmology. VI. The microwave background and the Sachs-Wolfe effect. *Phys. Rev. D*, 49:1845–1853, 1994.
- [91] W. R. Stoeger, S. D. Nel, R. Maartens, and G. F. R. Ellis. The fluid-ray tetrad formulation of Einstein’s field equations. *Class. Quantum Grav.*, 9:493–507, 1992.
- [92] W. R. Stoeger, S. J. Stanley, D. Nel, and G. F. R. Ellis. Observational cosmology. IV. Perturbed spherically symmetric dust solutions. *Class. Quantum Grav.*, 9:1711–1723, 1992.

- [93] W. R. Stoeger, S. J. Stanley, D. Nel, and G. F. R. Ellis. Observational cosmology. V. Solution of the first-order general perturbation equations. *Class. Quantum Grav.*, 9:1725–1751, 1992.
- [94] G. Temple. New Systems of Normal Co-ordinates for Relativistic Optics. *Proc. Roy. Soc. London A*, 168:122–148, 1938.
- [95] K. Tomita. Distances and Lensing in Cosmological Void Models. *Astrophys. J.*, 529:38–46, 2000.
- [96] J.-P. Uzan, C. Clarkson, and G. F. R. Ellis. Time Drift of Cosmological Redshifts as a Test of the Copernican Principle. *Physical Review Letters*, 100(19):191303–+, 2008.
- [97] P. J. van der Walt and N. T. Bishop. Observational cosmology using characteristic numerical relativity. *Phys. Rev. D*, 82(8):084001–+, 2010.
- [98] P. J. van der Walt and N. T. Bishop. Observational cosmology using characteristic numerical relativity: Characteristic formalism on null geodesics. *Phys. Rev. D*, 85(4):044016–+, 2012.
- [99] M. Visser. Cosmography: Cosmology without the Einstein equations. *Gen. Rel. Grav.*, 37:1541–1548, 2005.
- [100] R. M. Wald. *General relativity*. The University of Chicago Press, first edition, 1984.
- [101] J. Winicour. Characteristic Evolution and Matching. *Living Reviews in Relativity*, 15:2, 2012.
- [102] Chul-Moon Yoo, Tomohiro Kai, and Ken-ichi Nakao. Redshift drift in Lemaitre-Tolman-Bondi void universes. *Phys. Rev. D*, 83:043527–+, 2011.